2012

Enhanced performance of organic light-emitting diodes (OLEDs) and OLED-based photoluminescent sensing platforms by novel microstructures and device architectures

Rui Liu
Iowa State University

Enhanced performance of organic light-emitting diodes (OLEDs) and OLED-based photoluminescent sensing platforms by novel microstructures and device architectures

by

Rui Liu

A dissertation submitted to the graduate faculty

in partial fulfillment of the requirements for the degree of

DOCTOR OF PHILOSOPHY

Major: Condensed Matter Physics

Program of Study Committee:

Joseph Shinar, Major Professor

Ruth Shinar

Rana Biswas

Adam Kaminski

James Vary

Iowa State University

Ames, Iowa

2102

Table of Contents

Chapter 1. Introduction to OLEDs and OLED-Based Photoluminescent (PL) Sensors

1.1 History of OLED Development

Electroluminescence (EL) from organic devices operated in an ac mode was first reported in 1953 [1]. This report was followed by a 1963 work by Pope and coworkers on single crystal anthracene OLEDs [2]. However, only in 1987, when Tang and Van Slyke established the bilayer heterojunction small molecular organic light emitting diodes (SMOLEDs) [3], the advantages and promising applications of thin film-based OLEDs were realized. The reported device included a ~100 nm bilayer structure of N,N'-diphenyl-N,N-bis(3-methyl-phenyl)-1,1-biphenyl-4,4-diamine (TPD) and tris(8-hydroxyquinoline) Al (Alq_3) achieving an external quantum efficiency (EQE) ~ 1% and maximum brightness > 1000 Cd/m^2. This work together with the first polymer LEDs (PLEDs), demonstrated in 1990 [4] using spin-coated poly (para-phenylene vinylene) (PPV), have stimulated massive research and industrial interest in both vacuum-deposited and solution-processed OLEDs.

In 1992, Gustafsson *et al.* demonstrated the first flexible OLED on a polyethylene terephthalate (PET) substrate. Polyaniline (PANI) was utilized as the transparent "hole-injection contact" yielding comparable efficiency to inflexible ITO-based devices [5]. In 1994, Kido *et al.* reported the first white OLEDs using a double emitting layer structure with mixed blue and orange emission in the same device [6]. The device exhibited white emission covering a wide range of the visible region with a maximum luminance of 3400 Cd/m^2. Abundant research and development studies

have contributed to the development of innovative device structures and architectures, which paved the way to many potential applications, such as flat-panel displays, solid-state lighting, and OLED-based (bio)chemical sensing platforms [7-11].

Another milestone in OLED history was set by introducing phosphorescent materials into the device structure. In 1998 Baldo *et al.* applied the phosphorescent dopant platinum octaethylporphine (PtOEP) in the OLED to harvest triplet excitons [12]. This method enables one to break the 25% theoretical internal efficiency limit which was statistically predicted in fluorescent devices based on singlet exciton emission. Indeed, as shown in Adachi's following work, the second generation iridium-based phosphorescent dye was doped into a wide energy gap host material to achieve almost ~ 100% internal quantum efficiency [13].

Despite the fact that almost all the excitons can be utilized to emit light by optimizing the materials and carrier balance in the device, waveguiding within the ITO/organic layers and the substrate still prevent a large fraction of the generated light from being extracted. Starting from Sun's work on a low index grid for electroluminescent (EL) outcoupling enhancement [14], numerous studies have introduced various methods and solutions to improve the devices, partially alleviating this issue. Currently, white OLEDs with efficiency comparable to those of fluorescent tubes can be achieved [15]. The most efficient OLED has reached a ~ 63% EQE and ~ 290 lm/W power efficiency [16]. With improved device lifetime and efficacy, OLEDs have reached the last step toward mass production.

1.2 OLED Applications

A question that many may ask is why so much effort is spent on the development of OLEDs. The short answer is that OLEDs provide a wide variety of possibilities for making them superior to liquid crystal displays (LCDs), inorganic LEDs and fluorescent tubes. OLEDs are extremely thin (< 400 nm) and compatible with simple substrates and microfluidic structures. Their solution processability makes them easy to fabricate and hence, potentially low cost. Devices with selective colors and functionality can be made as one can easily tune the properties of the organic materials by changing the functional groups or ligands. Unlike LCDs, the displays made from OLEDs are self-luminous with no need for backlighting or polarizers, which provides a much wider viewing angle (> 160^{o}), higher contrast ratio and lower power consumption. These advantages enable one to fabricate better performing and cost-effective display products with OLEDs. With respect to lighting application, OLEDs are unique as they are diffuse (large area) and dimmable light sources. These two characteristics cannot be achieved simultaneously by neither LEDs nor fluorescent tubes.

More importantly, OLEDs can be made flexible and transparent. This creates many possibilities for innovative and distinct applications such as e-papers, smart bandages [17], and interactive displays that used to be feasible only in a Star Wars movie [18].

In spite of all the above-mentioned merits, there are still a few hurdles limiting OLED mass production. The disadvantages of OLEDs are mainly related to their

stability. The presence of UV light, oxygen and humidity can cause organic materials degradation and delamination between the metal electrodes and the active layers. As high band gap materials usually degrade faster, the blue OLED pixels possess a very different life span from the green and red pixels, which makes it difficult to fabricate OLED displays with a stable color balance. Extensive efforts have been made in encapsulation techniques, device structures and material synthesis to extend the lifetime of the devices [19-22]. Currently, accelerated measurements predict a record pixel lifetime of one million hours for green emitting OLEDs [23]. However, studies on enhancing lifetimes of panels, with comparable performance of pixels with different colors, are still needed.

If the process of commercialization of OLEDs in large-area flat-panel displays and solid-state lighting is a marathon, we are now probably at the last 100 yards to the finish line. There are already many existing products in cell phone screens and camera displays like Nokia 6215i, Samsung Galaxy and Nikon Coolpix, as well as in TV displays. In early 2007, Sony announced the first OLED TV – 11 inch XEL-1 with 45 Watt power consumption and 1,000,000:1 contrast ratio. LG and Samsung both will start to sell their 55 inch OLED TV in the middle of 2012. LG's product weighs only 7.5 kg and is 4 mm thick utilizing white OLED subpixels with color filters for reduced fabrication cost, while Samsung's product is based on true red-green-blue (RGB) pixels for more efficient emission. Additionally, many companies such as LG Chem, OSRAM, Philips, GE, Konica Minolta, Lumiotec, and Novaled have started to produce and sell OLED lighting products. These products are usually extremely light

and thin with a power efficiency of ~ 40-60 lm/W. Some of the products were as low as $100 per panel and aiming for massive reduction of price as production increases [24]. As more applications emerge, R&D on OLEDs continues to be important and necessary for better understanding of the operating mechanisms and further improving the device performance.

1.3 OLED Structures

The state-of- the art OLEDs are usually fabricated on glass or plastic substrates with multilayer thin film structures. The device generally includes ~ 100 nm thick organic layers that are sandwiched between two electrodes.

In order to couple the light out, one of the electrodes has to be largely transparent. For most of the devices, indium tin oxide (ITO) and poly (3,4-ethylenedioxy-thiophene):poly (styrenesulfonate) (PEDOT: PSS) are applied as the anode due to their high work function (W_F). The W_F of ITO ranges from 4.1 to 4.7 eV due to different oxygen vacancy levels and surface treatments [25,26]. Helander *et al.* recently found that a W_F greater than 6.1 eV can be achieved in the case of chlorinated ITO without altering the surface roughness, transparency and conductivity [27]. PEDOT:PSS was also well established as a polymer anode with a W_F of 4.7- 5.4 eV[28-31] in spite of its low conductivity (< 10 S/cm) [32]. Treatments with high boiling point solvents and multilayer deposition could largely improve its conductivity and make it promising for solution-processed OLEDs [33,34].

For the cathode, low W_F metals such as Ba (W_F ~ 2.7 eV), Ca (W_F ~ 2.87 eV), Mg (W_F ~ 3.66 eV) and Al (W_F ~ 4.26 eV) [35] are usually utilized to minimize the

energy barrier for electron injection. As many low W_F metals are reactive in ambient conditions, electron injection layers (EIL) such as LiF [36], CsF [37], lithium quinolate (Liq) [38] and Cs_2CO_3 [39] are applied at the organic/cathode interface.

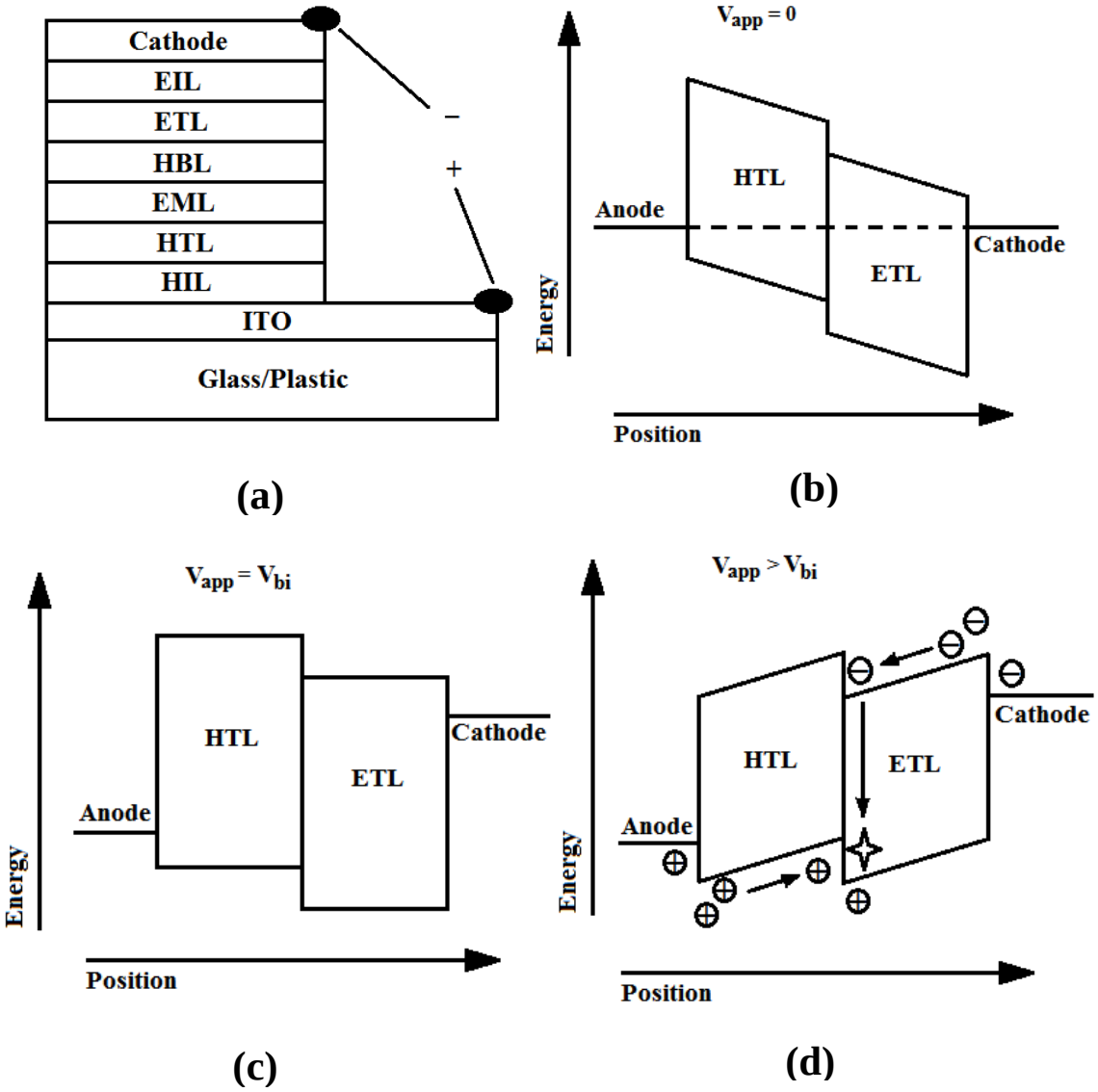

Fig. 1-1 (a) General structure of a SMOLED (not to scale); energy levels of a two-layer OLED under (b) short circuit, (c) turn-on threshold and (d) operation with continued forward bias.

As one of the merits of SMOLEDs, shown in Fig. 1(a), the organic part is usually comprised of multiple layers, each with its own functionality. The common layers are hole injection layer (HIL), hole transport layer (HTL), emission layer (EML), hole

blocking layer (HBL), electron transport layer (ETL) and EIL. PLEDs generally consist of a simpler structure, with the number of layers limited by solution orthogonality. Hence, PLEDs are often less efficient. A third class of OLEDs is based on dendrimers [40]. A typical dendrimer includes a core, dendrons, and surface groups. Processing, luminescent and electronic properties of surface groups and cores can be optimized independently. The number of dendrons provides molecular control over the intermolecular interactions that are crucial for device performance. Devices with such materials can achieve efficiencies comparable to SMOLEDs while maintaining solution processability.

Other than the conventional bottom-emitting architectures, OLEDs can also be configured with top-emitting structures giving off light through a transparent top electrode. Such structures are especially suitable with active matrix OLED (AMOLED) designs and opaque substrates, increasing the effective area and hence the resolution of the OLED displays [41].

Novel tandem OLEDs were also introduced recently. These devices have multiple emitting units stacked vertically in series providing higher brightness and current efficiency [42,43], which is attractive in solid-state lighting. One of the most important components of tandem OLEDs is the charge generation layer (CGL) that connects the different units. A double-layer junction with electric doping or large energy level contrast, favorable for electron-hole separation, is usually selected as efficient CGL for tandem OLEDs [42-45].

Figs. 1(b)-(d) show the energy level alignment under different operation

conditions of a typical double layer OLED. When there is no applied bias (V_{app}), the Fermi energies of the anode and cathode are shifted to align with each other. As shown in Fig. 1(b), the tilted bands of the HTL and ETL are unfavorable for carrier injection. Only when the applied forward bias reaches the built-in potential V_{bi}, the flat-band state can be reached as indicated in Fig. 1(c). Typical values of V_{bi} are ~1.5 – 3 V, related to the energy gap of the organic materials. This represents the threshold state of the OLED. As seen in Fig 1(d), increased forward bias would initiate carrier injection into the device. Holes and electrons drift under the influence of the external field. When oppositely charged carriers are injected and transported into organic layers, they recombine to form excitons. Radiative relaxation of the excitons generates photons, part of which is coupled out of the devices.

1.4 Operating Mechanisms of OLEDs

π-conjugated organic materials

Organic semiconductors are based on π-conjugated materials, i.e. materials with alternating single and double bonds through the molecule or polymer backbone. In such materials, sp^2 hybridization in C atoms is formed with three sp^2 orbitals (derived from *s*, p_x, and p_y orbitals and forming σ bonds with adjacent atoms) and one p_z orbital (forming a π bond with an adjacent p_z orbital). The σ bonds are coplanar with an angle of 120° and strongly localized. The p_z orbitals are perpendicular to the σ bond plane. Two p_z orbitals of adjacent carbon atoms form the relatively weak π bond, where the electrons are delocalized and move relatively freely in the molecule contributing to the semiconducting properties.

The band structures in π-conjugated materials are formed from discrete energy levels. As shown in Fig. 1-2, two p_z orbitals result in splitting into two energy levels (molecular orbitals). According to the Pauli exclusion principle, every energy state can be occupied by two electrons. Thus, in the ground state only the π orbital will be occupied by the electrons. In a molecular system with more carbon atoms, the two energy levels broaden into quasi-continuous energy bands. The highest occupied molecular orbital (HOMO) and lowest unoccupied molecular orbital (LUMO) are formed, in analogy to the top of the valence and the bottom of the conduction band.

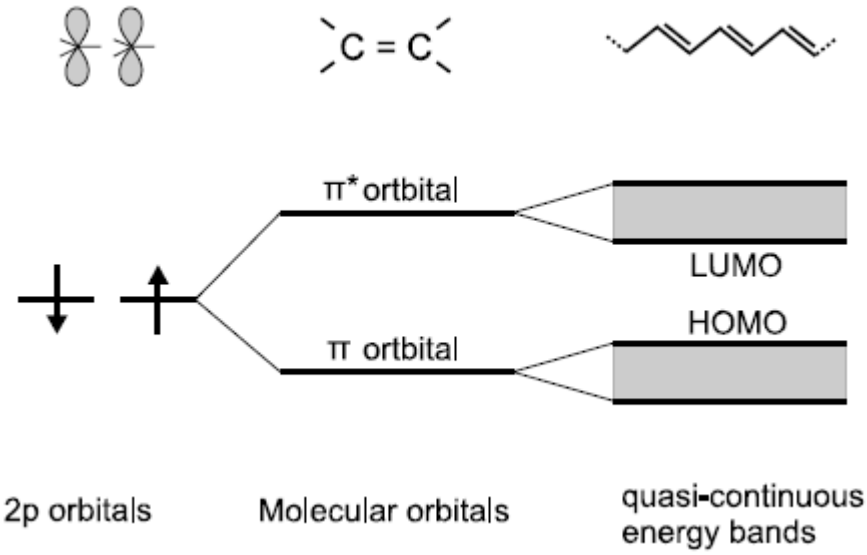

Fig. 1-2 Schematic representation of the molecular orbital splitting and quasi-continuous bands of occupied and unoccupied states in π-conjugated materials [46].

Carrier Injection

In general, carrier injection into organic materials has been described using thermionic emission, Fowler–Nordheim (FN) tunneling, and modifications of the above models. If we take electron injection as an example, when the contact between the cathode and the ETL is established, some electrons are injected into the trap states

of the organic materials. This results in an “image” potential due to the Coulomb attraction between these electrons and the holes which are left behind in the metal. When a forward electric field is applied, the effective potential barrier experienced by an electron is:

$$\phi_{\mathrm{B}}(x) = \phi_{\mathrm{m}} - qEx - q^2/16\pi\epsilon x \qquad (1.1)$$

where x is the distance between the electrons and the organic/cathode interface, E is the electric field and ϕ_{m} is the work function of the cathode.

The second and third terms of Eq. (1.1) come from the effect of the applied bias and the image charges, respectively. As demonstrated in Fig. 1-3, both the applied electric field and the image charge potential reduce the energy barrier at the interface and render it favorable for electron injection.

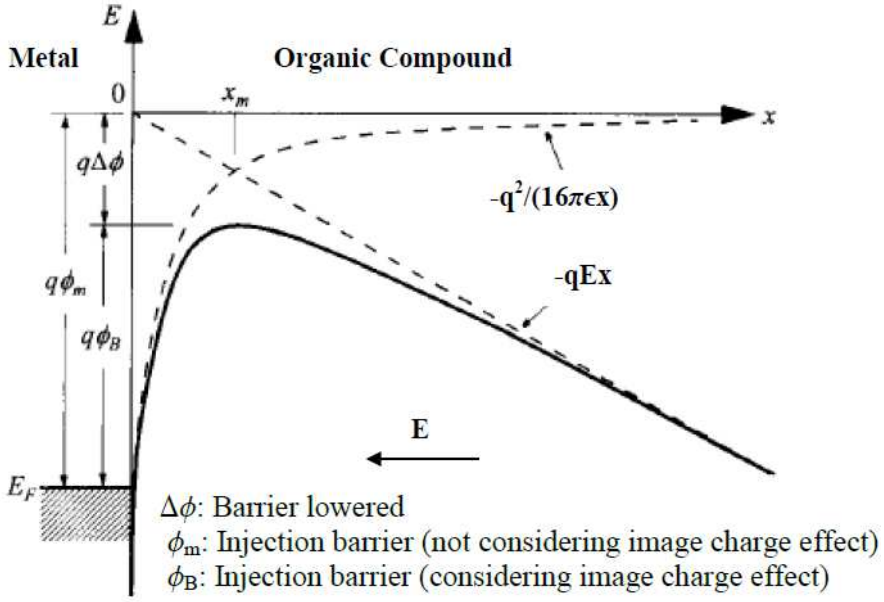

Fig. 1-3 Energy barrier lowering by the image charge at the organic/metal interface [47].

If we assume that an electron from the metal can be injected once it acquires sufficient thermal energy to surpass the maximum potential barrier shown in Fig. 1-3,

the thermionic injection current can be written as [47]

$$J_{th} = A^{*}T^{2}e^{-q\phi_{B}/kT} \quad (1.2)$$

with the Richardson constant A^{*} given by

$$A^{*} = 4\pi q m^{*} k^{2}/h^{3} \quad (1.3)$$

where m^{*} is the carrier effective mass and k is the Boltzmann constant.

If one substitutes Eq. (1.1) into Eq. (1.2),

$$J_{th} \propto e^{qV/kT} \quad (1.4)$$

It is worth to note that Eq. (1.2) represents the maximum current that can flow across the interface when no scattering occurs. However, when both the mobility of the ejected carrier and the applied field are low, the carriers can backflow into the electrode.

At low temperatures and high electric fields, field-assisted tunneling can be important. The FN tunneling model describes the tunneling of electrons from the metal through a triangular barrier, which can be made thin by applying higher fields. Such an injection current can be written as [47,48]

$$J_{FN} = \frac{q^{3}}{4h\phi} E^{2} e^{-\frac{8\pi\sqrt{2m^{*}}\phi^{3/2}}{3qhE}} \quad (1.5)$$

where ϕ is the metal/organic potential barrier.

This equation can be further simplified as

$$J_{FN} \propto V^{2} e^{-\frac{b}{V}} \quad (1.6)$$

In 1991, Braun and Heeger reported such a FN tunneling-based conduction in a poly[[[(2-ethylhexyl)oxy]methoxy-1,4-phenylene]-1,2-ethenediyl] (MEH-PPV) OLED [49]. They compared the fit of the *I-V* characteristic with models based on

thermionic emission and FN tunneling, as shown in Fig.1-4. It clearly showed that the experiment was consistent with the tunneling model at a relatively high electric field ranging from 7×10^5 to 3×10^6 V/cm if a device thickness of ~100 nm is assumed. Nonetheless, many fundamental considerations such as backflow current, injection into polaron levels and direct chemical interactions between the metal and the organic molecules [50] defeat the oversimplified treatment of the current injection. As a result, no general treatment is expected, with each process to be analyzed independently.

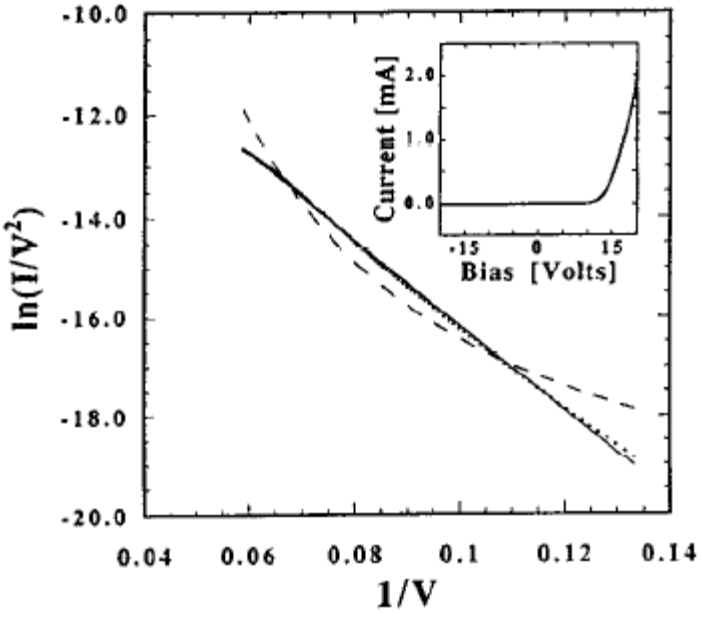

Fig. 1-4 ln(I/V^2) vs. 1/V for ITO/MEH-PPV diode: the dashed line is the best fit to Eq. (1.4) and the solid line is the best fit to Eq. (1.6). The inset shows the current and voltage characteristic [49].

Carrier Transport

Organic semiconductor layers are usually amorphous. The molecules interact with each other through Van der Waals forces, which are much weaker than covalent bonding. Consequently, the carriers are transported by site-to-site hopping through the molecular segments instead of band-like transport. As a result, the mobility is several

orders of magnitude lower than that of the inorganic counterparts. The typical mobility is ~10^{-6}-10^{-3} $cm^2/(V\cdot s)$ [11,50], where it is usually more than 10^2 $cm^2/(V\cdot s)$ for inorganic semiconductors.

The field-dependence of the carrier mobilities in OLEDs is given by [51]:

$$\mu = \mu_0 e^{-\Delta/kT} e^{\beta\sqrt{E}} \qquad (1.7)$$

Where μ_0 is the zero-field prefactor, Δ is the activation energy, E is the electric field and β is a field dependence coefficient.

As shown in Fig. 1-5, this dependence relies on a picture in which the carriers are generally trapped in localized states and hop between different potential wells with phonon-assisted and field-assisted energy. With thermal energy from lattice distortion they escape the localized states and transport through the LUMO and may be trapped again in another site. With the applied electric field, the potential level changes with the field asymmetrically, thus lowering the barrier for the carriers to escape.

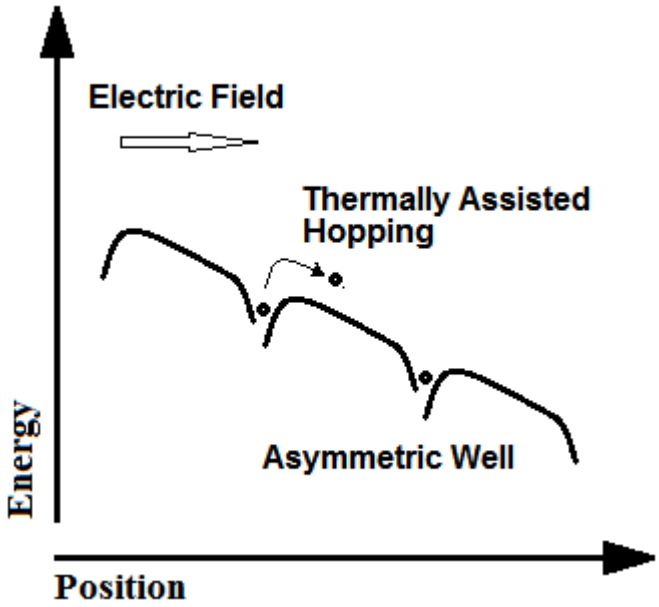

Fig. 1-5 Schematics of phonon-assisted and field-assisted carrier hopping in OLEDs.

As mentioned, the carrier mobility of organic semiconductors is several orders of magnitude lower than their inorganic counterparts. When bias is applied to the OLED, strong current injection into low-mobility materials inevitably leads to charge accumulation in the bulk of the organic layers. This charge build-up partially screens the applied electric field resulting in its redistribution. Hence, the *J-V* characteristic of a diode exhibits ohmic and injection-limited behavior in the low voltage range and space-charge limited current (SCLC) relations in higher voltage range due to the excessive injected carriers. Considering discrete traps that are present in the layers, the modified SCLC relation was written as

$$J_{SCLC} = 9\epsilon\epsilon_0(\Theta\mu)V^2/8d^3 \qquad (1.8)$$

where μ is the mobility, ε is the dielectric constant, V is the applied voltage, d is the thickness of the film, and Θ is the ratio of the free and trapped charge concentration [53,54].

However, the local increase in the quasi-Fermi level due to strong injection may lead to charge immobilization in the deep states of the disorder-induced distribution of the HOMO and LUMO levels [50]. The study on Alq_3-based and other OLEDs by Burrows *et al.* in 1996 has clearly shown that the *J-V* characteristic can be summarized as [55]

$$J \propto V^{m+1} \qquad (1.9)$$

where m is a factor dependent on trap density and distribution.

In the low voltage range, the *J-V* behavior obeys SCLC ($J \sim V^2/d^3$) for the thinnest film and Ohmic relation ($J \sim V/d$) for thicker films. While in high voltage range, the

J-V shows trap-charge-limited (TCL) behavior as *m* varies from 6 to 8 depending on different device structures and materials. Such a method was utilized in various electrically active organic films explaining the DC *J-V* curves in the most common types of OLEDs.

Recombination

Another distinct property of organic semiconductors compared to inorganic ones is the dielectric constant ε. The lower ε of the organic semiconductors (ε~3–5), compared to that of the inorganic semiconductors (ε > 10) causes different levels of dielectric screening. Therefore Frenkel excitons usually exist in OLEDs with a typical binding energy 0.3~1eV and a binding radius of ~ 1 nm, while the excitons in the inorganic LEDs are mostly Mott-Wannier excitons with binding energy ~ 10 meV and a binding radius ~ 10 nm [52].

The Coulombic attraction between electron and hole pairs needs to surpass the thermal energy for them to be bonded and form excitons through a random walk process. The Onsager radius

$$r_c = e^2/4\pi\epsilon\epsilon_0 kT \qquad (1.10)$$

is therefore the maximum separation for electron-hole capture. It is typically ~19 nm for organic materials in room temperature. At high injection levels strong carrier concentration gradients may build up at the interface, leading to increased local electric fields. These fields are formed close to the recombination zone leading to a dramatic decrease in emission efficiency through field-assisted exciton dissociation. This decreased efficiency at high injection levels is called “roll-off” and has been

observed in almost all multi-layer OLEDs [11,12]. Obviously, balancing carrier injection and transport may significantly improve the steady-state efficiency at high brightness levels.

Fluorescence vs. Phosphorescence

In the ground state of organic molecules, the HOMO level is filled by two electrons with opposite spins based on the Pauli exclusion principle. Electrons at the HOMO level are most likely to participate in electron transfer or optical transitions. The remaining electrons occupy tightly filled orbitals. Therefore the system can be described by a two electron configuration, which gives either total spin 0 or 1. According to degeneracy, S=0 is called singlet and S=1 triplet with spin wavefunctions as following:

$$\text{Singlet} \quad |0,0\rangle = \frac{1}{\sqrt{2}}[\uparrow\downarrow - \downarrow\uparrow] \tag{1.11}$$

$$\text{Triplet} \begin{cases} |1,0\rangle = \frac{1}{\sqrt{2}}[\uparrow\downarrow + \downarrow\uparrow] \\ |1,1\rangle = \uparrow\uparrow \\ |1,-1\rangle = \downarrow\downarrow \end{cases} \tag{1.12}$$

In the Langevin model, the electron and hole capture cross section is believed to be spin-independent. Statistically in an electrically driven OLED, 25% of the excitons will be singlets and the rest will be triplets based on Eqs. (1.11) & (1.12) and this limits the maximum internal quantum efficiency (IQE) of a fluorescent OLED. However, there are suggestions that in polymers, the cross section for singlet excitons (SEs) formation is higher than for triplet excitons (TEs) [56,57].

IQE that exceeds 25% has also been observed in fluorescent SMOLEDs. In 1998, Kido *et al.* reported tris(4-methyl-8-quinolinolato)Al ($Almq_3$)-based devices with

EQE~7.1% [58]. This converts to an IQE that breaks the 25% fluorescent OLED limit. Such a phenomenon was also extensively studied afterwards in other systems and believed to be caused by triplet-triplet annihilation (TTA) into singlets [58,59].

$$T^* + T^* \rightarrow S^* + S \qquad (1.13)$$

i. e., a TE goes through annihilative reactions with another TE to form a SE and a singlet ground state. This process is facilitated when a large number of excited molecules are generated at high bias.

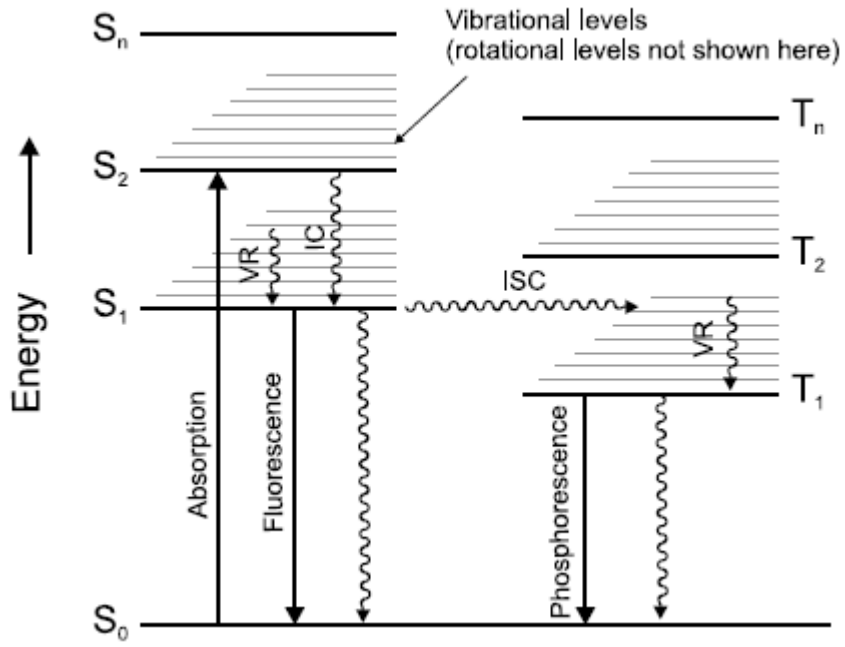

Fig. 1-6 Jablonski diagram illustrating the different energy levels of an organic molecule and indicating the possible transitions between them [46].

Fig. 1-6 demonstrates the possible transitions between different energy states in an OLED. In fluorescent systems, the radiative relaxation of the triplet is forbidden due to spin symmetry differences. However, it is necessary to note that singlets and triplets can be mixed by spin-orbit coupling. When heavy metal atoms are introduced into the organic molecules, the metal atom enhances the spin-orbit coupling and

reduces the phosphorescent lifetime significantly. This will result in a triplet state with additional singlet character and also enhances the probability of intersystem crossing (ISC) from the first SE state to the TE state as shown in Fig. 1-6. By utilizing both the SEs and TEs in phosphorescent systems, the theoretical limit of the IQE is 100% [13], as compared to the 25% limit in fluorescent OLEDs.

As mentioned earlier, the first phosphorescent OLED was reported in 1998 by Baldo *et al.* with PtOEP [12]. Adachi's following work with the second generation iridium-based phosphorescent dye achieved almost ~100% IQE [13]. Very recent studies show that by employing electron-donating and electron-accepting molecules that allow a very high reverse intersystem crossing (RISC) of 86.5% between non-radiative TE and radiative SE states, the TE can also be utilized for the emission of fluorescent OLEDs with increased IQE [60].

Energy Transfer vs. Charge Trapping

The organic materials possess a relatively low glass transition temperature (T_g). The crystallization of such compounds is one of the main degradation processes in OLEDs [11,50]. Doping of these compounds enhances stability by inhibiting the crystallization process and by localizing the excitation energy on the dopant or guest molecules. Furthermore, pristine fluorescent and phosphorescent organic molecules tend to aggregate. The intermolecular interactions cause either excitonic quenching through nonradiative decay or formation of excimers with emission at longer wavelength and lower efficiency [61]. Applying these materials as a dopant in guest-host systems prevents the aggregation and loss of efficiency.

In the guest-host system, an exciton can transfer its energy over to another molecule via radiative energy transfer, Förster Resonance Energy Transfer (FRET), or Dexter Energy Transfer (DET). In radiative energy transfer, the emission given off by the donor molecule is followed by the absorption of the photon by the acceptor molecule. Obviously, it can occur only if the emission spectrum of the donor overlaps the absorption spectrum of the acceptor.

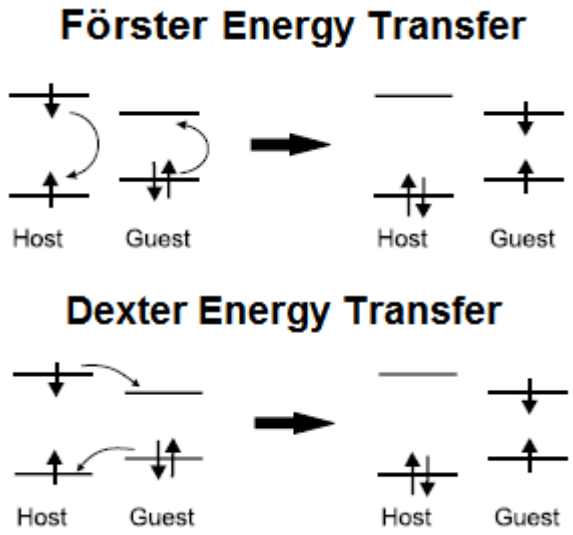

Fig. 1-7 Schematic description of Förster energy transfer and Dexter energy transfer.

Fig. 1-7 demonstrates the nonradiative FRET and DET processes. In the FRET process, an exciton on the host molecule induces a dipole in the guest molecule, and the inducing donor field can interact with the induced acceptor dipole. The FRET usually takes place within 10 nm at a time scale of nanoseconds. The rate of the energy transfer is proportional to $(1/R)^6$ [62]:

$$K_{FRET}(R) = \frac{1}{\tau_H}\left(\frac{R_0}{R}\right)^6 \qquad (1.14)$$

where R is the distance between the guest and host molecules, R_0 is the Förster Radius and τ_H is the average host exciton lifetime for recombination in the absence of energy

transfer.

Different from FRET, charge exchange is involved in DET, which occurs at a very short range (~1 nm). Consequently, as FRET requires $\Delta S = 0$ for both donor and acceptor, DET only requires the total spin conservation of the donor-acceptor system as a whole, thus triplet-triplet and triplet-singlet energy transfers are allowed. Electron exchange is a short range process, critically dependent on the distance *R*. The transfer rate is given by

$$K_{DET}(R) \propto \exp(-\frac{2R}{L}) \qquad (1.15)$$

where *L* is the sum of the van der Waals radii of the host and the guest molecules.

The optimized doping concentration of fluorescent guest-host systems is typically around 1% as higher doping leads to concentration quenching of the guest emission. However, phosphorescent OLEDs utilize the energy transfer with triplets. DET is mostly involved in the process, which requires a short interaction distance. This is the reason that phosphorescent guest-host systems use a doping ratio much higher than that of the fluorescent OLEDs, typically ~6-8% [11-13].

In the guest-host systems described above, either the HOMO or the LUMO level of the guest is usually inside the host HOMO–LUMO gap. This situation satisfies the spectral overlap condition if the Stokes Shift between the absorption and emission spectra of the host and guest are not too large. However, due to the same fact, the mismatched energy levels generate carrier traps in the guest-host system, which provide another emission mechanism through direct charge trapping on the guest molecules.

In fact, it is often debated if the emission from a certain guest-host system is based on energy transfer or charge trapping. For instance, the emission of the 4-dicyanomethylene-2-methyl-6-[2-(2,3,6,7-tetrahydro-1H,5H-benzo-[i,j]quinolizin-8-yl)vinyl]-4H-pyran (DCM2):Alq_3 system is attributed to both energy transfer [62] and charge trapping [63,64] based on different observations. Another example is that both mechanisms are claimed in iridium bis(4',6',-difluorophenylpyridineato)tetrakis (1-pyrazolyl)borate (FIr6)-doped 4,4'-*N*,*N*'-dicarbazole-biphenyl (CBP) system [65].

1.5 OLED Fabrication Techniques

Vacuum Deposition

Thermal evaporation of small molecules is usually performed in a vacuum of 10^{-6} Torr or better. The evaporation rate is typically in the range of 0.1~3 Å/s. The advantages of thermal evaporation are that it enables fabrication of multilayer devices in which the thickness of each layer can be controlled accurately. It is relatively easy to pattern the pixels with proper shadow masks. The existing vacuum deposition equipment in the semiconductor industry can also be easily utilized for the production of such OLEDs.

In addition, combinatorial studies of OLEDs, in which several parameters (e.g., the thickness or composition of the layers) may be varied systematically, can be easily applied in a single deposition procedure [50]. This combinatorial fabrication greatly enhances the efficiency of systematic device fabrication aimed at optimizing the various parameters.

The disadvantage of vacuum deposition is that it always requires sophisticated

vacuum systems and is very sensitive to the evaporation conditions such as pressure, substrate temperature, degassing from the chamber, etc. In order to maintain a decent vacuum and uniformity of the organic layers the chamber size is limited and thus limits the panel size. Moreover, large amounts of organic materials are deposited on the chamber's side walls during the fabrication, which results in material waste and higher production cost.

Organic vapor-phase deposition (OVPD) was developed in part to overcome the limitations of vacuum thermal evaporation [66]. It decouples the evaporation and deposition events, using a carrier gas to mediate the transport of material from the source to the substrate, thereby achieving greater control of the deposition process. Some manufacturers also developed linear evaporation sources [67] with the substrate transferring perpendicular to a line of evaporation sources. Such geometry could deposit uniform films without a great distance between source and substrate, and also enhance the material usage.

Solution Processing

Since polymers generally crosslink or decompose upon heating, they cannot be thermally evaporated in a vacuum chamber. Hence, they are generally deposited by solution-processing, such as spin-coating and inkjet printing. Spin-coating is an established procedure in semiconducting processing [50]. Excessive amount of polymer solution is cast on the substrate, which then rotates at high speed to spread the fluid by centrifugal force.

Solution-processing is widely used in PLED and SMOLED fabrication as it is

preferable for large size production and material usage. The doping process can be easily done by mixing several organic materials, while in thermal evaporation it requires complicated co-deposition. However, solvent orthogonality requirements limit the ability of spin-coating for fabricating multilayer devices. Although the thickness of the films can be controlled by the concentration of the cast solution, the spinning speed, and the spin-coating temperature, it is difficult to fabricate thick films and the thickness obviously cannot be monitored during deposition. In addition, the lack of combinatorial fabrication and patterning methods hinders its application in display industry.

Inkjet printing is driven by the low-cost of inkjet printers. The printing head is ceramic or especially resistant to organic solvents and it is thus possible for the experimentalist to procure an ink formulation based on a wide range of solvents. The formation of the droplet may be by mechanical compression of the ink through a nozzle (piezoelectric) or by heating the ink. The droplet is then electrostatically charged and accelerated towards the substrate by an electric field. This technique has the advantage of high resolution of up to ~1200 dpi [68]. In contrast to most other wet-coating techniques there is no need for a complex master. A disadvantage is possibly a limitation of printing speed.

As motivated by the need for fast and cost-effective OLED fabrication, roll-to-roll methods are believed to be the most realistic way for massive OLED production. Shown in Fig. 1-8 are many types of roll coating and printing systems, e.g. knife-over-edge, slot-die printing, gravure printing and meniscus printing, which can

be used for OLED fabrication.

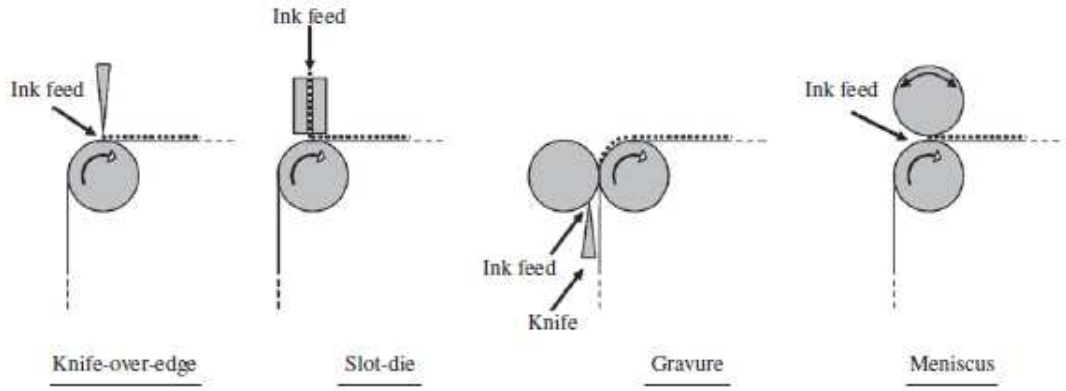

Fig. 1-8 Schematic drawings of roll coating and printing systems. The coating roller and coating unit are shown in grey shading. The web is shown as a thin line and the coated material is shown as dotted line [68].

1.6 OLED Efficiencies

Efficiency plays a very important role in the research and development of OLEDs as it is not only a key issue for energy-consumption, but also for the device lifetime. The ability to operate an OLED at a lower input power at a given luminance decreases the Joule heating and the speed of degradation.

For general research purposes, OLED's efficiency can be characterized in two ways – luminance efficiency and power efficiency with the units Cd/A and lm/W, respectively. The luminance efficiency describes how much light power was emitted in a certain direction under a certain current injection. The power efficiency describes the total light flux in the front direction under a certain operating power. It is also widely used to give an idea about how much perceived optical power (luminous power) can be generated per unit input electrical power. This provides a direct energy basis for comparison between different lighting technologies. However, in order to understand the basic mechanism of the OLED, EQE, i.e., the ratio of the number of

photons extracted toward the front to that of electrons flowing through the external driving circuit, is also measured. It can be described as the multiplication of four factors:

$$\eta_{\mathrm{E}} = \xi\gamma r_{\mathrm{ST}}\Phi_{\mathrm{PL}} \qquad (1.16)$$

Where Φ_{PL} is the PL quantum yield of the emitting species, γ is the charge balance factor, r_{ST} is the fraction of radiative excitons and ξ is the outcoupling efficiency.

The luminescent quantum yield Φ_{PL} is largely dependent on the material design and synthesis. While Φ_{PL} of many dyes is close to 100% in solution, it drops sharply in films since the increased concentration of the dye quenches the PL; this behavior is known as “concentration quenching” or “self quenching”. Guest-host systems or dendrimers are largely used to produce efficient emitting systems [12,13,40].

The charge balance factor $\gamma \leq 1$ is a measure of the balance between the hole and electron injection and the probability of their recombination. This factor is optimized by varying the composition and thickness of the charge transport layers and the energy barrier of the carrier injection through monitoring the response of the Luminance-*J*-*V* curves. Charge balance was found to be very important to achieve efficient and stable devices [69,70]. Optimized device architectures lead to low turn-on voltage and extensive carrier injections. The excessive charges can cause a drop in the efficiency due to unbalanced injection and ohmic heating, which results in a much shorter device lifespan.

As mentioned in Sec. 1.4, from spin-statistics, r_{ST} is 25% for fluorescent OLEDs. Studies have shown that the actual factor is higher due to TTA into SEs [56-59].

However, it still cannot be compared to the exciton usage in efficient electrophosphorescent OLEDs, in which the emission is due to allowed radiative decay of TEs. Spin-orbit coupling, owing to the heavy metal core, mixes the triplet states with singlet character, enabling the radiative transition of the TEs and encourages ISC from the SE to the TE state. Phosphorescent OLEDs are extensively studied and the up-to-date η_E has reached ~63% [16].

The outcoupling factor ξ describes the ratio of light extracted out of the device to that generated internally. Since OLEDs are planar multilayer structures, the inside photons inside experience layers with different refractive indices before exiting the substrate. As shown in Fig. 1-9, total internal reflection (TIR) at the interfaces results in trapped modes in the substrate and ITO/organic layers with only a small fraction of the light extracted forward.

Simulations based on classical ray optics have shown that the outcoupling efficiency ξ can be obtained by integrating the intensity over the surface-escape cone and taking the ratio to the hemispherical emission:

$$\xi = \int_0^{\theta_c} sin\theta d\theta = 1 - cos\theta_c = 1 - \sqrt{1 - \frac{1}{n^2}} \approx \frac{1}{2n^2} \qquad (1.16)$$

where *n* is the refractive index of the organic layer.

Based on this analysis, only ~20% of the internal photons escape in the front direction [13]. Further studies indicated that ~40-60% are waveguided and confined within the ITO/organic layers and ~20-40% are trapped in the glass substrate due to the TIR at the glass/air interface [71,72]. This situation imposes challenges on further enhancing the efficiency of OLED.

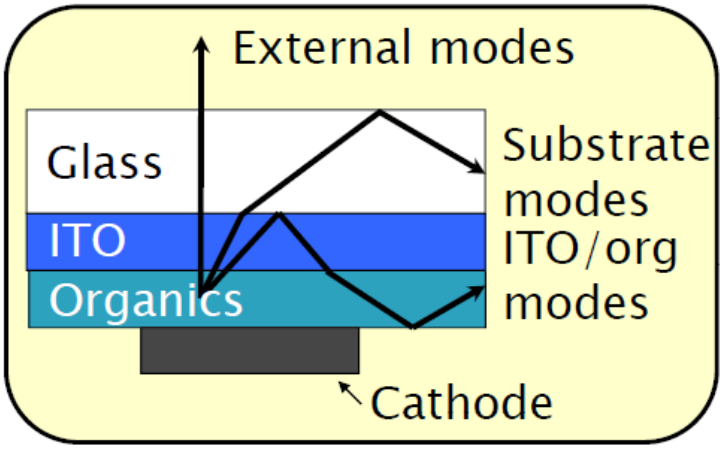

Fig. 1-9 Schematic drawing of external modes, substrate modes and ITO/organic modes in an OLED structure.

To achieve better light extraction, various methods have been utilized, which can be classified into three major categories: (*i*) Modification of the emitting species, e.g., increasing the population of horizontally oriented emitting dipoles [73]; (*ii*) Modification of the ITO/substrate structure or interface [14,16,74,75]; (*iii*) Modification of the substrate/air interface [15,76-78]. Recent studies have also shown that optimizing cavity effects and plasmon modes coupled with reflecting electrodes are also of major importance, affecting the outcoupling efficiency. Optimizing the ETL thickness can alleviate cavity-related losses and lead to an optimized device efficiency with the *J-V* characteristic maintained when using a highly conductive n-doped transport layer [79].

1.7 OLED-based PL Sensing Platforms

PL-based chemical and biological sensors are sensitive and suitable for various applications in areas such as environmental, medical, chemical and agricultural industries [10,80]. The sensors are typically composed of an analyte-responsive luminescent sensing component, a light source that excites the PL, and a

photodetector (PD). Applying an OLED as the excitation source in such platforms for (bio)chemical analytes and food pathogen detection have gained significant attention due to potential low cost, high sensitivity, and ease of OLED fabrication and possibility of integration with microfluidic channels and thin-film PDs [10,11,80]. Light sources such as diode lasers and LEDs typically require a complicated design (optical fibers, couplers, lens, mirrors, etc.) for incorporation into compact devices. In contrast, as shown in Fig. 1-10, the OLED-based sensing platform can be easily integrated with common substrates and miniaturized sensing structures. Our group has recently demonstrated that OLEDs are promising light sources for a uniquely simple structurally integrated PL-based sensor platform that includes miniaturized sensor arrays for high throughput, multianalyte analysis [10,11,81-86].

As mentioned, the OLED-based sensor is typically composed of three basic components: the OLED excitation source, the sensor film, whose PL is subject to change with the analyte type, concentration and reactions, and the PD. These three components can be arranged in either front detection or back detection geometries, as shown in Fig. 1-10. In the front detection geometry, the OLEDs and photodetector are placed on two different sides of the sensor film, while in the back detection geometry they are on the same side. The back detection geometry prevents direct illumination of the excitation light on the PD and hence, typically enhances the signal to noise ratio, resulting in easier data collection and a more compact architecture.

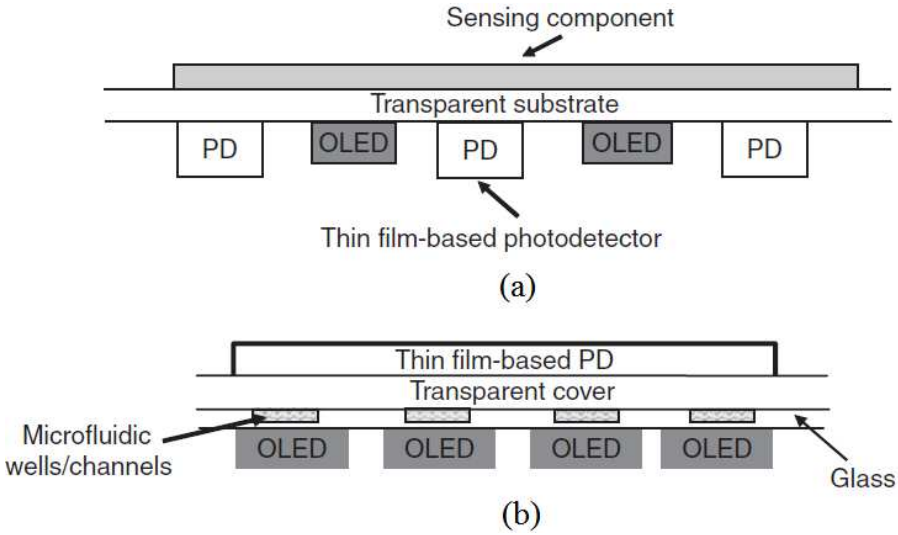

Fig. 1-10 Schematic drawing of (a) back detection and (b) front detection geometries[10].

Among all applications, OLED-based O_2 and pH sensors are especially attractive as they are very important in cultivation and bioprocess monitoring. Additionally, the O_2 sensing enables the detection of a wide variety of analytes such as glucose, lactate, ethanol, etc. that consume oxygen in the presence of their specific oxidase enzmes [85]. The ground state of O_2 is a triplet, which makes the O_2 molecule an efficient quencher of triplet excited states. Hence, phosphorescent dyes such as PtOEP (quantum yield ~50% in film and ~100 μs intrinsic decay time [87]) and palladium octaethylporphine (PdOEP) (~1 ms intrinsic decay time [81]) are very promising for effective O_2 detection based on their PL quenching.

If we assume the excitation level is constant, then the exciton generation rate R_{exc} would stay unchanged. In the presence of oxygen, there are 3 possible ways for exciton decay to the ground state as shown in Eq. (1.17) with the O_2 quenching rate related to O_2 concentration.

$$\begin{cases} \text{Radiative Channel} & A^* \xrightarrow{k_r} A + hv \\ \text{Nonradiative Channel} & A^* \xrightarrow{k_{nr}} A + phonon \\ \text{O}_2 \text{ Quenching Channel} & A^* \xrightarrow{k_q[\text{O}_2]} A + {\text{O}_2}^* \end{cases} \quad (1.17)$$

Consequently, in steady state the exciton decay rate equation is

$$\frac{\mathrm{d}N_0}{\mathrm{d}t} = R_{\text{exc}} - k_r N_0 - k_{nr} N_0 = 0 \quad (1.18)$$

$$\frac{\mathrm{d}N}{\mathrm{d}t} = R_{\text{exc}} - k_r N - k_{nr} N - k_q[\text{O}_2] N = 0 \quad (1.19)$$

where N_0 is the exciton population in absence of O_2 and N is that with O_2.

Eq. (1.18) & (1.19) are differential equations with time constants:

$$\tau_0 = \frac{1}{k_r + k_{nr}} \quad (1.20)$$

$$\tau = \frac{1}{k_r + k_{nr} + k_q[\text{O}_2]} \quad (1.21)$$

Assuming the radiative decay rate is not affected by the presence of O_2, the PL intensities I_0 and I are only related to N_0 and N, respectively. By solving Eqs. (1.18) & (1.19) and comparing Eq. (1.20) & (1.21), we could derive the following relations:

$$\frac{I_0}{I} = \frac{\tau_0}{\tau} = 1 + \frac{k_q}{k_r + k_{nr}}[\text{O}_2] = 1 + K_{SV}[\text{O}_2] \quad (1.22)$$

Eq. (1.22) is the Stern-Volmer equation. It indicates that the ratio of the PL intensity or decay time in absence of O_2 to that in the presence of O_2 is linear with $[O_2]$. Indeed as shown in Fig. 1-11(a), when a PtOEP: polystyrene (PS) film is excited by a pulsed green LED, both the PL intensity and decay time decrease as $[O_2]$ increases. The linear relation shown in Eq. (1.22) is demonstrated in Fig. 1-11(b).

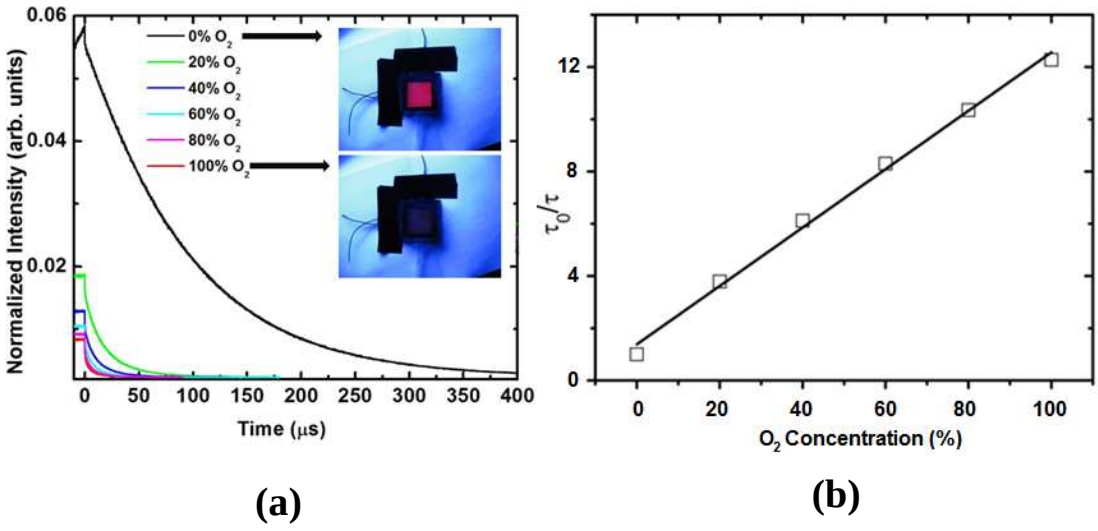

Fig. 1-11 (a) The PL decay curves of a PtOEP:PS film excited by a pulsed green LED at different O_2 concentrations; the inset shows the photographs of the excited film at 0% and 100% O_2. (b) The corresponding Stern-Volmer plot.

Although both *I* and τ are related to the analyte concentration, the τ mode is preferably used since the decay time is an intrinsic quantity, independent of the light intensity. Thus, minor changes in the background light, the sensing probe, or the excitation source do not affect sensor performance. In this way, frequent calibration and a reference pixel are avoided. Furthermore, pulsed operation reduces heat dissipation and enhances the lifetime of OLEDs. It also shortens the light exposure of the sensing film, resulting in reduced photobleaching.

With the relatively short decay of fluorescent OLEDs (SE lifetime is usually shorter than 10 ns) and the rather long decay time of PtOEP (~3-100 μs) and PdOEP (~5-1000 μs) [87], it appears that the distortion of the PL signal by the excitation light can be prevented. However, in some guest-host OLEDs, charge migration and detrapping processes dominate light generation at the turn-off edge of the pulsed OLED due to the low mobility of charge carriers in organic materials. This issue

affects data analysis in some sensor platforms and needs to be alleviated, as discussed later.

1.8 Dissertation Organization

This dissertation is comprised of 7 chapters. Chapter 1 is a general introduction to OLEDs and OLED-based PL sensors. Chapter 2 describes the transient emission mechanism of guest-host OLEDs both experimentally and theoretically. Chapter 3 demonstrates a monolithic and easy-to-apply process for fabricating multicolor microcavity OLEDs (that improve the sensor platform). Chapter 4 addresses the outcoupling issues of OLEDs at the substrate/air interface by using a microstructured polymer film resulting from a PS and polyethylene glycol (PEG) mixture. Based on the understanding of OLEDs and their improvement described in Chapters 2-4, research was done in order to realize integrated all organic-based O_2 and pH sensors with improved signal intensity and sensitivity. The sensor design modification and optimization are summarized in Chapters 5 & 6. Finally, the conclusions are summarized in Chapter 7.

References

1. A. Bernanose, M. Comte, P. Vouaux, J. Chim. Phys. **50**, 65 (1953).
2. M. Pope, H.P. Kallmann, P. Magnante, J. Chem. Phys. **38**, 2042 (1963).
3. C. W. Tang, S. A. VanSlyke, Appl. Phys. Lett. **51**, 913 (1987).
4. J. H. Burroughs, D. D. C. Bradley, A. R. Brown, R. N. Marks, K. Mackay, R. H. Friend, P. L. Burns, A. B. Holmes, Nature **347**, 539 (1990).
5. G. Gustafsson, Y. Cao, G. M. Treacy, F. Klavetter, N. Colaneri, A. J. Heeger,

Nature **357**, 477 (1992).

6. J. Kido, K. Hongawa, K. Okuyama, K. Nagai, Appl. Phys. Lett. **64**, 815 (1994).
7. R. H. Friend, R. W. Gymer, A. B. Holmes, J. H. Burroughes, R. N. Marks, C. Taliani, D. D. C. Bradley, D. A. Dos Santos, J. L. Brédas, M. Lögdlund, W. R. Salaneck, Nature **397**, 121 (1999).
8. S. R. Forrest, Nature **428**, 911 (2004).
9. R. F. Service, Science **310**, 1762 (2005).
10. R. Shinar, J. Shinar, eds., *Organic Electronics in Sensors and Biotechnology* (McGraw-Hill, 2009).
11. F. So, ed., *Organic Electronics: Materials, Processing, Devices and Applications* (CRC, 2010).
12. M. A. Baldo, D. F. O'Brien, Y. You, A. Shoustikov, S. Sibley, M. E. Thompson, S. R. Forrest, Nature **395**, 151 (1998).
13. C. Adachi, M. A. Baldo, M. E. Thompson, S. R. Forrest, J. Appl. Phys. **90**, 5048 (2001).
14. Y.Sun, S. R. Forrest, Nature Photonics **2**, 483 (2008).
15. S. Reineke, F. Lindner, G. Schwartz, N. Seidler, K. Walzer, B. Lüssem, K. Leo, Nature **459**, 234 (2009).
16. Z. B. Wang, M. G. Helander, J. Qiu, D. P. Puzzo, M. T. Greiner, Z. M. Hudson, S. Wang, Z. W. Liu, Z. H. Lu, Nature Photonics **5**, 753 (2011).
17. M. Koeste, P. Rensing, G. van Heck, R. Sharpe, B. Allard, F. Wieringa, P. Kruijt, N. Meulendijks, H. Jansen, H. Schoo, Proc. SPIE **7054**, 7054I (2008).

18. http://www.oled-info.com/microsoft-research-shows-3d-interactive-desktop-using -transparent-oled.

19. P. E. Burrows, V. Bulovic, S. R. Forrest, L. S. Sapochak, D. M. McCarty, M. E. Thompson, Appl. Phys. Lett. **65**, 2922 (1994).

20. A. B. Chwang, M. A. Rothman, S. Y. Mao, R. H. Hewitt, M. S. Weaver, J. A. Silvernail, K. Rajan, M. Hack, J. J. Brown, X. Chu, L. Moro, T. Krajewski, N. Rutherford, Appl. Phys. Lett. **83**, 413 (2003).

21. H. You, Y. Dai, Z. Zhang, D. Ma, J. Appl. Phys. **101**, 026105 (2007).

22. L. Duan, D. Zhang, K. Wu, X. Huang, L. Wang, Y. Qiu, Adv. Funct. Mater. **21**, 3540 (2011).

23. http://www2.dupont.com/Displays/en_US/news_events/article20090527.html.

24. www.oled.com, www.displaysearch.com, www.isuppli.com.

25. D. J. Milliron, I. G. Hill, C. Shen, A. Kahn, J. Schwartz, J. Appl. Phys. **87**, 572 (2000).

26. F. Nüesch, E. W. Forsythe, Q. T. Le, Y. Gao, L. J. Rothberg, J. Appl. Phys. **87**, 7973 (2000).

27. M. G. Helander, Z. B. Wang, J. Qiu, M. T. Greiner, D. P. Puzzo, Z. W. Liu, Z. H. Lu, Science **332**, 944 (2011).

28. J.C. Scott, G. Malliaras, W.D. Chen, J. Breach, J. Salem, P. Brock, S. Sachs, C. Chidsey, Appl. Phys. Lett. **74**, 1510 (1999).

29. A. J. Makinen, I. G. Hill, R. Shashindhar, N. Nikolov, Z.H. Kafafi, Appl. Phys. Lett. **79**, 557 (2001).

30. N. Koch, A. Kahn, J. Ghijsen, J.-J. Pireaux, J. Schwartz, R.L. Johnson, A. Elschner, Appl. Phys. Lett. **82**, 70 (2003).

31. A.M. Nardes , M. Kemerink, M.M. de Kok, E. Vinken, K. Maturova, R. A. J. Janssen, Organic Electronics **9**, 727 (2008).

32. S. Kirchmeyer, K. Reuter, J. Mater. Chem. **15**, 2077 (2005).

33. K. Fehse, K. Walzer, K. Leo, W. Lövenich, A. Elschner, Adv. Mater. **19**, 441 (2007).

34. M. Cai, T. Xiao, R. Liu, Y. Chen, R. Shinar, J. Shinar, Appl. Phys. Lett. **99**, 153303 (2011).

35. W. M. Haynes, Ed., *CRC handbook of Chemistry and Physics* (Taylor and Francis 2008).

36. L. S. Hung, C. W. Tang, M. G. Mason, Appl. Phys. Lett. **70**, 152 (1997).

37. G. E. Jabbour, B. Kippelen, N. R. Armstrong, N. Peyghambarian, Appl. Phys. Lett. **73**, 1185 (1998).

38. S. H. Kim, J. Jang, J. Y. Lee, Appl. Phys. Lett. **91**, 103501 (2007).

39. J. Huang, G. Li, E. Wu, Q. Xu, Y. Yang, Adv. Mater. **18**, 114 (2006).

40. P. Burn, S. Lo, I. Samuel, Adv. Mater. **19**, 1675 (2007).

41. S. Chen, L. Deng, J. Xie, L. Peng, L. Xie, Q. Fan, W. Huang, Adv. Mater. **22**, 5227 (2010).

42. T. Matsumoto, T. Nakada, J. Endo, K. Mori, N. Kawamura, A. Yokoi, J. Kido, SID Digest. **34**, 979 (2003).

43. L. S. Liao, K. P. Klubek, C. W. Tang, Appl. Phys. Lett. **84**, 167 (2004).

44. L. S. Liao, W. K. Slusarek, T. K. Hatwar, M. L. Ricks, D. L. Comfort, Adv. Mater. **20**, 324 (2008).

45. T.-W. Lee, T. Noh, B.-K. Choi, M.-S. Kim, D. W. Shin, J. Kido, Appl. Phys. Lett. **92**, 043301 (2008).

46. S. Schols, *Device Architecture and Materials for Organic Light-Emitting Devices*, (Springer 2011).

47. S.M. Sze, *Physics of Semiconductor Devices* (John Wiley & Sons 2007).

48. P. Vacca, M. Petrosino, A. Guerra, R. Chierchia, C. Minarini, D. Della Sala, A. Rubino, J. Phys. Chem. C **111**, 17404 (2007).

49. D. Braun, A. J. Heeger, Appl. Phys. Lett. **58**, 1982 (1991).

50. J. Shinar ed., *Organic Light-Emitting Devices: A Survey* (Springer 2003).

51. L. Bozano, S. A. Carter, J. C. Scott, G. G. Malliaras, P. J. Brock, Appl. Phys. Lett. **74**, 1132 (1999).

52. M. Pope, C.E. Swenberg, *Electronic Processes in Organic Crystals and Polymers* (Oxford 1999).

53. M.A. Lampert, Phys. Rev. **103**, 1648 (1956).

54. T. Mori, T. Ogawa, D. Cho, T. Mizutani , Appl. Sur. Sci. **212**, 458 (2003).

55. P. E. Burrows, Z. Shen, V. Bulovic, D. M. McCarty, S. R. Forrest, J. A. Cronin, M. E. Thompson, J. Appl. Phys. **79**, 7991 (1996).

56. M. Wohlgenannt, K. Tandon, S. Mazumdar, S. Ramasesha, Z. V. Vardeny, Nature **409**, 494 (2001).

57. J. S. Wilson, A. S. Dhoot, A. J. A. B. Seeley, M. S. Khan, A. Köhler, R. H. Friend,

Nature **413**, 828 (2001).

58. J. Kido, Y, Iizumi, Appl. Phys. Lett. **73**, 2721 (1998).

59. D. Y. Kondakov, J. Appl. Phys. **102**, 114504 (2007).

60. K. Goushi, K. Yoshida, K. Sato, C. Adachi, Nature Photonics **6**, 253 (2012).

61. J. H. Park, J. H. Seo, S. H. Lim, G. Y. Ryu, D. M. Shin, Y. K. Kim, Journal of Physics and Chemistry of Solids **69**, 1314 (2008).

62. V. Bulovic, A. Shoustikov, M.A. Baldo, E. Bose, V.G. Kozlov, M.E. Thompson b, S.R. Forrest, Chemical Physics Letters **287**, 455 (1998).

63. K. O. Cheon, J. Shinar, Appl. Phys. Lett. **81**, 1738 (2002).

64. F. Nüesch, D. Berner, E. Tutiš, M. Schaer, C. Ma, X. Wang, B. Zhang, L. Zuppiroli, Adv. Funct. Mater. **15**, 323 (2005).

65. K.-R. Wee, W.-S. Han, H.-J. Son, S. Kwon, S. O. Kang, J. Phys. D: Appl. Phys. **42**, 235107 (2009).

66. M. Shtein, H. F. Gossenberger, J. B. Benziger, S. R. Forrest, J. Appl. Phys. **89**, 1470 (2001).

67. S. A. VanSlyke, A. Pignato, D. Freeman, N. Redden, D. Waters, H. Kikuchi, T. Negishi, H. Kanno, Y. Nishio, M. Nakai, Proceedings of the Society for Information Display, Digest of Technical Papers **33**, 886 (2002).

68. F. C. Krebs, Solar Energy Materials & Solar Cells **93**, 394 (2009).

69. N. Chopra, J. Lee, Y. Zheng, S.-H. Eom, J. Xue, F. So, ACS Appl. Mater. Interfaces **1**, 1169 (2009).

70. Y.-J. Pu, G. Nakata, F. Satoh, H. Sasabe, D. Yokoyama, J. Kido, Adv. Mater. **24**,

1765 (2012).

71. G. Gu, P.E. Burrows, S. Venkatesh, S.R. Forrest, M.E. Thompson, Opt. Lett. **22**, 396 (1997).
72. A. Chutinan , K. Ishihara, T. Asano, M. Fujita, S. Noda, Organic Electronics **6**, 3 (2005).
73. J. Frischeisen, D. Yokoyama, A. Endo, C. Adachi, W. Brütting, Organic Electronics **12**, 809 (2011).
74. W. H. Koo, S. M. Jeong, F. Araoka, K. Ishikawa, S. Nishimura, T. Toyooka, H. Takezoe, Nature Photonics **4**, 222 (2010).
75. A. O. Altun, S. Jeon, J. Shim, J.-H. Jeong, D.-G. Choi, K.-D. Kim, J.-H. Choi, S.-W. Lee, E.-S. Lee, H.-D. Park, J. R. Youn, J.-J. Kim, Y.-H. Lee, J.-W. Kang, Organic Electronics **11**, 711 (2010).
76. Y. Sun, S. R. Forrest, J. Appl. Phys. **100**, 073106 (2006).
77. J.-M. Park, Z. Gan, W.Y. Leung, R. Liu, Y. Zhou, K. Constant, J. Shinar, R. Shinar, K.-M. Ho, Optics Express **19**, A786 (2011).
78. R. Liu, Z. Ye, J.-M. Park, M. Cai, Y. Chen, K.-M. Ho, R. Shinar, J. Shinar, Optics Express **19**, A1272 (2011).
79. M. Furno, R. Meerheim, S. Hofmann, B. Lüssem, K. Leo, Phys. Rev. B **85**, 115205 (2012).
80. O. S. Wolfbeis, Anal. Chem.**72**, 81 (2000).
81. J. Shinar, R. Shinar, J. Phys. D: Appl. Phys. **41**, 133001 (2008).
82. V. Savvate'ev, Z. Chen-Esterlit, J. W. Aylott, B. Choudahury, C.-H. Kim, L. Zou,

R. Shinar, J. Shinar, R. Kopelman, Appl. Phys. Lett. **81**, 4652 (2002).

83. B. Choudhury, R. Shinar, J. Shinar, J. Appl. Phys. **96**, 2949 (2004).

84. Z. Zhou, R. Shinar, A. J. Allison, J. Shinar, Adv. Funct. Mater. **17**, 3530 (2007).

85. Y. Cai, R. Shinar, Z. Zhou, J. Shinar, Sensors and Actuators B **134**, 727(2008).

86. R. Liu, Y. Cai, J.-M. Park, K.-M. Ho, J. Shinar, R. Shinar, Adv. Funct. Mater. **21**, 4744 (2011).

87. Y. Amao, Microchim. Acta **143**, 1 (2003).

Chapter 2. Comprehensive Investigation of Transient Electroluminescence Spikes in SMOLEDs

Modified from R. Liu, Z. Gan, R. Shinar, J. Shinar,

Phys. Rev. B **83**, 245302 (2011).

Abstract

A comprehensive study of transient ns electroluminescence (EL) spikes that exceed the dc level and μs-long EL tails following a bias pulse in guest-host small molecular organic light-emitting diodes (SMOLEDs), including relatively efficient devices, which elucidates carrier and exciton dynamics in such devices, is presented. The transient EL is strongly dependent, among other parameters, on device materials and structure. At low temperatures, all measured devices, with the exception of Pt octaethylporphyrin (PtOEP)-doped tris(8-hydroxyquinoline) Al (Alq_3) SMOLEDs, exhibit the spikes at ~70-300 ns. At room temperature (RT), however, only those with a hole injection barrier, carrier-trapping guest-host emitting layer, and no strong electron-transporting and hole-blocking layer (such as 4,7-diphenyl-1,10-phenanthroline (BPhen)) exhibit strong spikes. These narrow and appear earlier under post-pulse reverse bias. To further elucidate the origin of the spikes, we monitored their dependence on the pulsed bias width and voltage, the doped layer thickness, and its location within the OLED structure. The characteristics of the μs-long tails were also evaluated through the effect of the post-pulse voltage. A model based on the recombination of correlated charge pairs (CCPs) and on charge detrapping is presented; the model agrees well with the experimental data. The results suggest that

reduced electric field-induced dissociative quenching of singlet excitons is responsible for the spikes' amplitude exceeding the on-pulse dc EL level. The long tails are attributed to recombination of charges detrapped from a distribution of shallow, mostly host, sites, reminiscent of the detrapping and recombination processes that yield the thermally stimulated luminescence of such materials. The comprehensive transient EL measurements in guest-host devices demonstrate the generality of the strong spike phenomenon in devices with charge trapping in the emitting guest molecules. Hence the transient EL can serve as an important tool to identify the dominant emitting mechanisms in the guest-host systems.

2.1 Introduction

Thin film organic light emitting diodes (OLEDs) have advanced dramatically since they were first described [1]. They are comprised of one or multiple organic semiconducting layers, with a total thickness of ~100 nm, sandwiched between two electrodes. They exhibit great promise in various applications such as displays, solid-state lighting, and chemical and biological sensing [2-7]. However, despite growing interest and applications, fundamental processes that affect device performance, such as carrier transport and recombination, as well as electroluminescence (EL) quenching, in particular following a bias pulse, remain to be understood. In this study, we address these processes in small molecular OLEDs (SMOLEDs), which dominate OLED-based applications.

Most studies that address the above-mentioned processes focus on the behavior under dc voltage, with much less treatment of the transient behavior and its relation to

device performance [8-18]. Among these studies, other than research concentrated on triplet-triplet annihilation (TTA) in long EL decay processes [14,15], only a few transient EL studies on polymer LEDs (PLEDs) [8-10] and on 4,4'-bis(2,2'-diphenylvinyl)-1,1'-biphenyl (DPVBi)-based SMOLEDs [16,17] reported intriguing EL spikes following a bias pulse. Such spikes were also observed in (8-hydroxyquinoline) Al (Alq_3)-based [18] SMOLED but they were not analyzed. The observations reported in this paper point to these spikes as a general phenomenon in SMOLEDs, including relatively efficient devices, when charge trapping processes occur and, hence, result in a more comprehensive treatment of the transient EL behavior and its implications regarding the choice of OLED materials and device architecture. Additionally, as discussed later, the transient EL behavior may point to the light emission mechanism, whether dominated by energy transfer from host to guest or by direct carrier trapping on the guest.

As is well known, the transport of carriers in amorphous organic solids is based on hopping between shallow localized states [5-7], which is due to energetic or structural disorder and impurities. Traps within organic materials tend to retain charges for relatively long periods, as demonstrated by, e.g., thermally stimulated luminescence [19], indicating that such long-lived trapped charges can survive after the external field is turned off. Unless they reach the appropriate electrode, such charges eventually form correlated charge pairs (CCPs) with an opposite mobile charge within the Onsager radius (19 nm at room temperature neglecting screening by other charges; <<19 nm if not) [17,20]. The recombination of these carriers following a bias pulse

will consequently affect the transient behavior of the OLEDs, both electrically and optically.

In this paper, a detailed investigation of transient EL spikes observed at 70 – 300 ns and tails extending to several μs following a bias pulse in efficient SMOLEDs is described. The effect of materials and other parameters/attributes of the various layers of the SMOLEDs are discussed, including the effect of temperature and post-pulse forward and reverse bias. The OLEDs studied comprised of all or part of the following layers: anode/hole injection layer (HIL)/hole transport layer (HTL)/guest-host emitting layer (EML)/hole blocking and electron transporting layer (HBL and ETL, respectively)/electron injection layer/metal cathode. Specific examples include EL spikes and tails in devices with coumarin6 (C6)-doped Alq_3) as the EML and copper phthalocyanine (CuPc) as the HIL. Since the highest occupied molecular orbital (HOMO) energy of C6 is $E_{HOMO} \approx$ -5.4 eV, it becomes a hole trapping center when doped into Alq_3, where $E_{HOMO} \approx$ -5.9 eV. Hence, in this case (and other cases of a dopant that traps h^+ or e^- due to its energy levels relative to the host), most of the CCPs will involve a relatively deeply trapped h^+ on the C6 and a relatively mobile e^- hopping among the Alq_3 molecules around it. Thus the e^- will eventually recombine with the h^+ to form an exciton on the C6.

The dependence of the spikes and tails on parameters such as the thickness of the doped layer and its distance from the HTL (*N*,*N*'-bis(naphthalen-1-yl)-*N*,*N*'-bis(phenyl)benzidine (α-NPB))/Alq_3 interface, the on-pulse voltage, the pulse duration, and the time the device was exposed to air are discussed. The strong effects

of the HIL, whether absent, CuPc, or MoO_3, and of the ETL/HBL, are also discussed. Moreover, a model based on the observed phenomena is presented; the model is in good agreement with the experimental data. Based on the model and the experiments, the observed EL spikes are attributed to the recombination of CCPs, and the longer emission tails to recombination of initially unpaired, uncorrelated charges. Transient EL exhibiting spikes and tails observed in other doped devices are also presented. This comprehensive study highlights universal aspects of SMOLED performance. It points to the strong role of materials and device design as well as electric field-induced dissociative quenching of singlet excitons (SEs) (whose radiative decay yields the EL). The contribution from a "back-drift" of holes that have leaked through the recombination zone (RZ) toward the cathode and drift back toward the RZ in causing the EL spikes, as proposed for some PLEDs, is most likely marginal. Importantly, no spike is observed, even at low temperature, in a guest-host system where efficient energy transfer to a long-lived (τ_{rad} ~ 100 μs) phosphorescent guest, rather than charge trapping on it, dominates. This behavior can possibly provide a novel way to distinguish between energy transfer and charge trapping processes in guest-host systems.

2.2 Experimental methods

21×21 OLED pixel arrays (pixel diameter ~1.5 mm) were fabricated combinatorially [21]. All depositions were performed in a conventional thermal vacuum evaporation chamber (base pressure ~10^{-6} Torr; the organic layers' deposition rate was ~1 Å/s) installed inside a glove box with <20 ppm O_2. The bias pulses were

generated by an Avtech Model AV-1011 power supply with a nominal rise and fall times of ~10 ns. The EL was monitored by a Hamamatsu R6060-02 photomultiplier tube (PMT) with a 50 Ω external load connected to a 350 MHz oscilloscope. For low temperature measurements, the OLED pixels' size was 2×2 mm^2. The devices were placed in a small chamber with a transparent window on one side. The EL was detected through that window using the PMT. Due to the geometry of the setup the PW in the low-temperature measurements was set to 1 ms to improve detection. As shown in the inset of Fig. 2-5, however, the difference in A_{spike} using PWs of 100 μs and 1 ms is modest. Note that there were some variations in A_{spike} from batch to batch, with the overall behavior reproducible.

2.3 Results and discussion

Following a bias pulse applied to an OLED several processes responsible for the post-pulse EL in fluorescent SMOLEDs occur [22]. These processes include:

(1) EL decay of pre-existing excitons, i.e., those formed during the pulse. This decay process usually takes a few ns for SEs [11,23].

(2) EL decay of SEs formed during the falling edge of the voltage pulse. Carriers are continuously injected into the device while the voltage is decaying, which in this work lasted for ≤ 50 ns [24]. The decaying external field also continues to drive the pre-existing electrons e^- and holes h^+ from the bulk of the transporting layers into the RZ (which we approximate to coincide with the EML) to form excitons. The EL generated from these excitons, as well as from the pre-existing excitons of (1), results in an EL amplitude similar to that observed during the pulse.

(3) Recombination of initial CCPs (i.e., those present at t ~50 ns after the end of the pulse). Even after the external field decays, charges within the RZ that are Coulombically bound, i.e., CCPs, recombine. The recombination of these charge pairs is believed to generate the EL spikes that are up to > 3 times larger than the on-pulse (dc) EL level. As discussed below, the intriguing strength of these EL spikes is suspected to be due to reduced electric-field-induced dissociative quenching of SEs as the applied field is turned off and the internal field due to the dissipating charge accumulation layers decays. An alternative mechanism, whereby increased CCP generation from holes that have leaked through the RZ, continued to drift toward the cathode, but now turn back toward the RZ in greater numbers due to the absence of an applied field [22], is most likely marginal in generating the spikes.

(4) Recombination of newly formed CCPs. Detrapped charges originating mostly from host shallow states continue to pair with opposite charges, mostly on guest molecules, to form CCPs. Due to the relatively slow process of detrapping, the excitons generated from these CCPs yield the observed stretched exponential EL tails that extend over several microseconds.

(5) Decay of SEs formed by TTA. The fusion of the triplets generates additional SEs, whose decay contributes to the transient EL. This process approximates an exponential decay in the long time range [14]. Compared to the EL decay caused by the trapped charges, TTA is not affected by the external electric field due to the charge neutrality of the triplets.

These processes for various materials, device structures, and conditions are

discussed in detail in the following sections. We note that OLED displays can have a faster response time than standard LCD screens. While LCDs are capable of a ≤ 1 ms response time offering a frame rate ≥ 1 kHz, OLEDs are advantageous with potential response times < 10 μs (100 kHz refresh rates). However, the transient EL of OLEDs that might include a spike at ~100 ns and tails that extend to several μs (and even ms when triplet-triplet annihilation is non-negligible) present a limitation. This issue becomes increasingly acute as the display size increases. Moreover, the observed spikes and tails are already a limitation for the OLED-based luminescent biochemical sensing platform, which has been drawing considerable interest[3,4].

2.3.1. Devices with CuPc as the HIL

2.3.1-1 General Phenomena

Fig. 1 shows a typical transient EL following a 100 μs, 6 V pulse, normalized to the EL amplitude during the pulse, in devices of the general structure ITO / CuPc (5 nm) / α-NPB (50 nm) / 1 wt.% C6:Alq_3 ($0 \leq x \leq 5$ nm) / Alq_3 (40-x nm) / LiF (1 nm) / Al (~120 nm). These devices are termed A0 to A5, depending on the value of x. Strong EL spikes at ~100 ns and tails are observed in all C6-doped devices with CuPc as the HIL, but not in the undoped Alq_3 device A0. Similar spikes and tails were observed also in other device structures detailed later.

As mentioned, C6, with $E_{HOMO} \approx$ -5.4 eV, is a hole trapping fluorescent dopant in Alq_3, where $E_{HOMO} \approx$ -5.9 eV. The emission is mainly through direct recombination of CCPs at the dopant molecules, resulting from carrier trapping [25,26]. As the carriers are driven toward the RZ during the bias pulse, h^+ are trapped on the energetically

preferred sites of the C6 molecules. Although the CCPs will eventually recombine and form excitons, a considerable fraction of them and the resulting excitons could be dissociated by the electric field during the pulse, resulting in EL quenching. Research by other groups has shown that a significant amount of charges will be stored near the RZ under constant bias, causing a high internal electrical field [27,28]. It has also been shown that this field that induces SE dissociation can reduce the EL by > 60% [29,30].

After the pulse is turned off there are many remaining CCPs in the RZ due to the holes trapped on the guest molecules. Since the electric field decreases, field-induced dissociative SE quenching is reduced as well, and the flow of h^+ that have leaked through the RZ toward the cathode and now turn back to the RZ increases [8,9]. The former process is believed to contribute to the EL spikes sufficiently to result in a spike amplitude that exceeds the on-pulse EL. Newly created CCPs, formed from unpaired, detrapped (mostly host) charges, are believed to contribute only to the EL tails, due to the slow process of detrapping and the larger distance from the RZ. The undoped Alq_3 device, on the other hand, has a much weaker post-pulse EL due to the lack of guest-host-related charge trapping sites and consequently CCPs. This observation therefore provides additional strong evidence for the charge trapping mechanism in the C6:Alq_3 guest-host system.

As seen in Fig. 2-1, the relative spike amplitude A_{spike} (i.e., spike intensity normalized to the on-pulse level) increases when x increases from 0 to 2 nm. This behavior is probably due to the increasing number of guest-induced traps. However,

A_{spike} decreases in device A5 in comparison to devices A1 and A2; repeated measurements reproduced this A5 weakened A_{spike}; in other devices, where the doped layer thickness was farther increased, the spike weakened further. Assuming that during the pulse the carrier density just outside the RZ is not drastically changed when the doped layer thickness increases, in A5 the internal electric field across the RZ is likely lower than in A2, which results in lower field-induced EL quenching during the pulse and hence a relatively lower A_{spike}.

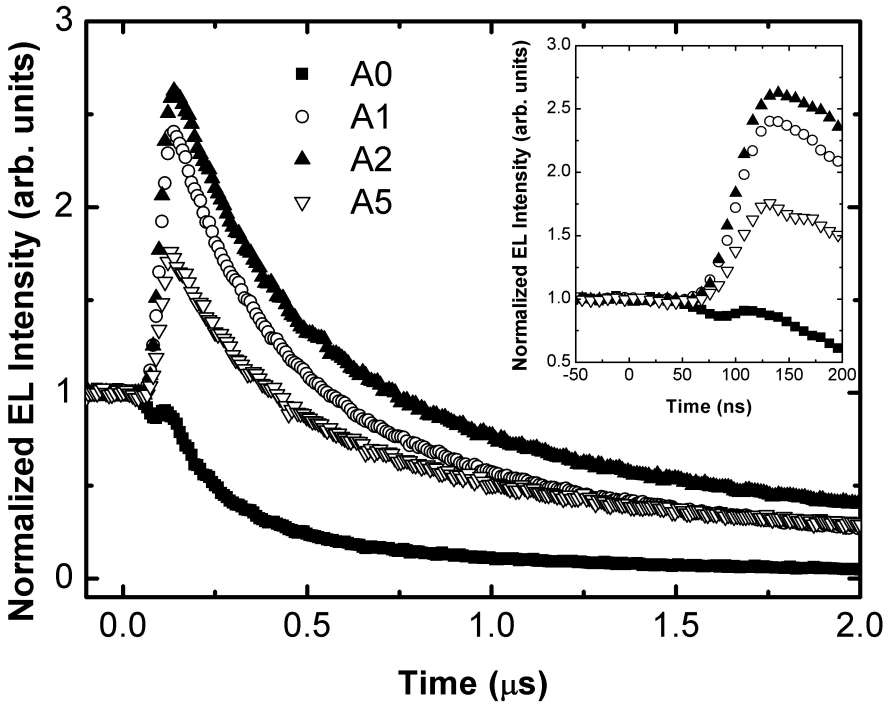

Fig. 2-1 The transient EL following a 100 μs, 6.0 V pulse of devices of the structure ITO/5 nm CuPc/50 nm α-NPB/*x* nm 1wt% C6:Alq_3/(40-*x*) nm Alq_3/1 nm LiF/~120 nm Al, termed, device A*x* (i.e., A0, A1, A2, A5). Inset: Expanded view of the transient EL up to 200 ns following the bias pulse.

To observe an EL spike, it is also important that excitons do not saturate the CCP sites. Fig. 2-2 shows A_{spike} vs voltage in devices A1, A2, and A5. As clearly seen, A_{spike} increases with the bias at low voltages, and decreases above ~6.5-7 V. Holes injected

from the anode will be either trapped on guest molecules to later form CCPs, or will recombine with e^- to form excitons in host or guest molecules. Due to the barrier for h^+ hopping from α-NPB to Alq_3, only a relatively small fraction of h^+ is supplied to the doped layer at low voltage, most of which will be rapidly trapped in the C6 guest molecules. Thus, the spike increases with bias as the trapped h^+ density in the guest molecules increases. When the bias is high (> ~6.5 V in this case), most of the guest traps are filled, and consequently the trapping rate decreases, while the guest+host exciton formation rates increase. Therefore, the relative amplitude of the spike decreases. This behavior and its analysis are similar (though not identical) to those of DPVBi-based OLEDs [16,17].

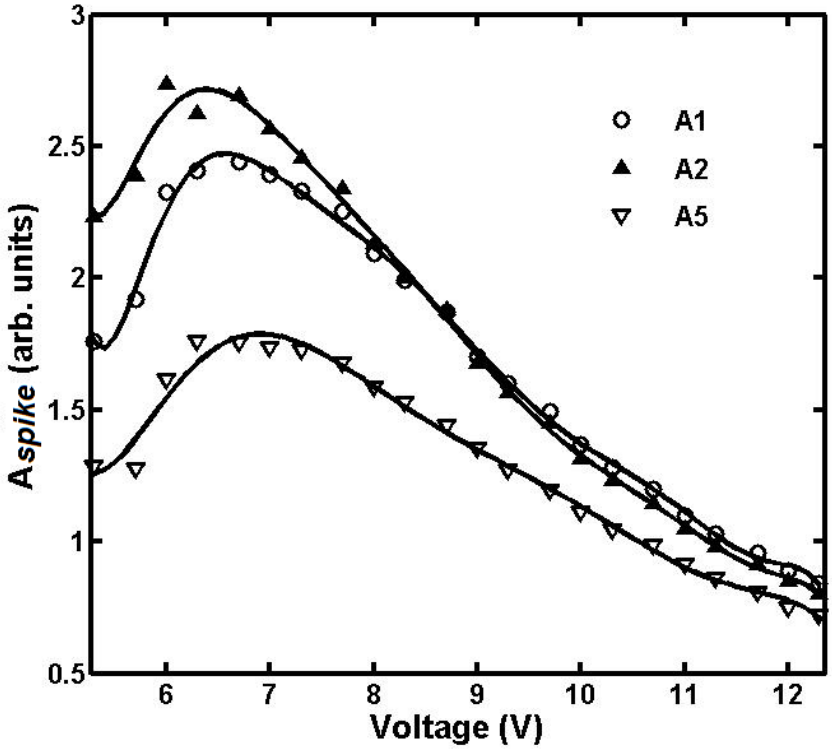

Fig. 2-2 The voltage dependence of the peak intensity of the spike in A1 (open circles), A2 (solid squares), and A5 (solid triangles). The lines are a guide to the eye.

2.3.1-2 Effects of the Doped EML Position

Fig. 2-3 confirms the crucial role of the C6:Alq_3 guest-host system in generating CCPs and hence the EL spikes. In addition to the normalized transient EL intensity of A0 and A1, it shows also the EL intensity in devices in which the 1 nm doped layer was fabricated at an increasing distance from the HTL. The general structure of these devices was ITO / CuPc (5 nm) / α-NPB (50 nm) / Alq_3 (*y* nm) / 1 wt.% C6:Alq_3 (1 nm) / Alq_3 (39-*y* nm) / LiF (1 nm) / Al (~120 nm) with $0 \leq y \leq 10$ nm; these devices are termed A1-1 to A1-10, based on the value of *y*.

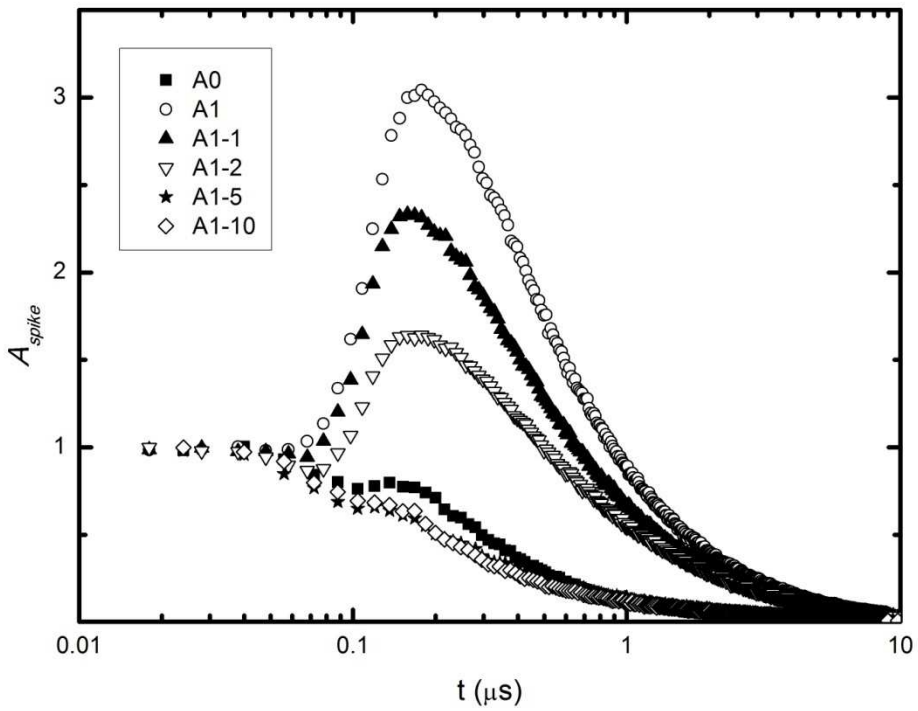

Fig. 2-3 The EL, following a 100 μs, 6.0 V pulse, of undoped Alq_3 device A0 (solid squares), C6-doped device A1 with the doped layer at the α-NPB/Alq_3 interface (open circles), and A1-based devices, A1-*y*, with the doped layer at distance *y* from the HTL, i.e., ITO/5 nm CuPc/50 nm α-NPB/*y* nm Alq_3/1 nm 1wt% C6:Alq_3/(40-*y*) nm Alq_3/1 nm LiF/~120 nm. The A1-*y* devices, according to the value of *y*, are A1-1 (solid triangles), A1-2 (open inverted triangles), A1-5 (stars), and A1-10 (open diamonds).

As seen in Fig. 2-3, the EL spike intensity decreased with increasing *y*. The h^+ energy barrier between α-NPB ($E_{HOMO} \approx$ -5.6 eV) and Alq_3 ($E_{HOMO} \approx$ -5.9 eV)

obviously generates a h^+ accumulation layer at the α-NPB/Alq_3 interface, and therefore the carrier density in the guest-host layer decreases greatly as *y* increases [27]. Hence, despite the unchanged doped-layer thickness, the carrier density in it, and consequently the CCP formation rate and its contribution to the spikes, decreases from A1-1 to A1-10. Since the contribution of h^+ that turn back toward the RZ after having drifted beyond it to the spikes should, if anything, increase with *y*, we conclude that this mechanism's contribution to the spikes is marginal.

2.3.1-3 Ambient -Induced Degradation

Fig. 2-4 shows the integrated transient EL of an unencapsulated A1 OLED as obtained from the integrated area Q_{tot} and the normalized (relative to the 'on-pulse' level) integrated area Q_N vs operation time.

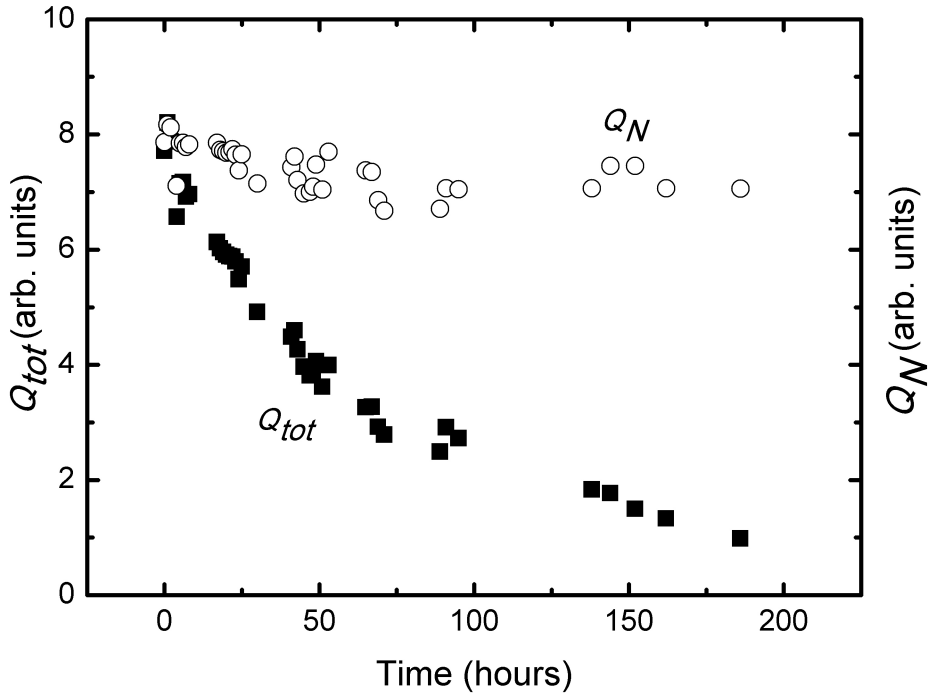

Fig. 2-4 The integrated area of the transient EL of unencapsulated device A1 operated constantly at 9V, Q_{tot}, (solid squares) and the normalized value, Q_N, (open circles) vs.

the OLED's operation time.

In spite of the decline of Q_{tot} caused by degradation of the OLED, both the profile of the transient EL and Q_N were barely changed. It indicates that the EL spikes and tails are an intrinsic property of the SMOLEDs that is related to the EML guest-host system, device materials and structure, and carrier injection and transport energy barriers; it is not affected by early-stage ambient (likely humidity)-induced degradation mechanisms.

2.3.1-4 Effects of Pulse Width

Fig. 2-5 shows the dependence of the on-pulse EL and EL spike intensity on the applied bias pulse width (PW) for an A2 device.

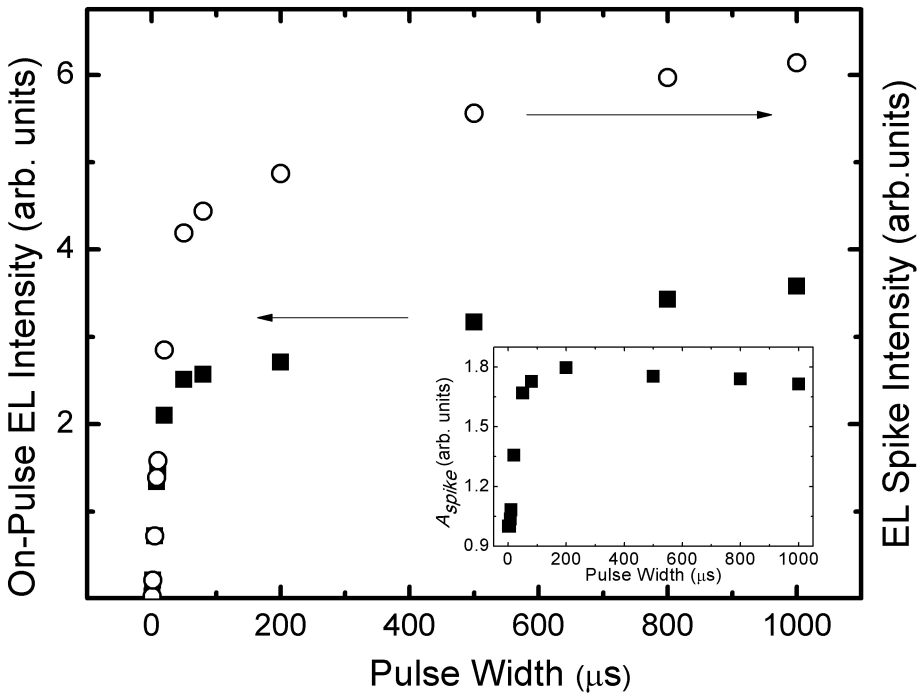

Fig. 5. The pulse width dependence of the on-pulse EL (solid squares) and EL spike (open circles) intensities of device A2. Inset: Dependence of the EL spike intensity normalized to the on-pulse intensity of A2 on the bias pulse width.

No spikes are observed when the PW is below 5 μs. The spike intensity increases

sharply as the PW increases, but beyond 100 μs it saturates. When the PW increases, the bulk HTL and ETL carrier densities, in addition to the CCP density, increase, resulting in stronger electric field-induced EL quenching, which increases the difference between the EL spike intensity and the on-pulse EL. This behavior is in contrast to that of undoped and [2-methyl-6-[2-~(2,3,6,7-tetrahydro-1H, 5H-benzo [ij] quinolizin-9-yl)- ethenyl]-4H-pyran-4- ylidene] propane-dinitrile (DCM2)-doped DPVBi OLEDs[16,17], where the normalized spike amplitude decreases beyond a PW of ~100 μs, clearly due to the subtle differences between the EL overshoot mechanisms in the Alq_3 and DPVBi-based devices. In the latter devices, there is a (modest) spike in the undoped OLEDs as well, and DCM2 traps both h^+ and e^- [17]. In the wide variety of the OLEDs described in this current study, when the PW is long enough for the device to reach a steady state, the relative spike intensity saturates due to the unchanged charge profile within the OLED.

2.3.2. Model Analysis

Based on the experiments described in the previous section and our interpretation of the origin of the EL spikes and tails, a model, accounting for the observations, was developed. As a brief summary, the major processes taken into account following the bias pulse in fluorescent guest-host systems include

(*i*) EL decay of SEs formed during the pulse;

(*ii*) exciton formation from carriers injected into the RZ during the falling edge of the voltage pulse (i.e., during the 0 - 50 ns period following the pulse);

(*iii*) recombination of initial CCPs (those present at t ~ 50 ns);

(*iv*) recombination of newly formed CCPs generated from uncorrelated, detrapped carriers at $t > 50$ ns;

(*v*) decay of SEs formed from TTA.

In simulating the experimental results, the decay of the pre-existing SEs can be neglected, since their lifetime is < 10 ns [11,23]. Process (*v*) was not considered because its contribution is a significant component of the EL tail only at times beyond those monitored in this study [14,15]. Therefore, the EL spikes and tails were simulated as an exponential decay of SEs formed in processes (*ii*) - (*iv*).

The net SE formation rate $dN_{SE}(t)/dt$ is given by [22]

$$\frac{dN_{SE}(t)}{dt} = \left(\frac{dN_{exc}}{dt}\right)_J + N_{ccp0}R_{ccp}(t) + \int_0^t \frac{dN_t(t')}{dt'} R_{ccp}(t-t')dt' - \frac{N_{SE}(t)}{\tau_{SE}} \tag{2.1}$$

The first term of Eq. (2.1) describes process (*ii*) in which the injected carriers' profile during the falling edge of the bias is proportional to the injection-limited current density J [5,7]:

$$\left(\frac{dN_{exc}}{dt}\right)_J \propto J \propto V(t)^2 \exp\left(-b/V(t)\right) \tag{2.2}$$

The second term in Eq. (2.1) describes process (*iii*). In the initial CCPs (with initial density N_{ccp0}), subject to Coulomb attraction, the untrapped carrier performs a random walk toward the trapped carrier (usually localized on the guest). The recombination rate of these CCPs can be written as [20]:

$$R_{ccp}(t) = \frac{\sqrt{4\pi}}{\sqrt{D_{ccp}}} \frac{r_c}{t^{3/2}} \int_0^\infty g(r_0) \exp\left(-\frac{r_0^2}{4D_{ccp}t}\right) \exp\left(-\frac{r_c}{r_0}\left(1 - \operatorname{erf}\left(\frac{r_0}{\sqrt{4D_{ccp}t}}\right)\right)\right) r_0^2 \, dr_0 \tag{2.3}$$

where

$$g(r_0) = \frac{\exp\left(-\frac{(r_0 - \bar{r})^2}{\sigma^2}\right)}{4\pi^{3/2}\sigma\bar{r}^2} \tag{2.4}$$

is a standard Gaussian distribution. In Eqs. (2.3) & (2.4) D_{ccp} is the diffusivity of the mobile charge within the CCP, $r_c \sim 19$ nm is the room temperature Onsager radius [17], r_0 is the e^--h^+ separation within the CCP, $\bar{r}$ is the average of r_0, and σ is the r_0 distribution width.

The third term in Eq. (2.1) is attributed to the recombination of detrapped charges. Due to the broad distribution of trap levels in organic materials [31], the total density of trapped charges is approximated by a stretched exponential [32,33], which is often used to describe charge transport and trapping governed by a distribution of relaxation times, in disordered systems

$$N_t(t) = N_t(0)\exp\left(-(t/\tau_{ucc})^{\beta}\right) \tag{2.5}$$

β is the stretching factor that quantifies the distribution width of the trapping energies, and τ_{ucc} is the characteristic time the carrier remains uncorrelated.

The fourth term in Eq. (2.1) presents the loss of SEs due to the radiative and various nonradiative decay channels.

By solving Eq. (2.1), the time-dependent $N_{SE}(t)$ can be expressed as [22]:

$$\begin{aligned} N_{SE}(t) = {} & N_e exp\left(-\frac{t}{\tau_{SE}}\right) + N_{ccp0}\, exp\left(-\frac{t}{\tau_{SE}}\right)\int_0^t R_{ccp}(t')\, exp\left(\frac{t'}{\tau_{SE}}\right)dt' \\ & + exp\left(-\frac{t}{\tau_{SE}}\right)\int_0^t exp\left(\frac{t'}{\tau_{SE}}\right)\left[\int_0^{t'}\frac{dN_t(s)}{ds}R_{ccp}(t' \right. \\ & \left. - s)ds\right]dt' \end{aligned} \tag{2.6}$$

where $N_e = \int_0^t \left(\frac{dN_{exc}}{dt}\right)_J exp\left(\frac{t'}{\tau_{SE}}\right) dt' + Constant$. The first, second, and third terms of Eq. 6 are due to excitons generated from process (*ii*), (*iii*) and (*iv*), respectively. In the second and third terms the $t = 0$ lower limit of the integrals corresponds to $t = 50$ ns in the experiments. Due to the fast decay of the SEs and the recombination of CCPs compared to the detrapping rate, the third term of Eq. (2.6) can be approximated by the stretched exponential (Eq. (2.5)).

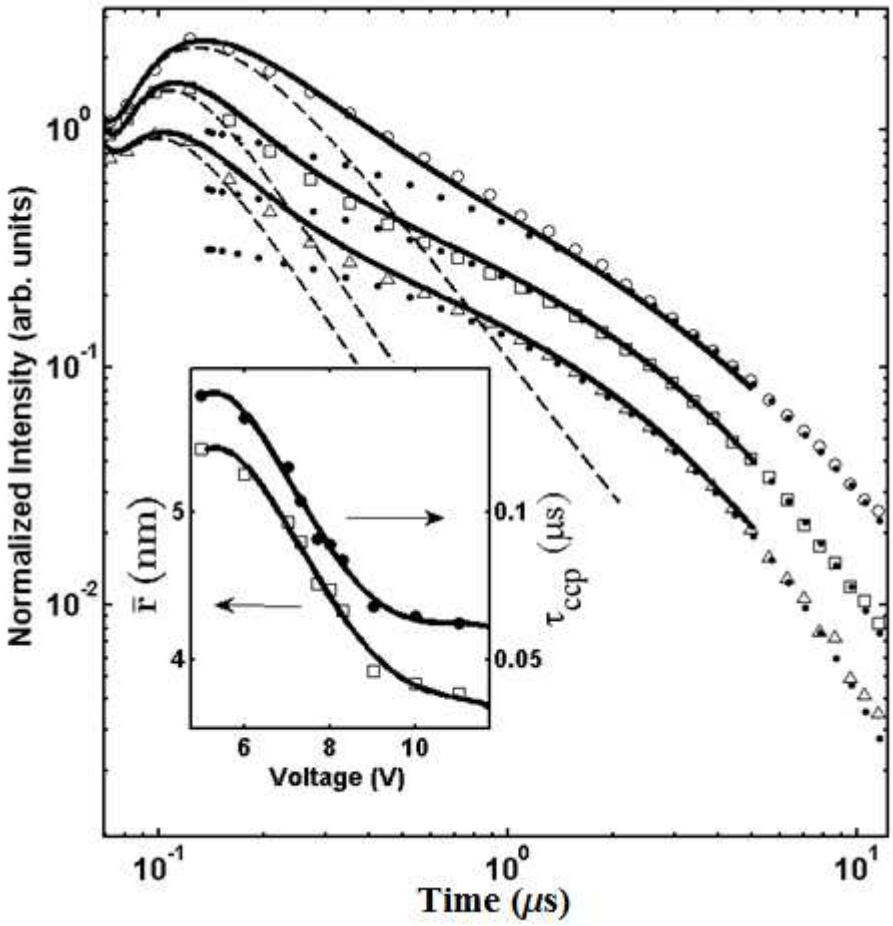

Fig. 2-6 Log-log plot of the transient EL of device A2 following 7 V (circles), 9 V (squares), and 11 V (triangles) pulses. The solid lines are the best fits using Eq. (6). The dashed and dotted lines are the contributions of the excitons and CCPs present at $t = 50$ ns, and detrapped carriers (governed by a stretched exponential), respectively. Inset: the voltage dependence of τ_{ccp} and $\bar{r}$; the lines are guides to the eye.

Fig. 2-6 shows the log-log plot of the normalized transient EL profile for device

A2 after a 100 μs bias pulse with on-pulse amplitudes of 7, 9, and 11 V. The solid lines show the best fit using Eq. (2.6). The separate contributions of processes (*ii*) + (*iii*) and process (*iv*) (governed by the stretched exponential dynamics) are plotted as the dashed and dotted lines, respectively. As clearly seen, the model is in good agreement with the observed behavior *over the whole observed transient EL period*. In particular, the agreement is better than that obtained using a CCP + Langevin recombination model described previously [17].

Fitting Eq. (2.6) to the observed behavior yields the SE decay time τ_{SE} = 8.7 ns, which is consistent with the C6 radiative lifetime τ_{rad} < 10 ns [12,23]. It also yields a practically unchanged $D_{ccp} \sim 5.6\times10^{-7}$ cm^2/s. This implies a mobility of ~ 2×10^{-5} cm^2/V·s, which is reasonable given the fact that the holes are trapped and the relative movement within the CCPs is dominated by the mobile electrons hopping among Alq_3 molecules [34].

The inset of Fig. 2-6 shows the dependence of $\bar{r}$ and τ_{ccp} on the bias. The fit yields $\bar{r}$ = 4.9, 3.9, and 3.7 nm and τ_{ccp} = 115, 68, 63 ns at 7, 9, and 11 V, respectively, where $\tau_{ccp} = \bar{r}^2/(4D_{ccp})$. The decrease in $\bar{r}$ is obviously due to the increased carrier density and consequently decreased τ_{ccp}, but both level off above ~9 V where $\bar{r} \approx 3.7$ nm.

At *t* < 200 ns, the first and second terms of Eq. (2.6) dominate. At longer times the free carrier density decreases, and the detrapping process increasingly dominates. The dotted lines in Fig. 6 represent the contribution of the detrapping process that, as mentioned, is governed by the stretched exponential behavior (Eq. (2.5)). The fitting

of the long tails and Eq. (2.5) yield $\bar{\tau}_{ucc} =$ 0.74, 0.86, and 1.05 μs for 7, 9, and 11 V, respectively, where $\bar{\tau}_{ucc} = (\tau_{ucc}/\beta)\Gamma(1/\beta)$, and Γ is the gamma function [35]. The respective values of β are 0.38, 0.48, and 0.59. The increase in β with V is expected, as the additional charges likely occupy a narrower range of energies in shallower tail states. The increase of $\bar{\tau}_{ucc}$ with V may be due to the increasing imbalance between the saturated h^+ trapping sites in the C6 guests and the increased density of e^- in the shallow host Alq_3 states.

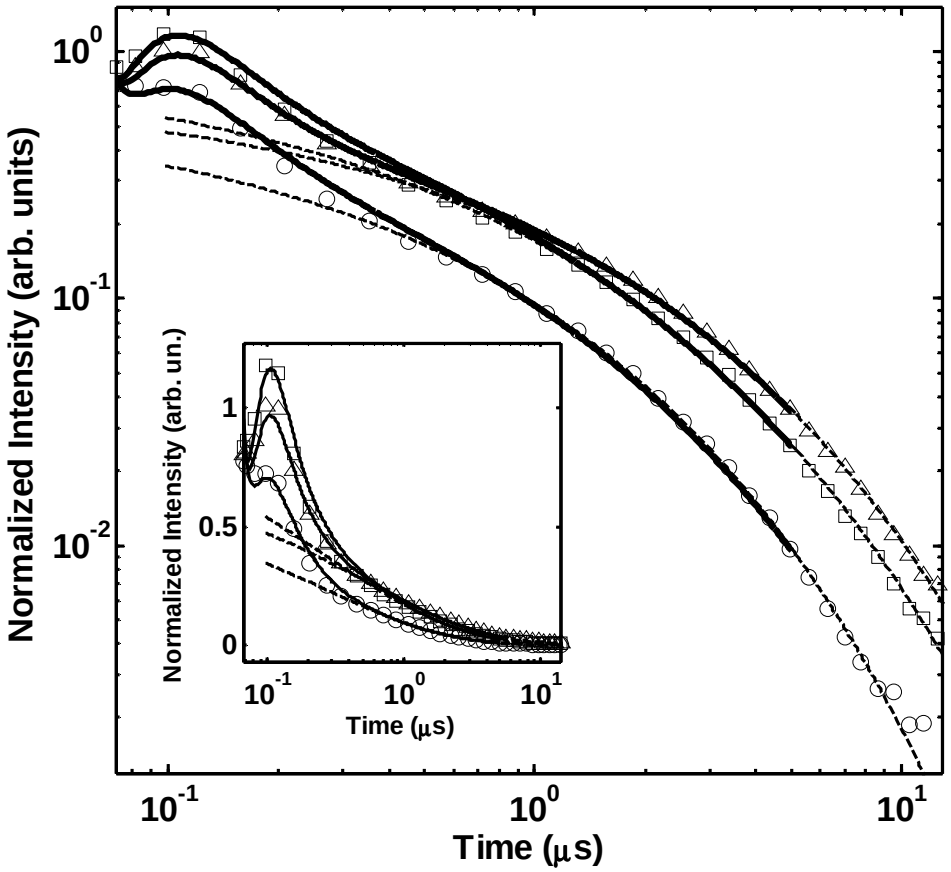

Fig. 2-7 The transient EL decay of A0 (circles), A2 (squares), and A5 (triangles) following a 10 V bias pulse with 100 μs duration. The solid lines are the least square fits of Eq. (6); the dashed lines are the fits of the stretched exponential (Eq. 5). The inset is the semi-log plot expansion showing the spikes.

Fig. 2-7 shows the fit of the model to the transient EL in OLEDs with different doped layer thickness following a 10 V bias pulse. Note that the relative intensity of

the long tail at a given *V* increases with increasing thickness of the doped layer *x*, indicating that most of the tail emission is due to C6. The fit of Eq. (2.5) to the long tails yields $\bar{\tau}_{ucc}$ = 0.57, 0.92, and 1.01 μs for A0, A2, and A5, respectively, at *V* = 10 V. This increase in $\bar{\tau}_{ucc}$ with doped layer thickness is probably due to the longer time needed for the detrapped carriers to find the opposite charges and form an exciton.

2.3.3. Effect of the HIL and ETL/HBL in C6-doped Alq_3-based devices

The observation of EL spike with an amplitude greater than the on-pulse level is intriguing and elucidating their nature is therefore challenging. In order to further evaluate the above-mentioned model and elucidate the origin of the spikes, additional C6-doped Alq_3-based devices with different materials/structures were fabricated; their transient EL behavior is shown in Fig. 8. In particular, the influence of the HIL and ETL/HBL on the EL spikes was investigated. The structures are (a) a device without any HIL; (b) a control device A1 with CuPc as the HIL; (c) a device with CuPc as the HIL and an added ETL/HBL of 4,7-diphenyl-1,10- phenanthroline (BPhen), where the total thickness of the device is kept constant; (d) a device with MoO_3 as the HIL, with no added BPhen.

As seen in Fig. 2-8, the normalized A_{spike} decreased from structure (a) to (b) to (c). No EL spikes were observed in device (d) or in a device with both MoO_3 and BPhen (not shown). BPhen is a well known ETL/HBL material [36], while MoO_3 greatly improves hole injection [37,38]. In comparing the devices shown in Fig. 2-8(a) (no HIL), (b) (CuPc as HIL) and (d) (MoO_3 as HIL), the EL spike decreases and even

disappears as the h^+ injecting energy barrier is lowered. In comparing devices (b) (no ETL/HBL) and (c) (BPhen added) of Fig. 2-8, the EL spikes are reduced as the BPhen is added. Based on these observations, we conclude that in addition to a sufficient trapped carrier density in the RZ (as discussed in section 2.1) a sufficiently high h^+ injection barrier and the absence of a ETL/HBL are also crucial for creating strong transient EL spikes.

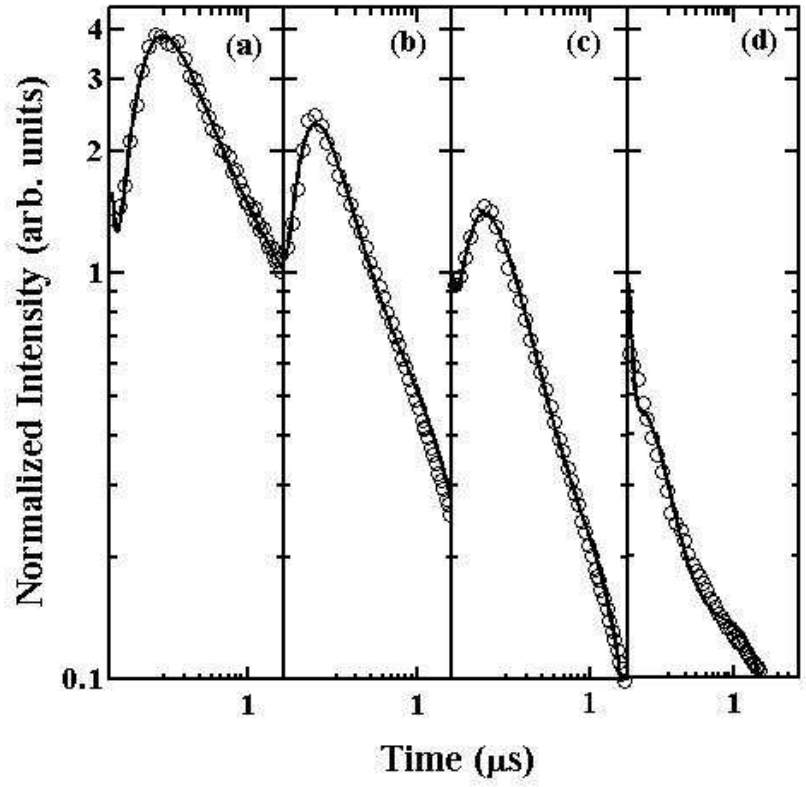

Fig. 2-8 The transient EL following a 100 μs bias pulse for four devices with different structures, normalized to the on-pulse level. (a) ITO/50 nm α-NPB/2 nm 1wt% C6 doped-Alq_3/38 nm Alq_3/1 nm LiF/~120 nm Al, i.e, no HIL; (b) ITO/5 nm CuPc/50 nm α-NPB/2 nm 1wt% C6 doped-Alq_3/38 nm Alq_3/1 nm LiF/~120 nm Al, i.e., CuPc as the HIL; (c) ITO/5 nm CuPc/50 nm α-NPB/2 nm 1wt% C6 doped-Alq_3/38 nm Alq_3/30 nm BPhen/1nm LiF/~120nm Al, i.e., a BPhen HBL was added to structure (b); (d) ITO/5 nm MoO_3/50 nm α-NPB/2 nm 1wt% C6 doped-Alq_3/38 nm Alq_3/1 nm LiF/~120 nm Al, i.e., structure (b) where MoO_3 replaced CuPc as the HIL. The lines are the simulations based on Eq. 2.6.

The foregoing results suggest that the mechanism that is likely responsible for EL

spikes whose amplitude exceeds the on-pulse intensity is reduced electric field-induced dissociative SE quenching [29]. The high barrier for h^+ injection in devices with CuPc or no HIL results in a large accumulation of h^+ at the ITO/α-NPB or ITO/CuPc interface, respectively, when biased. This high h^+ density increases the internal field, which dissociatively quenches SEs during the bias pulse. When the bias is turned off, this h^+ accumulation layer dissipates as the h^+ diffuse, mostly back to the anode, resulting in much less field-induced SE dissociative quenching. When MoO_3 is used as the HIL, h^+ injection is greatly improved. This improvement increases the carrier density within the bulk of the organic materials and forces the major accumulation of carriers to occur at the α-NPB/Alq_3 interface. In this way the internal electric field is higher and slower to decay, and consequently continues to suppress the EL after the bias is turned off, and therefore no spike is observed.

The observation that BPhen reduces the spike is probably due to the enhanced e^- mobility in that material (~50 times higher than in Alq_3 [36]), which probably reduces h^+ buildup at the α-NPB/Alq_3 interface and in the RZ.

An alternative mechanism, namely increased fraction of h^+ that have leaked through the RZ, drift toward the cathode, and then "turn back" toward the RZ, is ruled out as a major contributor to the spikes. This is due to at least two observations: (a) The RT spike is absent from the undoped devices; a significant contribution from h^+ beyond the RZ that turn back toward it would mandate a significant spike in the undoped devices as well. (b) As mentioned in Sec. 2.1, the contribution of h^+ that turn back toward the RZ after having drifted beyond it to the spikes should, if anything,

increase with *y*, in sharp contrast to the observed strong decrease in A_{spike} with increasing *y* (Fig. 2-3).

2.3.4. Effect of Post-Pulse Reverse Bias

Fig. 2-9 shows the transient EL behavior of device A1 under post-pulse reverse and forward bias.

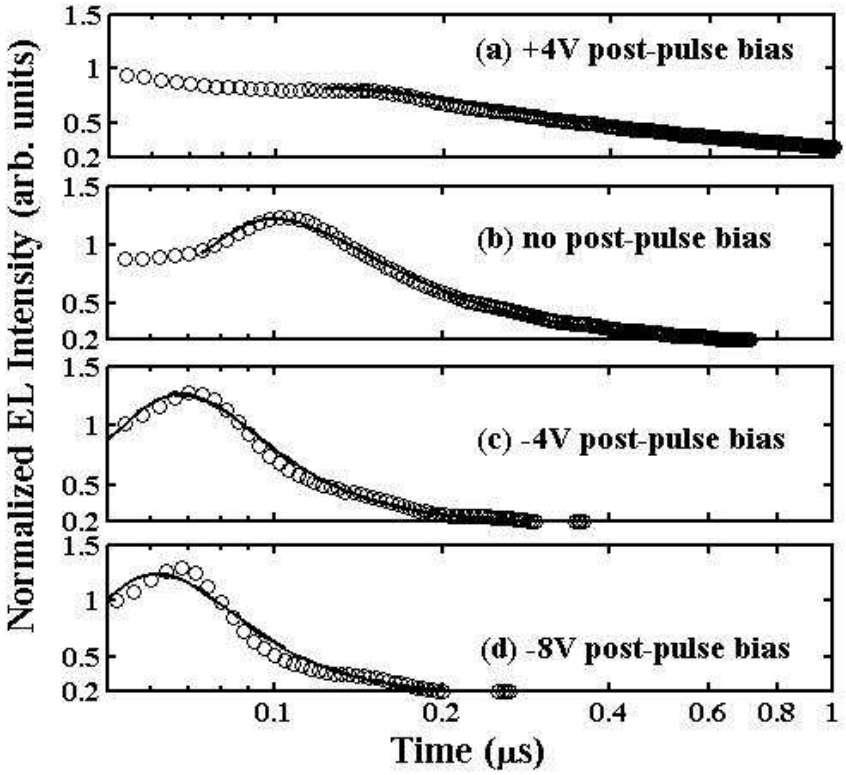

Fig. 2-9 The normalized transient EL data (symbols) and simulations (lines) with 100 μs, 9 V bias pulses at post-pulse voltages of 4 V (a), 0 V (b), -4 V (c), and -8V (d).

When a forward bias is applied, the post-pulse internal electric field is slower to decay as more charges continue to be injected into the RZ, which results in suppression of the EL spike and a much higher emission tail. Under reverse bias, the decay of the internal electric field becomes faster and the spike appears earlier with a weakened tail. This behavior strongly supports the conclusion that the transient EL tail results from trapped charges rather than TTA because, as mentioned, neutral

triplets should not be affected by the external field.

2.3.5. Effect of Temperature

Fig. 2-10 shows the dependence of the EL spikes on the temperature in the 40 to 300 K range.

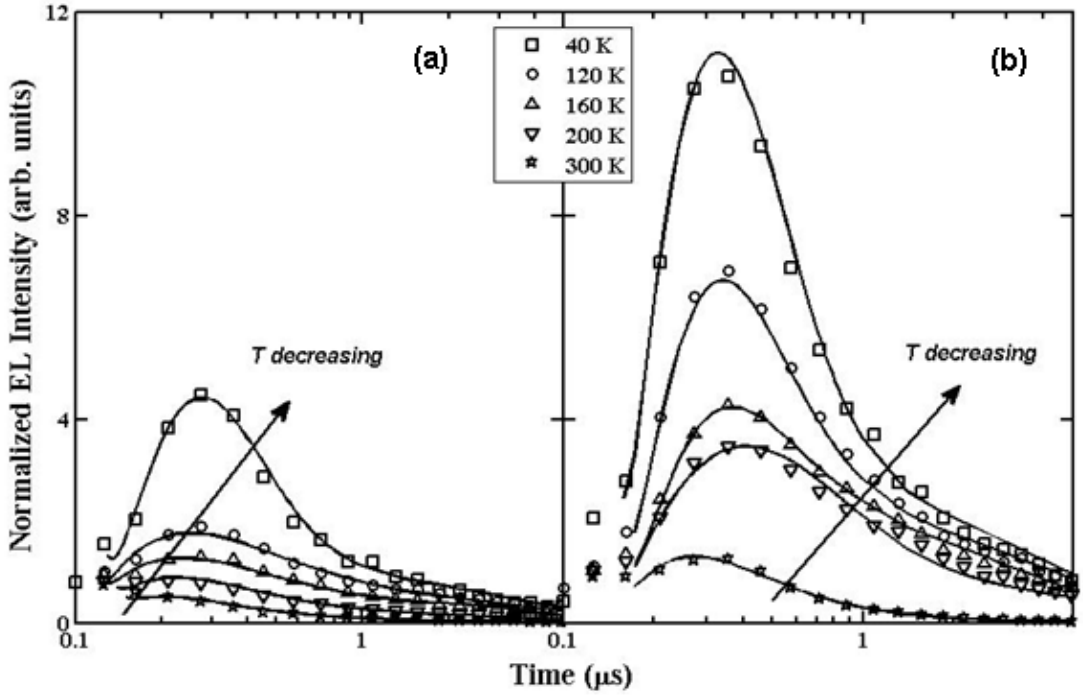

Fig. 2-10 The experimental, normalized EL (symbols) and simulated EL (lines) of devices A0 (a) and A1 (b) at temperatures $40 \leq T \leq 300$ K. The applied bias PW was 1 ms to achieve a high enough EL intensity with the low temperature measurements set-up.

A 1 ms pulse was used to achieve a sufficiently high EL intensity in the low-temperature measurements. As shown in the inset of Fig.5, the pulse width difference (between 100 μs and 1 ms) does not affect the transient behavior. Both A0 and A1 exhibit strong EL spikes at low temperatures, while only A1 shows an EL spike at room temperature [39]. At low temperatures, carriers are more prone to trapping in shallow traps as well. Their reduced mobility then suggests a much higher charge density within the RZ after the end of the pulse. This should lead to a higher concentration of CCPs and a strong internal electric field during the pulse that

quenches the EL, yielding a larger difference between the transient and on-pulse EL; Fig. 2-10 supports this interpretation.

2.3.6. Transient EL in Other SMOLEDs

The transient EL behavior was studied in other efficient SMOLEDs of different materials. These include rubrene-doped Alq_3, *fac* tris(2-phenylpyridine) Ir ($Ir(ppy)_3$)-doped spiro-4,4'-Bis(9-carbazolyl) biphenyl (spiro-CBP), and Pt(II) octaethylporphine (PtOEP)-doped Alq_3 SMOLEDs. The observations confirm the occurrence of EL spikes and tails in various guest-host SMOLEDs where charge trapping is dominant and prove that the phenomenon appears to be universal even in some phosphorescent OLEDs where triplet excitons are the emitting species.

Fig. 2-11 exhibits the transient EL behavior of devices with a rubrene-doped Alq_3, $Ir(ppy)_3$-doped spiro-CBP, and PtOEP-doped Alq_3 EML. As seen in the figure, EL spikes are observed in the first two, but not in the PtOEP-doped device, even at 20 K. This situation can be attributed to two phenomena: the emission of PtOEP-doped Alq_3 guest-host system is dominated by strong energy transfer [40], and the long radiative decay time of this phosphorescent molecule is $\tau_{rad} \sim 100$ μs. In contrast, the emission mechanisms of the $Ir(ppy)_3$- and rubrene-doped devices are both known to originate from charge trapping [40,41]. Note that the spikes in the rubrene-doped devices are stronger than those in the C6- and $Ir(ppy)_3$-doped SMOLEDs. This behavior supports the CCP model since it is well known that rubrene is a stronger h^+ trap in Alq_3. Hence, the EL spikes appear to be a reliable and easily measurable phenomenon to identify the main emitting mechanism in guest-host OLEDs.

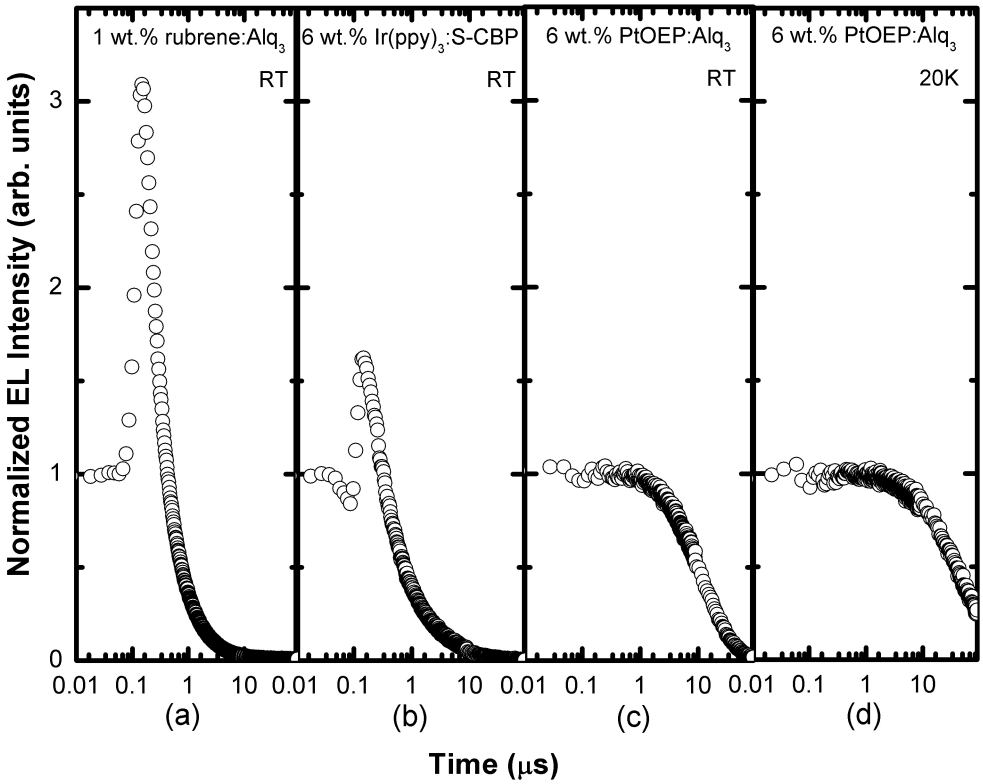

Fig. 2-11 The transient EL of different guest-host SMOLEDs, all with structure ITO / 5 nm CuPc / 50 nm α-NPB / guest-host EML / 40 nm Alq_3 / 1 nm LiF / ~120 nm Al. EML is (a) 1 nm 1 wt.% rubrene in Alq_3, at RT, 8 V, 100 μs pulse, (b) 1 nm 6 wt% $Ir(ppy)_3$ doped-spiro CBP, at RT, 8 V, 100 μs pulse, (c) & (d) 1 nm and 2 nm 6 wt.% PtOEP doped-Alq_3 with 600 nm long-pass filter at RT, 7 V, 100 μs pulse and 20 K, 24 V, 1 ms pulse, respectively.

2.4 Conclusions

In conclusion, following a bias pulse, ITO/CuPc/α-NPB/C6-doped Alq /Alq_3/LiF/ Al devices and other charge trapping guest-host SMOLEDs exhibit EL spikes at 70 – 300 ns and μs long EL tails, whose amplitude varies with the pulse voltage. The spikes are not affected by early-stage device degradation, but are strongly influenced by the pulse duration and the distance of the doped layer from the HTL. They narrow and shift to shorter times under a reverse bias applied after the pulse. At low temperature they are much stronger, appear after a slightly longer time, *and are apparently universal in all charge-trapping SMOLEDs*, with the exception of devices

in which there is efficient energy transfer to a long-lived phosphorescent guest emitter. Good agreement is found between the experimental data and a model based on recombination of CCPs and charges that are initially unpaired. The generation of spikes exceeding the on-pulse EL level is attributed to the combination of CCP formation and reduced electric field-induced SE dissociation after the pulse. The spikes are significantly weaker in devices where a BPhen ETL/HBL layer is added, likely due to enhanced e^- transport, and absent in devices where MoO_3 replaces CuPc.

The comparison of the transient EL behavior of various SMOLEDs suggests that the EL spikes are an additional reliable tool to identify the main emitting mechanism in guest-host OLEDs.

Acknowledgements

Ames Laboratory is operated by Iowa State University for the US Department of Energy (USDOE) under Contract No. DE-AC 02-07CH11358. This work was supported by the Director for Energy Research, Office of Basic Energy Sciences, USDOE.

References

1. C. W. Tang and S. A. Vanslyke, Appl. Phys. Lett. **51**, 913 (1987)
2. R. F. Service, Science **310**, 1762 (2005)
3. J. Shinar and R. Shinar, J. Phys. D **41**, 133001 (2008).
4. *Organic Electronics in Sensors and Biotechnology* (Eds: R. Shinar and J. Shinar, McGraw Hill, NY, 2009).

5. J. Shinar and V. Savvate'ev, in *Organic Light Emitting Devices: A Survey* (Ed: J. Shinar, Springer Verlag, NY, 2004), Ch. 1.
6. *Organic Electroluminescence* (Ed: Z. Kafafi, Taylor & Francis, CRC Press, Boca Raton, FL 2005).
7. J. Kalinowski, *Organic Light-Emitting Diodes: Principles, Characteristics, and Processes* (Marcel Dekker, NY, 2005).
8. Y. H. Tak, J. Pommerehne, H. Vestweber, R. Sander, and H. Bässler, Appl. Phys. Lett. **69**, 1291 (1996).
9. V. R. Nikitenko, V. I. Arkhipov, Y.-H. Tak, J. Pommerehne, H. Bässler, and H.-H. Hörhold, J. Appl. Phys. **81**, 7514 (1997).
10. J. M. Lupton, V. R. Nikitenko, I. D. W. Samuel, and H. Bässler, J. Appl. Phys. **89**, 311(2001).
11. D. J. Pinner, R. H. Friend, and N. Tessler, J. Appl. Phys. **86**, 5116 (1999).
12. J. Kalinowski, N. Camaioni, P. Di Marco, V. Fattori, and A. Martelli, Appl. Phys. Lett. **72**, 513 (1998).
13. M. A. Baldo, C. Adachi, and S. R. Forrest, Phys. Rev. B **62**, 10967 (2000)
14. Z. D. Popovic and H. Aziz, J. Appl. Phys. **98**, 013510 (2005).
15. D. Y. Kondakov, J. Appl. Phys. **102**, 114504 (2007).
16. V. Savvateev, J. H. Friedl, L. Zou, J. Shinar, K. Christensen, W. Oldham, L. J. Rothberg, Z. Chen-Esterlit, and R. Kopelman, Appl. Phys. Lett. **76**, 1501(2000).
17. K. O. Cheon and J. Shinar, Phys. Rev. B **69**, 201306 (2004).
18. S. C. Tse, H. H. Fong, and S. K. So, J. Appl. Phys. **94**, 2033 (2003).

19. A. Kadashchuk, V. I. Arkhipov, C.-H. Kim, J. Shinar, D.-W. Lee, Y.-R. Hong, J.-I. Jin, P. Heremans, and H. Bässler, Phys. Rev. B **76**, 235205 (2007).

20. A. Mozumder, J. Chem. Phys. **48**, 1659 (1968).

21. L. Zou, V. Savvate'ev, J. Booher, C.-H. Kim, and J. Shinar, Appl. Phys. Lett. **79**, 2282 (2001).

22. Z. Gan, R. Liu, R. Shinar, and J. Shinar, Appl. Phys. Lett. **97**, 113301 (2010).

23. T. Nakazawa, M. Asano, S. Fujita, and S. Fujita, Jpn. J. Appl. Phys., Part 2 **38**, L206 (1999).

24. (i) The pulsed bias was provided by an Avtech Model AV-1011 Pulse Generator, with bias rise and fall times of ~10 ns. (ii) The field-dependent electron mobility in Alq_3 and hole mobility in α-NPB are ~10^{-4} cm^2/Vs, so if the potential drop across each of these layers is ~4 V, then the time required to drift through the ~45 nm-thick HTL & ETL is ~$(45\times10^{-7}cm)^2/(4V\times10^{-4}\ cm^2/Vs)$ = 50 ns.

25. J. Kido and Y. Iizumi, Appl. Phys. Lett. **73**, 2721 (1998).

26. J. Huang, J. Blochwitz-Nimoth, M. Pfeiffer and K. Leo, J. Appl. Phys. **93**, 838 (2003).

27. E. Tutiš, D. Berner, and L. Zuppiroli, J. Appl. Phys. **93**, 4594 (2003).

28. B. Masenelli, E. Tutis, M. N. Bussac, and L. Zuppiroli, Syn. Met. **121**, 1513 (2001).

29. R. Kersting, U. Lemmer, M. Deussen, H. J. Bakker, R. F. Mahrt, H. Kurz, V. I. Arkhipov, H. Bässler, and E. O. Göbel, Phys. Rev. Lett. **73**, 1440 (1994).

30. Y. Luo, H. Aziz, Z. D. Popovic and G. Xu, Appl. Phys. Lett. **89**, 103505 (2006).

31. S. Karg, J. Steiger, and H. von Seggern, Synth. Met. **111-112**, 277 (2000).

32. J. Kakalios, R. A. Street, and W. B. Jackson, Phys. Rev. Lett. **59**, 1037 (1987).

33. D. L. Huber, Phys. Rev. E. **53**, 6544 (1996).

34. H. Park, D. S. Shin, H. S. Yu, and H. B. Chae, Appl. Phys. Lett. **90**, 202103 (2007).

35. C. P. Lindsey and G. D. Patterson, J. Chem. Phys. **73**, 3348 (1980).

36. S. Naka, H. Okada, H. Onnagawa, and T. Tsutsui, Appl. Phys. Lett. **76**, 197 (2000).

37. H. You, Y. Dai, Z. Zhang, and D. Ma, J. Appl. Phys. **101**, 026105 (2007).

38. H. Lee, S. W. Cho, K. Han, P. E. Jeon, C. N. Whang, K. Jeong, K. Cho, and Y. Yi, Appl. Phys. Lett. **93**, 043308 (2008).

39. The spike's peak location can be affected by the time constant or delay time of the electronics. In the low- and room-temperature measurements the coaxial cables connecting the OLED to the electronics are ~4 and ~1.5 m long, so the spikes peak at 200–300 and 100 – 200 ns, respectively.

40. M. A. Baldo and S. R. Forrest, Phys. Rev. B **62**, 10958 (2000).

41. H. Murata, C. D. Merritt and Z. H. Kafafi, IEEE Journal of Selected Topics in Quantum Electronics **4**, 119 (1998).

Chapter 3. MoO_3 as Combined Hole Injection Layer and Tapered Spacer in Combinatorial Multicolor Microcavity OLEDs

Modified from **R. Liu**, C. Xu, R. Biswas, J. Shinar, R. Shinar,

Appl. Phys. Lett. **99**, 093305 (2011).

Abstract

Multicolor microcavity (μC) organic light-emitting diode (OLED) arrays were fabricated simply by controlling the hole injection and spacer MoO_3 layer thickness. The normal emission was tunable from ~490 to 640 nm and can be further expanded. A compact, integrated spectrometer with two-dimensional combinatorial arrays of μC OLEDs was realized. Introducing MoO_3 yields more efficient and stable devices, and reduces device breakdown. The pixel current density reaches ~4 A/cm^2, resulting in a maximal normal brightness $L_{\perp max}$ ~ 140,000 Cd/m^2, which is important for photoluminescence-based sensing and absorption measurements. The results also illustrate a new breakdown mechanism in OLEDs.

3.1 Introduction

Organic light-emitting diodes (OLEDs) have been widely studied over the last decade for applications in flat panel displays and solid-state lighting. Particularly, multi-color OLEDs are of great interest not only for simple fabrication of display sub-pixels, but also for their promise in miniaturized analytical devices. By combining OLEDs with multiple-wavelength emission on a simple substrate, they can either work as a compact spectrometer or form pixel arrays of excitation sources, with each pixel individually addressable, for bio(chemical) sensing of different analytes [1].

Previous studies have focused on tunable multi-color OLEDs within one pixel [2-7]. In spite of the fact that these devices, based on widening the recombination zone of multi-emitting layers or sophisticated materials and structures, are well integrated, they generally have broad emission spectra. In other studies, techniques with small controllable changes of the structures such as the doped-layer thickness variation [8], hybrid inkjet printing [9], optical color filter [10], and grayscale lithography [11] have been utilized to achieve pixel arrays with multi wavelength emission. However, with growing industrial requirements, to obtain a compact, potentially disposable analytical device, a simpler, economical method to fabricate multi-color OLEDs for the above-mentioned applications is desirable.

The hole injection layer (HIL) in OLEDs is necessary for favorable band alignment between the anode and the organic hole transport layer (HTL). Among the materials utilized, oxides such as V_2O_5 [12], WO_3 [13], and MoO_3 [12, 14 -19] have drawn interest due to their superior device performance. MoO_3, in particular, is widely used due to its ease of processing (it can be evaporated at a relatively low temperature). Considered as an insulating HIL, the optimized thickness of stoichiometric MoO_3 was found to be <1 nm [16].However, some studies have shown that the thermally-evaporated MoO_3 tends to be oxygen deficient, i.e., MoO_x ($x < 3$) [12,19]. Recent photoemission spectroscopy measurements further indicate high conductivity and favorable energy alignment in this suboxide [18,19]. With its relatively high refractive index [20,21], MoO_x can be used as a good injection and spacer material for tuning the optical length of μC OLEDs, while maintaining a

favorable current density-voltage (*J-V*) characteristic. Additionally, it is found that by applying this heat-resistant oxide as the HIL, the μC OLEDs show a more stable performance at high voltage and their maximum normal direction electroluminescence (EL) is enhanced. This is very beneficial for sensitive sensors, which require high excitation amplitudes.

It has been demonstrated that μC OLEDs fabricated between a total reflecting metal and a semi-transparent metal electrode [22,23] or dielectric mirror [24,25] result in narrow band-emissions concentrated in the normal direction. The OLEDs fabricated in such manner can emit at a number of sharp resonant cavity modes, determined by the cavity's optical length. In this sense, one can achieve multicolor μC OLEDs via simply step-changing the organic layer thickness during combinatorial fabrication. However, with the limited charge transport ability of organic materials, the μC OLEDs obtained in this way will have inferior electrical properties and luminosity. In this paper, we present a very simple alternative method for monolithic fabrication of multi-color μC OLED arrays by controlling the thickness of MoO_3, which serves as both the HIL and optical spacer. This provides a simple method to fabricate multicolor μC OLEDs without affecting significantly the electrical and optical properties of the devices.

3.2 Experiments and simulations

2×2 mm^2 pixels of μC OLEDs were fabricated. All depositions were performed in a thermal vacuum evaporation chamber (base pressure ~10^{-6} Torr; the organic layers' deposition rate was ~1 Å/s) installed in a glove box with <20 ppm O_2. For the

absorption spectrum demonstration, 15 mg/mL poly(3-hexyl thiophene) (P3HT) solution was spin-coated at 3000 rpm for 100 s on glass as the test sample. Twelve types of μC OLED pixel arrays (pixel diameter ~1.5 mm) were fabricated combinatorially on a 2"×2" substrate. The EL was monitored by a Hamamatsu R6060-02 photomultiplier tube (PMT) with a 50 Ω external load connected to a 350 MHz oscilloscope. The reference absorption spectrum was obtained by an Ocean Optics spectrometer using a tungsten lamp as the light source.

The rigorous simulations utilized a scattering matrix approach [27], where emissive dipoles were placed near the interface of the *N*,*N*'-bis(naphthalen-1-yl)-*N*,*N*'-bis (phenyl)benzidine (α-NPB) HTL and electron-transport and emissive tris(8-hydroxyquinoline) Al (Alq_3) layers. Then Maxwell's equations were solved for both polarizations, in Fourier space, i.e., in a plane wave basis, to obtain the emission from the OLED for different device geometries. In each layer of the OLED stack, the materials are represented by realistic frequency-dependent absorptive dielectric functions obtained from experimental measurements on Alq_3, α-NPB, Ag, Al, and MoO_3 [27-29].

3.3 Results and discussions

To prove that varying the thickness of the thermally-evaporated MoO_3 within a certain range can maintain comparable electrical properties of the device, α-NPB hole-only devices were fabricated on MoO_3 layers with different thickness (fabricated using the sliding-shutter technique [8]); their *J*-*V* curves are shown in Fig. 3-1 (a). These devices exhibit very weak EL (< 0.1 Cd/m^2), confirming that they are primarily

hole-only devices. The *J-V* curves of devices with 2, 5 and 10 nm of MoO_3 almost overlap each other (Fig. 3-1); the device with 20 nm MoO_3 shows a slightly lower current for the same voltages.

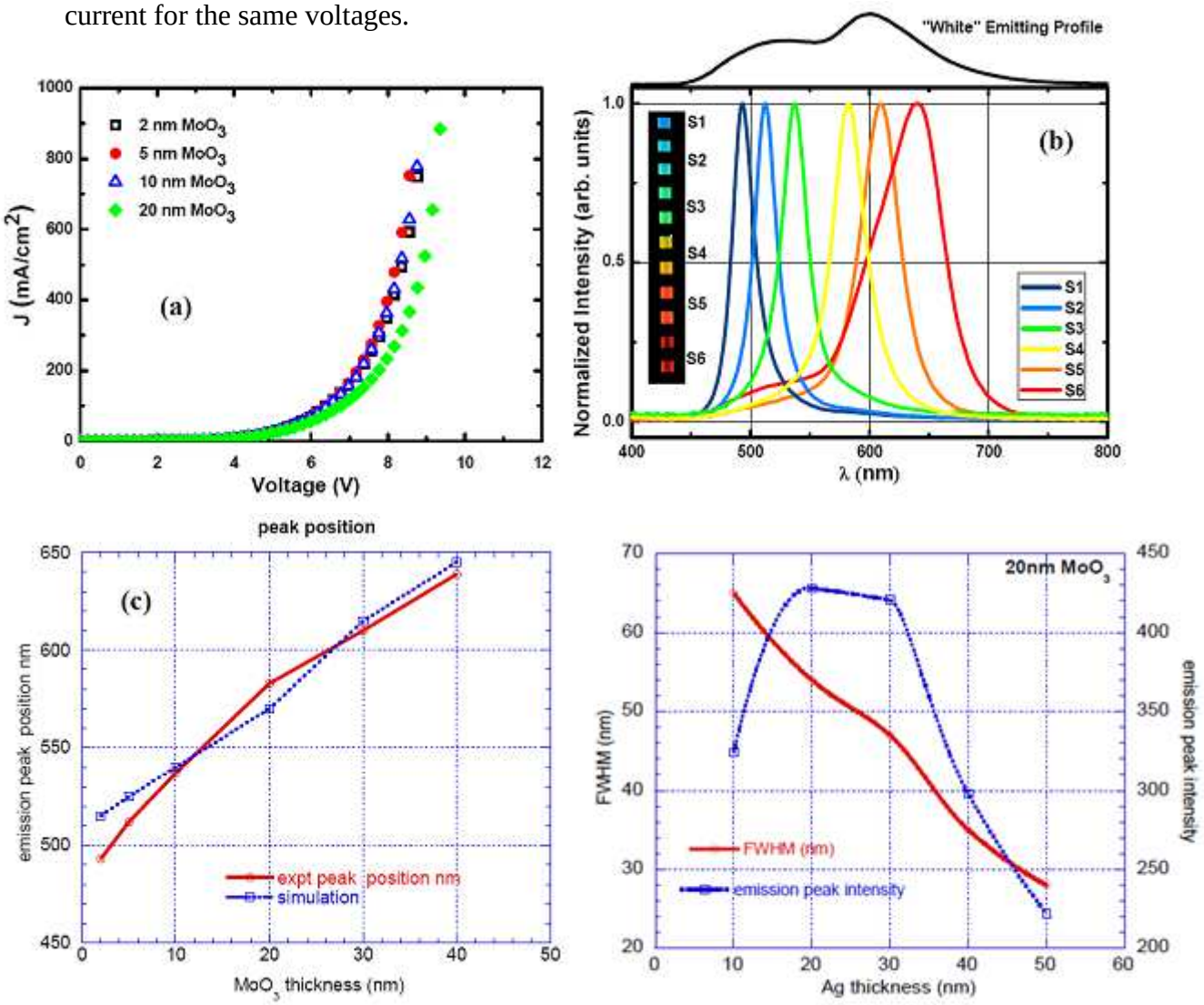

Fig. 3-1 (a) The J-V characteristics of the hole-only devices ITO/x nm MoO_3/112 nm α-NPB/100 nm Al, where x = 2, 5, 10, and 20 nm. (b) The photographs of the actual pixels and forward direction EL spectra of the multicolor μC OLEDs with the structure: 40 nm Ag/ y nm MoO_3/ 49 nm NPB/ 1 nm 8 wt% Ir $(MDQ)_2(acac)$:NPB/ 56 nm Alq_3/ 1nm LiF/ 100 nm Al, where y = 2, 5, 10, 20, 30 and 40 nm in S1, S2, S3, S4, S5 and S6, respectively, the black line is the EL spectrum of the reference OLED with the same active layer but ITO as the anode. All devices are driven at ~30 mA/cm^2; (c) Measured and simulated peak emission wavelength vs MoO_3 thickness. (d) Simulated peak emission intensity and full width at half maximum for the OLED emission as a function of the Ag anode thickness. Simulations are for a MoO3 thickness of 20 nm.

We then deposited MoO_3 with monotonically increasing thickness on top of Ag

using the same method as for the hole-only device. Organic layers with broad emission spectra were then inserted between the 40 nm Ag anode and the 100 nm Al cathode to form multicolor μC OLEDs. Photographs of the emissive pixels and the spectra in the normal direction are shown in Fig. 3-1(b) for OLEDs with various thicknesses of the MoO_3 spacer layers. The OLEDs consisted of 40 nm Ag / *x* nm MoO_3/ 49 nm α-NPB/ 1 nm 8 wt% Iridium (III) bis(2-methyldibenzo[f,h]quinoxaline) (acetylacetonate) ($Ir(MDQ)_2(acac)$): α-NPB/ 56 nm Alq_3/ 1nm LiF/ ~100 nm Al. The thin $Ir(MDQ)_2(acac)$ doped layer is responsible for the red emission peaking at ~610 nm and Alq_3 for the green emission peaking at ~525 nm. By changing the thickness of the MoO_3 we were able to tune the peak emission of the μC device from sky blue at 493 nm (device S1) to red at 639 nm (device S6). The smallest full-width at half maximum (FWHM) is ~22 nm for device S1 and it broadens for thicker MoO_3 layers; the efficiencies of the OLEDs are comparable. The broader emission at the longer wavelengths is probably due to the imperfect "white" emission of the active layer. Although higher efficiency can certainly be obtained with other materials and structures, the present results demonstrate the ability and simplicity of thermally-evaporated MoO_3 in realizing tunable efficient μC OLEDs.

It is worth noting that the sum of the optical lengths (L_{opt}) of the layers between the two metal electrodes is smaller than half the resonant wavelength $\lambda/2n$, where *n* is the layers' refractive index. This is due to electric field penetration into both the Ag and Al electrodes. Our simulations show that the penetration depth in Al is ~13 nm and in Ag it varies from 25 to 30 nm across the spectrum of interest. In considering

these penetration depths, the simulated peak positions (Fig. 3-1(c)) closely track the measured values across the entire MoO_3 thickness range.

The effect of the Ag cathode thickness is clearly critical. To achieve high normal direction efficiency, our simulations suggest that 20-30 nm is the optimal thickness (Fig. 3-1(d)), in agreement with earlier μC OLED studies [11,23] which showed that the optimized Ag thickness is ~25 nm. Thinner Ag increases the overall emission intensity due to less absorption but broadens the FWHM (Fig. 3-1(d)). Conversely, thicker Ag damps the overall intensity but provides sharper and more concentrated normal direction emission. The balance of the above-mentioned reasons results in the optimal Ag anode thickness. Our measurements (not shown) confirm that devices with 25 nm Ag are much more efficient than those with 40 nm Ag; however the latter do yield a purer color, i.e. a smaller FWHM

As mentioned, OLEDs have been utilized as excitation sources in (bio)chemical sensing. Hence, it is highly desirable that the OLEDs used in this application be operated at high emission intensity, while maintaining a reasonable operational lifetime. We emphasize that utilizing the MoO_x HIL not only yields wide tunability of the emission wavelength in the μC OLEDs, but also significantly improves the device stability and efficiency in comparison to other conventional HILs [14]. This situation is also confirmed in the μC devices with Ag as the electrode. As shown in Fig 3-2(a), starting from fixed EL amplitudes, the 90% lifetime of the device with MoO_x as the HIL is ~30× longer than that with CuPc. This is likely due to the reduction in the hole injection barrier (from the HIL to the α-NPB), so far fewer holes accumulate at the

HIL/HTL interface, resulting in much lower local Joule heating. In addition, MoO_3 is much more stable than other organic hole-injection materials, resulting in OLEDs with higher stability.

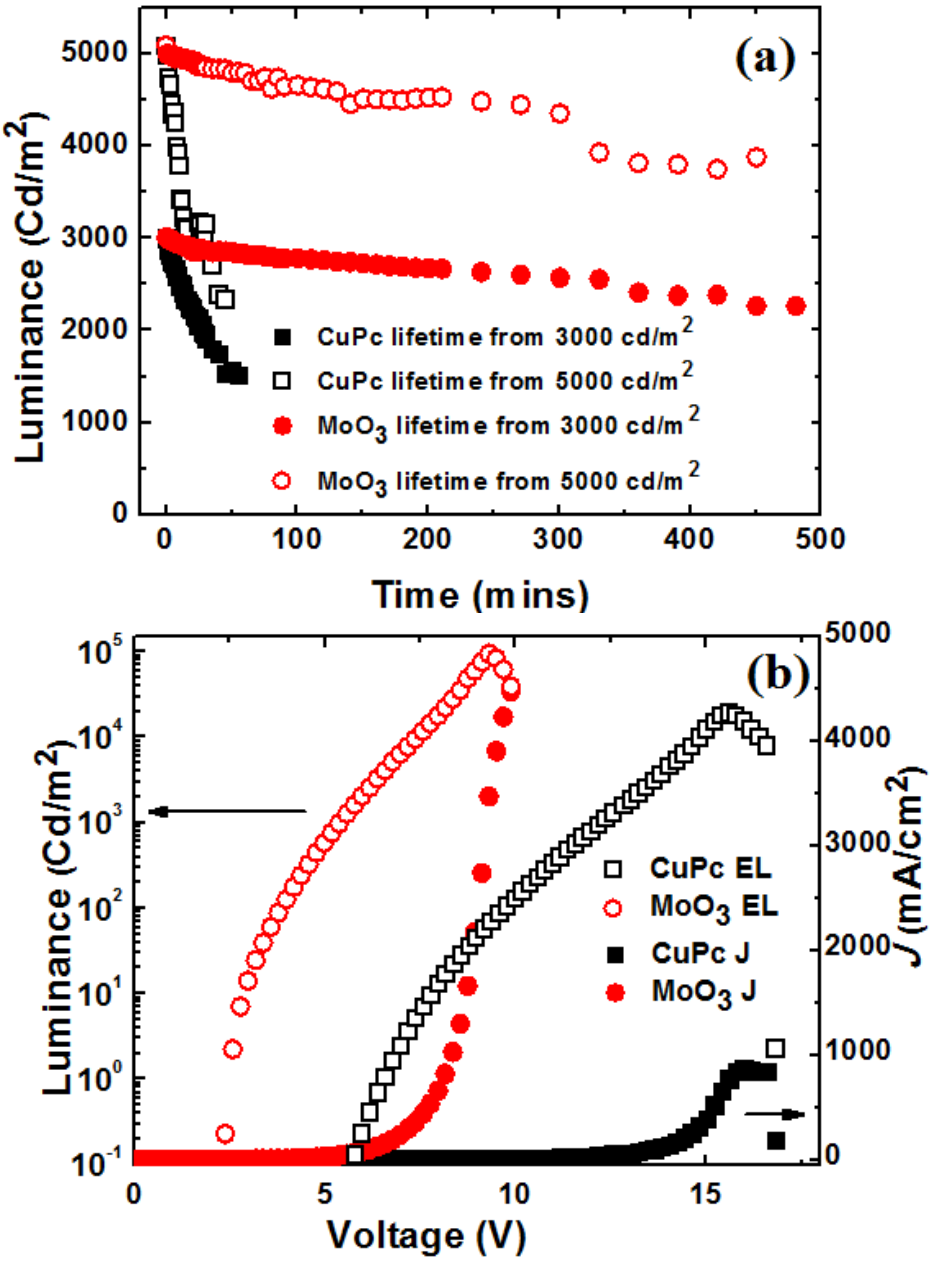

Fig. 3-2 (a) Comparison of the lifetime of μC OLEDs with MoO_x and CuPc as the HIL for EL intensities starting at 5000 & 3000 Cd/m^2. The OLED devices have the structure: 25 nm Ag/ 5 nm MoO_x/ 49 nm α-NPB/ 56 nm Alq_3/ 1nm LiF/ 100 nm Al and 25 nm Ag/ 5 nm CuPc/ 49 nm α-NPB/ 56 nm Alq_3/ 1nm LiF/ 100 nm Al; (b) *J-L-V* curves of the μC OLEDs with MoO_x or CuPc HILs.

The *J-L-V* curves of the Alq_3-based μC OLEDs fabricated with MoO_x and CuPc

are shown in Fig. 3-2(b). The advantage of MoO_x over CuPc is clearly observed in the far lower turn-on voltage – 2.4 V compared to 6.6 V at 1 Cd/m^2. Importantly, the μC OLEDs with MoO_x also yield a maximum normal direction EL that is higher than that of other conventional devices. As shown in Fig. 3-2(b), the μC OLED with CuPc breaks down at J < 1000 mA/cm^2, with a highest normal direction $L_{\perp max}$ ~ 20,000 Cd/m^2. The EL obtained with the MoO_x-based device at the same current density is similar ($L_{\perp max}$ ~ 22,000 Cd/m^2) because both devices utilize the same Alq_3 emitting material with the same intrinsic luminous efficiency, if charge balance effects are ignored. However, J of the MoO_x-based device could ramp up to ~4,000 mA/cm^2, resulting in $L_{\perp max}$ ~ 95,000 Cd/m^2, as shown in the figure, and even values of $L_{\perp max}$ ~ 140,000 Cd/m^2 were observed [30]. We propose that this may be due to two reasons: (i) MoO_x, compared to other conventional organic hole injection materials, can sustain higher local heating. (ii) Due to the favorable energy alignment, there is much less accumulation of interface charges that cause the local heating at the HIL/HTL junction. The comparison of these two devices provides evidence that the joule heating caused by charge accumulation at the HIL/HTL interface may be the major reason for the breakdown of the CuPc-based OLEDs.

To demonstrate the potential of multicolor OLEDs for on-chip applications, we fabricated an integrated spectrometer using these tunable μC OLEDs. As shown in Fig. 3-3(a), μC OLED arrays on glass were fabricated combinatorially to provide tunable peak emissions over a broad range of wavelengths. By making small changes in both the MoO_x and Alq_3 thickness, we were able to combine OLEDs with 12 different peak

emissions within a small substrate area. P3HT, a common donor material in organic photovoltaics, was spin-coated on a microscope slide; it served as a test sample.

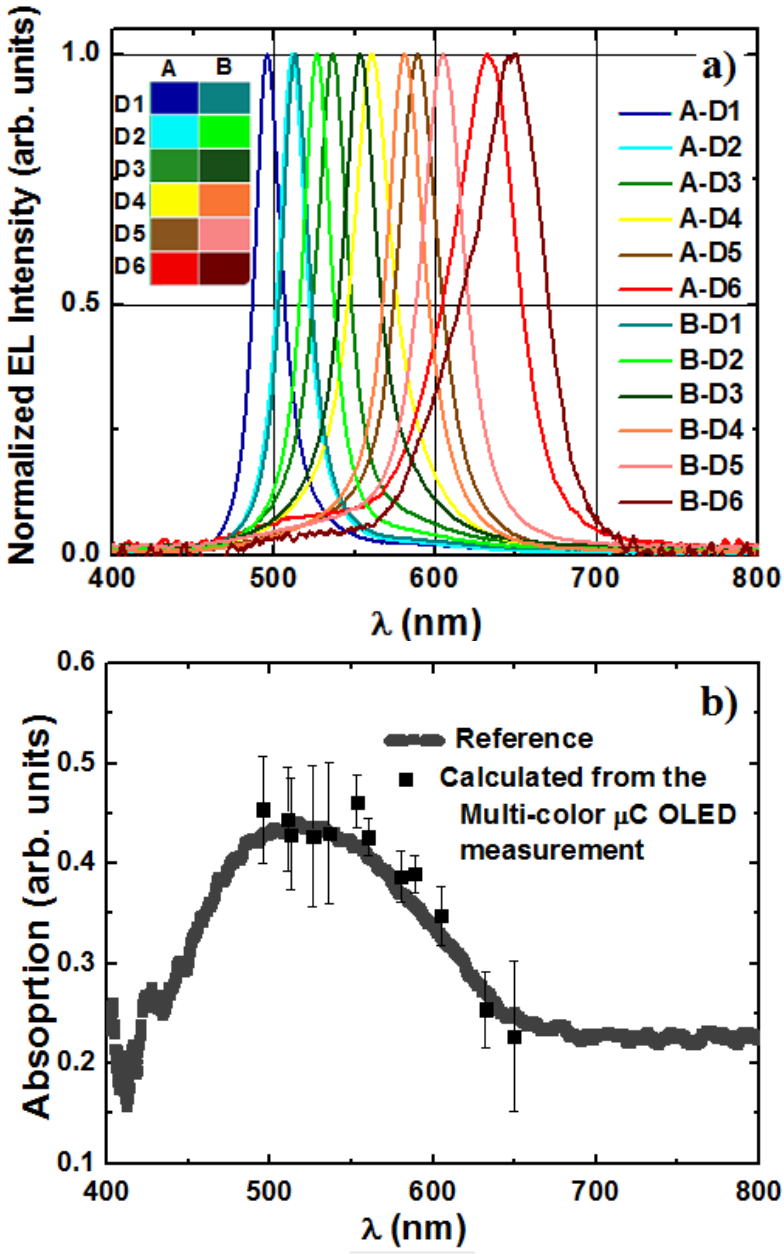

Fig. 3-3 (a) Spectra of the combinatorially fabricated multicolor μC OLEDs on one substrate. The structure is 40 nm Ag/ *i* nm MoO_3/ 49 nm α-NPB/ 1 nm 8 wt% Ir $(MDQ)_2$(acac): α-NPB/ *j* nm Alq_3/ 1 nm LiF/ 100 nm Al where *i* = 2, 5, 10, 15, 20 and 35 nm for D1, D2, D3, D4, D5 and D6, and *j* = 56 and 64 nm for A and B, respectively. (b) The absorbance of a P3HT film on a glass substrate, measured with the multi-color combinatorial μC OLEDs and a PMT, and compared with the reference performed with a standard tungsten lamp.

For each OLED pixel, a background signal was obtained by shining the OLED directly on the PMT, while the actual signal was taken after the light passed through

the P3HT film. The ratio of the difference of the two signals to the background is related to the absorption of the P3HT film. As seen in Fig. 3-3(b), the resultant absorption spectrum is in close agreement with the reference spectrum measured with a tungsten lamp in the same fashion.

3.4 Conclusions

In summary, we have demonstrated a simple monolithic fabrication method for achieving multicolor μC OLEDs by tuning the thickness of the HIL/spacer MoO_x. The peak emission wavelength was tunable from 493 to 639 nm and could be expanded by further optimization of the devices. The electrical characteristics of the OLEDs and the EL intensity remain comparable over this wide wavelength range. The variation of the emission wavelength agrees well with rigorous electromagnetic simulations of OLED emission. Comparison of device lifetimes and the *J-L-V* curves of the Alq_3-based μC OLEDs with MoO_x and CuPc as the HILs confirm the significant stability and performance improvement provided by MoO_x. The higher $L_{\perp max}$ obtained with the MoO_x-based μC OLEDs provides further evidence that the breakdown of the conventional CuPc-based OLEDs likely occurs due to Joule heating produced by the accumulated charges at the unfavorable HIL/HTL interface. Furthermore, by using the method established in this letter, an integrated spectrometer based on a two-dimensional combinatorial array of μC OLEDs was demonstrated.

Acknowledgements

We thank R. W. Mayer for film thickness measurements. Research supported by the U.S. Department of Energy, Basic Energy Sciences, Materials Sciences and

Engineering Division, under Contract No. DE-AC 02-07CH11358.

References

1. J. Shinar and R. Shinar, J. Phys. D: Appl. Phys. **41**, 133001 (2008); *Organic Electronics in Sensors and Biotechnology*, edited by R. Shinar and J. Shinar (McGraw Hill, NY, 2009).
2. M. Yoshida, A. Fujii, Y. Ohmori, and K. Yoshino, Appl. Phys. Lett. **69**, 734 (1996).
3. S. Welter, K. Brunner, J. W. Hofstraat, and L. De Cola, Nature **421**, 55 (2003).
4. C. C. Huang, H. F. Meng, G. K. Ho, C. H. Chen, C. S. Hsu, J. H. Huang, S. F. Horng, B. X. Chen, and L. C. Chen, Appl. Phys. Lett. **84**, 1195 (2004).
5. R. Reyes, M. Cremona, E. E. S. Teotonio, H. F. Brito, and O. L. Malta, Chem. Phys. Lett. **396**, 54 (2004).
6. C. J. Liang and W. C. H. Choy, Appl. Phys. Lett. **89**, 251108 (2006).
7. K. Nakamura, T. Ishikawa, D. Nishioka, T. Ushikubo, and N. Kobayashi, Appl. Phys. Lett. **97**, 193301 (2010).
8. K. O. Cheon and J. Shinar, Appl. Phys. Lett. **83**, 2073 (2003).
9. S.-C. Chang, J. Liu, J. Bharathan, Y. Yang, J. Onohara, and Junji Kido, Adv. Mat. **11**, 734 (1999).
10. X. Wu, Y. Hua, Z. Wang, J. Zheng, S. Yin, J. Deng, K. Wu, Songliu, F. Zhu, and X. Niu, Optik **117**, 373 (2006).
11. M. C. Gather , N. M. Kronenberg , and K. Meerholz, Adv. Mat. **22**, 4634 (2010).
12. S. Tokito, K. Noda, and Y. Taga, J. Phys. D: Appl. Phys. **29**, 2750 (1996).

13. J. Li, M. Yahiro, K. Ishida, H. Yamada, and K. Matsushige, Synth. Met. **151**, 141 (2005).

14. H. You, Y. Dai, Z. Zhang, and D. Ma, J. Appl. Phys. **101**, 026105 (2007).

15. H. Lee, S. W. Cho, K. Han, P. E. Jeon, C.-N. Whang, K. Jeong, K. Cho, and Y. Yi, Appl. Phys. Lett. **93**, 043308 (2008).

16. T. Matsushima, G.-H. Jin, and H. Murata, J. Appl. Phys. **104**, 054501 (2008).

17. M. Kröger, S. Hamwi, J. Meyer, T. Riedl, W. Kowalsky, and A. Kahn, Appl. Phys. Lett. **95**, 123301 (2009).

18. M. T. Greiner, M. G. Helander, Z. B. Wang, W. M. Tang, J. Qiu, and Z. H. Lu, Appl. Phys. Lett. **96**, 213302 (2010).

19. Irfan, H. Ding, Y. Gao, C. Small, D. Y. Kim, J. Subbiah, and F. So, Appl. Phys. Lett. **96**, 243307 (2010).

20. T. S. Sian and G. B. Reddy, Sol. Ener. Mat. & Sol. Cells **82**, 375 (2004).

21. F. Hamelmann, A. Brechling, A. Aschentrup, U. Heinzmann, P. Jutzi, J. Sandrock, U.Siemeling, T. Ivanova, A. Szekeres, and K. Gesheva, Thin Sol. Films **446**, 167 (2004).

22. C. L. Lin, H. W. Lin, and C. C. Wu, Appl. Phys. Lett. **87**, 021101 (2005).

23. H. Peng, J. Sun, X. Zhu, X. Yu, M. Wong, and H. S. Kwok, Appl. Phys. Lett. **88**, 073517 (2006).

24. A. Dodabalapur, L. J. Rothberg, R. H. Jordan, T. M. Miller, R. E. Slusher, and J. M. Phillips, J. Appl. Phys. **80**, 6954 (1996).

25. T. Shiga, H. Fujikawa, and Y. Taga, J. Appl. Phys. **93**, 19 (2003).

26. J. Lee, N. Chopra, D. Bera,, S. Maslov, S. H. Eom., Y. Zheng,, P. Holloway, J. Xue, and F. So, Adv. Ener. Mater. **1**, 174 (2011).

27. R. Biswas, C. Xu, W. Zhao, R. Liu, R. Shinar, J. Shinar, J. Phot. Ener. **1**, 011016 (2011).

28. S. Hermann, O. D. Gordan, M. Friedrich, D. R. T. Zahn, Phys. Status Solidi c **2**, 4037 (2005).

29. *Handbook of the Optical Constants of Solids II*, edited by E. Palik (Academic Press, Boston, 1991).

30. In our comparison experiments MoO_x and CuPc were evaporated on different parts of the same substrate, which involved multiple vacuum breaking/sample loading. This may lead to a relatively lower maximum EL compared to simply made MoO_x μC OLED. However, results from both experiments were confirmed multiple times.

Chapter 4. Microporous Phase-Separated Films of Polymer Blends for Enhanced Outcoupling of Light from OLEDs

Modified from R. Liu, Z. Ye, J.-M. Park, M. Cai, Y. Chen, K.-M. Ho,

R. Shinar, J. Shinar, Optics Express **19**, A1272 (2011).

Abstract

Thin microporous films were formed by dropcasting a toluene solution containing various ratios of polystyrene:polyethylene glycol blends on a glass substrate, with OLEDs on the ITO that coated the opposite side of that substrate. We demonstrate for the first time that such easily-fabricated films with surface and bulk micropores in the index-matching polystyrene can serve as random microlens-like arrays to improve forward OLED light extraction by up to ~60%. A theoretical interpretation of the angular emission profile of the device, considering the geometrical change at the substrate/air interface and the scattering by the pores within the films, was established in excellent agreement with the experiments. The use of such blended thin films provides an economical method, independent of the OLED fabrication technique, for improving the outcoupling efficiency.

4.1 Introduction

Extensive research has been conducted on OLEDs for their potential applications in flat panel displays, solid-state lighting and integrated (bio)chemical sensing [1-4]. Although efficient and long-lived OLEDs have been realized via utilizing advanced materials and device architectures, a significant limiting issue is their relatively low

forward outcoupling efficiency (η_{out}) [5-19]. Earlier studies have shown that η_{out} of conventional OLEDs is limited to ~20% due to waveguiding within the organic layers/ITO and the glass substrates, which is caused by total internal reflection at the ITO/glass and glass/air interfaces, respectively [5]. To achieve better light extraction, various methods have been utilized, which can be classified into three major categories: (*i*) Modification of the emitting species, e.g., increasing the population of horizontally oriented emitting dipoles [6]; (*ii*) Modification of the ITO/substrate structure or interface, by e.g., utilizing low index grids [5,7], corrugated or nanoporous anode structures [8-10], and high index substrates [11]; (*iii*) Modification of the substrate/air interface, by e.g., using truncated luminaires [12], ZnS nanocolumns [13], macrolenses [14], and microlenses (μLs) [15-21].

The modification of the substrate/air interface has drawn great interest due to the variety of methods and the fact that it does not interfere with device fabrication. In particular, various methods have been established to construct μLs using, for instance, imprint lithography via-different routes [15-19,22,23] and self-assembled materials [20,21]. However, multi-step substrate transfer and lithography and curing processes in the above-mentioned methods remain a challenge for mass production on large areas. Thus, an economical method with complete independence from the OLED fabrication method is highly desirable.

It should be noted that not only convex-shaped μLs [15-19], but also concave-shaped ones [22,23] can lead to better light extraction as long as they reduce the total internal reflection at the glass/air interface. To our knowledge, this paper

demonstrates for the first time index-matching films with micropores, formed by polymer phase separation in blended layers during the drying process, which can be used as "random microlens arrays (μLAs)" to enhance η_{out}.

Due to intrinsic differences in miscibility of many macromolecular constituents of blends, polymer solutes will typically separate during the drying process of films fabricated by solvent-casting [24]. This de-mixing process of a multicomponent blend often results in a phase separated morphology that may be beneficial for many applications. For example, microporous structures derived from this method have been widely adopted for photonic crystals [25], membrane filters [26], and drug delivery [27]. Earlier research has demonstrated such structures using materials with a refractive index *n* similar to glass, such as polystyrene (PS) (*n*~1.55-1.59) [28-30]. In this paper, we show that the micro-porosity formed in films prepared from blends of PS and polyethylene glycol (PEG) can enhance η_{out} by up to ~60%. Such a simple technique is very promising as it is economical and the fabrication of the film is an independent process, i.e., it can be done before or following device fabrication and encapsulation. Moreover, by controlling the total concentration of the solution, the dropcast volume, and the ratio of the mixed polymers one can easily control the thickness, size and filling factor of the film [28-30]. This advantage will enable future systematic and detailed investigation of the effect of the geometrical properties of the "random μLAs" on extracting light.

4.2 Experimental procedure

For OLED fabrication, the ITO was patterned and etched to form anode stripes. It was

then thoroughly cleaned with surfactant, acetone and isopropanol and treated in a UV/ozone oven. The OLED was fabricated by thermal evaporation of the organic layers, LiF, and Al in a vacuum chamber (background pressure ~ 10^{-6} Torr) located in an Ar-filled glovebox. The rate of the organic layers' evaporation was ~ 1Å/s. The pixel size was 3×3 mm^2.

The PS (molecular weight M_w ~280,000) and PEG (M_ws ~200, ~400, ~1,000, and ~8,000) were purchased from Sigma-Aldrich. The microporous films were formed by dropcasting 50-200 μL of toluene solution containing PS:PEG mixtures with different weight ratios (the total concentrations were 60 or 90 mg/mL) on the backside of the OLED ITO/glass substrate. The films were dried under ambient conditions in a fume hood following the dropcasting. Experiments with films washed with methanol, which results in removal of surface PEG, were also conducted, however, this approach did not present an advantage and the enhancement was generally lower than with un-washed films. The best results, presented here, were obtained by using PEG of M_w ~1000 and 200 μL of 60 mg/mL solution to form the film. The SEM images of the films' surface morphology and side view were taken with a JEOL model 5910v microscope. In order to prevent charging, a 15 nm Ag layer was deposited on top of the films.

To determine n of the PS:PEG film we measured the optical transmission of a film prepared by spin-coating a toluene solution containing 54:6 mg/mL PS:PEG at 3000 rpm on a 200 μm thick sapphire substrate (n ~ 1.77@ ~500 nm). This procedure was used due to the rough surfaces of the dropcast films and their n value that is very close

to that of the glass. The interference fringes yielded n~1.58-1.61 in the range 1.4-2.3 μm.

For measurement of the overall emission spectra, the OLEDs were placed at the window of an integrating sphere with all sides, except for the front emitting surface, covered with black tape. The electroluminescence (EL) spectra were then recorded by an Ocean Optics Chem 2000 spectrometer. For the angular emission profile measurements, the pixels were placed in the center of a goniometer, sufficiently far (~64 cm) from the detector, so that the emitting area could be approximated as a point source. The light intensity was detected through a long dark pipe by a Hamamatsu R6060-02 photomultiplier. The photocurrent was monitored by a Keithley 2400 source-meter.

4.3 Results and discussion

Mixtures of PS:PEG in toluene with different weight ratios ranging from 1:0 to 1:1 were dropcast onto the backside of the OLED ITO/glass substrate. Fig. 4-1(a) shows schematically the process of micropore formation on the surface and in the bulk of the film, which is similar to earlier descriptions [28,29]. Note that the schematic does not show the non-uniformity in the pore density. The high molecular-weight PS with matching n ~ 1.55-1.59 has a lower solubility in toluene than the low molecular weight PEG (n ~ 1.46). Hence, during the drying process of the solution, PS first precipitates while small PEG-rich droplets are formed on the surface and in the bulk. During the evaporation of the solvent, the PEG droplets shrink, leaving behind surface and bulk PEG-coated PS micropores, as shown in Fig.

4-1(a). The resulting films with ≥ 50% high-M_w PS are mechanically stable due to the entanglement of the long polymer chains. The PEG at the surface can be washed away by polar solvents without dissolution of the PS. However, because of the smaller *n* of PEG in comparison to PS, the PEG coating of the micropores do not negatively affect the outcoupling function of the film.

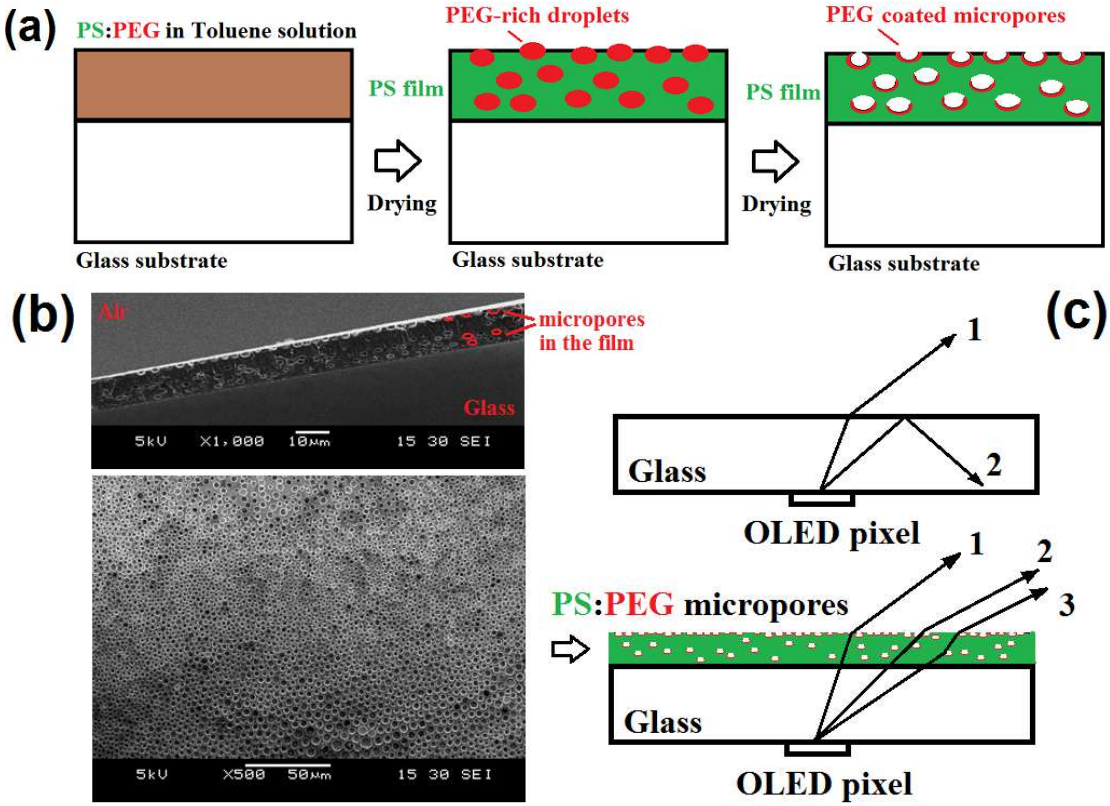

Fig. 4-1 (a) Schematic demonstration of the microporous structure formation of the PS:PEG mixed film during the drying process following dropcasting; note that the actual pore density is not uniform. (b) SEM images of the surface and cross section of a film with 48:12 mg/mL PS:PEG. (c) The principle of the OLED outcoupling enhancement by the PS:PEG film.

As an example, the microporous structure formed by dropcasting 48:12 mg/mL PS:PEG in toluene is shown in the SEM images of Fig. 4-1(b). The size of the micropores ranges from ~1.5 μm to ~5 μm in diameter. They are densely packed at the surface and randomly distributed at a lower density within the bulk of the film. As shown next, the pores enhance light extraction through the glass substrate of an

OLED.

In a regular OLED, only those light rays with an incident angle smaller than the critical angle (Ray 1, Fig 4-1(c)) can escape at the substrate/air interface. However, with the index-matching PS film and the surface micropores, the light rays that were previously waveguided within the substrate (Ray 2) are now extracted due to the change of the substrate/air interface geometry. Additionally, some of the light rays may also be scattered by the pores within the bulk of the PS:PEG film (Ray 3), and hence change to directions that are forward-extracted.

Fig.4-2(a) shows the actual outcoupling enhancement by a 54:6 mg/mL PS:PEG film, for a conventional tris(8-hydroxyquinolinato) Al (Alq_3)-based OLED with the structure ITO/5 nm MoO_3/56 nm *N*,*N*'-bis(naphthalen-1-yl)-*N*,*N*'-bis(phenyl)benzidine (NPB)/64 nm Alq_3/1 nm LiF/100 nm Al. The emission from an OLED with the same structure, but without the PS:PEG film is also shown. Both devices were lit under the same conditions. As seen, the light emitted from the pixel with the PS:PEG film is brighter and diffuse in comparison to the emission from the pixel without the microporous film. Additionally, the rim of the device (an epoxy sealant used for device encapsulation, sealing the gap between the OLED's glass substrate and an additional glass cover) without the PS:PEG film is much brighter, indicating that a large fraction of the light is waveguided to the edge of the glass substrate. In contrast, the dark rim of the device with the PS:PEG film (left image) clearly demonstrates the enhanced forward light extraction by the PS:PEG film.

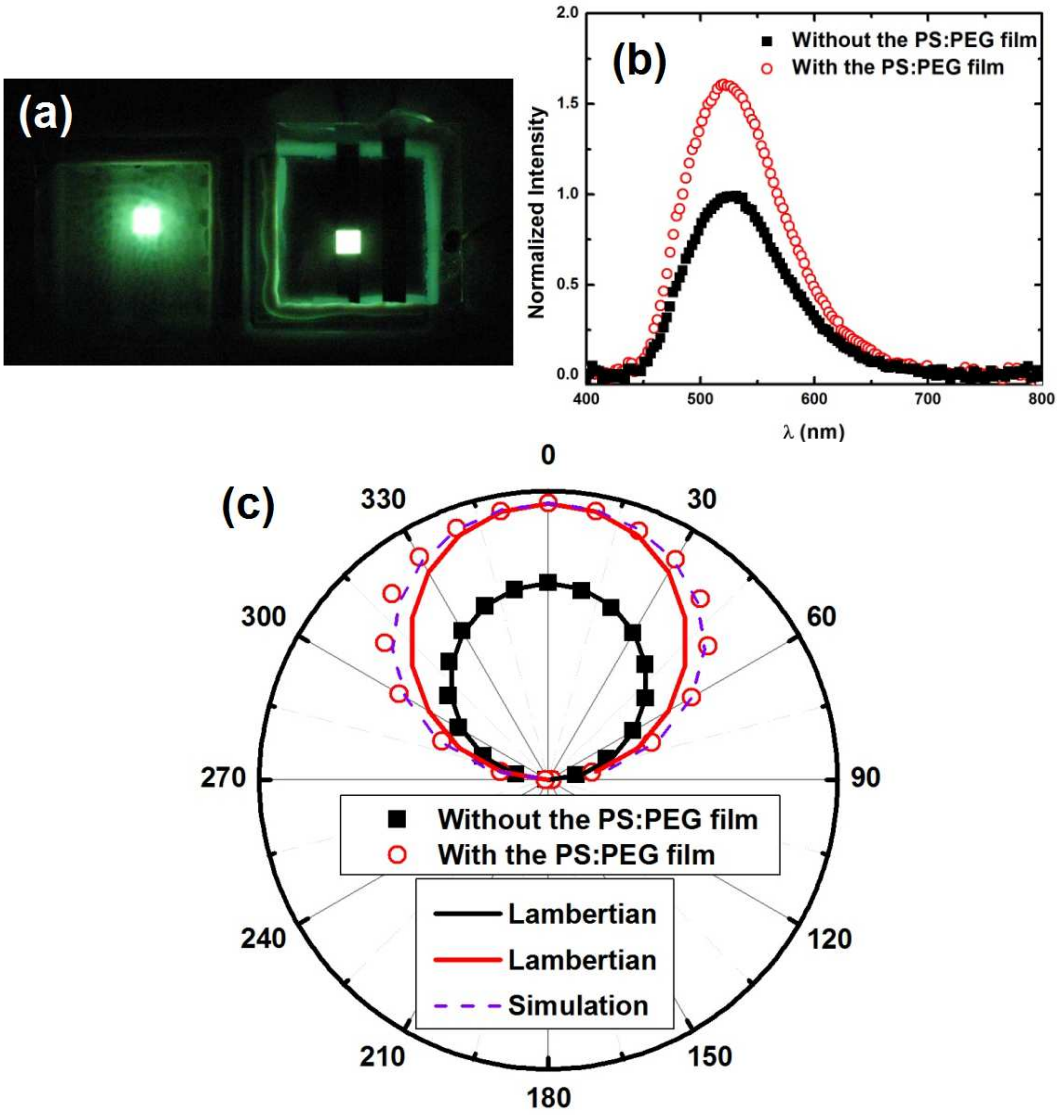

Fig. 4-2 Effect of 200 μL PS:PEG 54:6 mg/mL in toluene that were dropcast on the backside of the OLED's ITO/glass substrate. (a) Images of two pixels with and without the PS:PEG film, each biased at 6 V. The dropcast area is 1×1 in.^{2} (b) Overall emission spectra of the devices with (red open circles) and without (black solid squares) the PS:PEG film. The current density in each device was J = 55 mA/cm^2 (c) Angular emission intensity profile of the device with (red open circles) and without (black solid squares) the PS:PEG film. In each device J = 5.5 mA/cm^2 The solid lines are the Lambertian emission profiles. The dashed purple line is the simulated emission profile. We note that the enhancement was essentially independent of J and consequently, of course, the brightness L, in agreement with other studies [16].

In order to quantify the outcoupling enhancement of the PS:PEG film, we measured the overall emission spectra of the devices using an integrating sphere, as shown in Fig. 4-2(b). The peak emission of the device with the PS:PEG film was

slightly blue shifted to 516 nm from the 525 nm peak of the conventional device. This is attributed to the scattering effect of the micropores. The integration of the spectra yields an enhancement of ~61%. Furthermore, Fig. 4-2(c) shows the angular emission-intensity profile of the devices. As clearly seen, the emission profile of the device with the PS:PEG film was enhanced at all angles, but it deviates from a Lambertian profile, with increased intensity at higher angles. Assuming the emission profile has azimuthal symmetry, the integrated enhancement is ~57%, which is consistent with the spectral measurement. Fig. 4-2(c) also shows the simulation results (discussed next) of the PS:PEG effect, which are in good agreement with the experimental results. We note that the enhancement was essentially independent of the current density *J* and consequently, of course, brightness *L*, in agreement with other studies [16].

The physical interpretation of the enhancement of the light extraction and the consequential angular emission profile lies in the geometrical change of the substrate/air interface morphology and the scattering effect of the embedded voids. Let $I_0(\theta_0)$ and $I_1(\theta_1)$ be the angular energy distribution in the emitting layer and in the PS:PEG film, respectively. In the absence of pores, due to energy conservation, $I_0(\theta_0)\sin\theta_0 d\theta_0 = I_1(\theta_1)\sin\theta_1 d\theta_1$, and with Snell's law $n_{org}\sin\theta_0 = n_{PS:PEG}\sin\theta_1$ we get [31],

$$I_1(\theta_1) = \frac{I_0(\theta_0)\sin\theta_0 d\theta_0}{\sin\theta_1 d\theta_1} = \frac{n_{PS:PEG}^2\cos\theta_1}{n_{org}^2\cos\theta_0} I_0(\theta_0) = \frac{n_{PS:PEG}^2\cos\theta_1}{n_{org}^2\sqrt{1-\left(\frac{n_{PS:PEG}}{n_{org}}\sin\theta_1\right)^2}} I_0(\theta_0) \quad (4.1)$$

Similarly, the external luminous energy distribution is given by

$$I_2(\theta_2) = \frac{n_{air}^2 \cos\theta_2}{n_{org}^2 \sqrt{1-\left(\frac{n_{air}}{n_{org}}\sin\theta_2\right)^2}} I_0(\theta_0), \qquad (4.2)$$

where θ_2 is the viewing angle in the far field. Assuming isotropic emission, $I_0(\theta_0)$ = 1/(2π), Eq. (4.2) yields

$$I_2(\theta_2) = \frac{1}{2\pi} \frac{n_{air}^2 \cos\theta_2}{n_{org}^2 \sqrt{1-\left(\frac{n_{air}}{n_{org}}\sin\theta_2\right)^2}}, \qquad (4.3)$$

which approximately resembles a Lambertian profile when $n_{org} >> n_{air}$.

In the presence of micropores in the PS:PEG film, we assume the incoming light undergoes two processes: (i) scattering by the voids embedded within the film to uniformly distributed random directions, and (ii) refraction by the micropores at the top surface of PS:PEG, where part of light originally trapped in PS:PEG is extracted. The above assumptions may not be accurate for a real device, yet they can provide a qualitative analysis. Under these assumptions, the modified angular distribution in PS:PEG is given by

$$I_1'(\theta_1) = \begin{cases} C_1 & when\ \theta_1 \le \theta_c \\ C_2 & when\ \theta_1 > \theta_c \end{cases}, \qquad (4.4)$$

where C_1 and C_2 are constant, and $\theta_c = \sin^{-1}(n_{air}/n_{PS:PEG})$ is the critical angle at the PS:PEG/air interface. If we don't consider process (ii), the uniformly random scattering in process (i) gives $C_1 = C_2$. However, the refraction by surface micropores in process (ii) changes the incident angle for each ray, and helps part of the PS:PEG guided light to outcouple (changing $\theta_1 > \theta_c$ to $\theta_1 < \theta_c$), which results in $C_2 < C_1$. In

an ideal case where all PS:PEG guided light is extracted via surface micropores and there is no absorption in the device, $C_2 = 0$ and $C_1^{ideal} = 0.359$ can be calculated from energy conservation.

After determining the expression for $I_1'(\theta_1)$, the external luminous energy distribution in the presence of micropores can be obtained from

$$I_2'(\theta_2) = C_1 \frac{n_{air}^2 \cos\theta_2}{n_{PS:PEG}^2 \sqrt{1-\left(\frac{n_{air}}{n_{PS:PEG}}\sin\theta_2\right)^2}}. \qquad (4.5)$$

Comparing Eqs. (4.3) and (4.5), we see that $I_2'(\theta_2)$ deviates from a Lambertian profile more than $I_2(\theta_2)$, since $n_{air}/n_{PS:PEG} > n_{air}/n_{org}$. Assuming $n_{PS:PEG} \approx 1.58$ we obtain excellent agreement between the calculated emission profile and the experimental profile (Fig. 4-2(c)). We note that the n of the matrix is not as crucial as the scattering factor C_1 in the model for determining the enhancement and emission profile. The use of n_{PEG}=1.48 (not shown) resulted in a nearly identical emission profile.

In Fig. 4-3, we further demonstrate the ability to control the size and fill factor of the micropores. PS:PEG films with the same total concentration (60 mg/mL) but different weight ratios (ranging from 1:0 to 1:1 PS:PEG ratio) were fabricated and imaged using SEM. Although there is macroscopic domain formation caused by heat convection [29], Fig. 4-3 can adequately represent the microscopic structures formed in these films. Starting from the undoped PS film, as the concentration of PEG increases, the fill factor of the surface micropores increases until they fully cover the

surface of the film (PS:PEG 4:1 ratio). This behavior is in accordance with the earlier interpretation of the micropores' formation process (Fig. 4-1a). The device with the pure PS film barely shows any outcoupling enhancement, which confirms the role of the microstructure in enhancing light extraction. The increasing density of pores increases the scattering probability and at an optimal pore size and distribution, it maximizes the forward light extraction at the substrate/air interface. Indeed, as clearly shown in Table 4.1, the enhancement factor relative to conventional OLEDs increases from 3% for undoped to ~60% for 10 wt.% PEG-doped PS. As the concentration of PEG further increases, the closely packed PEG-rich droplets formed during the drying process coalesce to form larger concave structures (Fig. 4-3). These structures, with a relatively smaller curvature but increased size, reduce the outcoupling enhancement.

	Undoped PS	PS:PEG 19:1	PS:PEG 9:1	PS:PEG 4:1	PS:PEG 2:1	PS:PEG 1:1
Enhancement	3%	40%	61%	58%	46%	38%
C_1		0.1	0.18	0.18	0.17	0.16

Table 4.1. Comparison of the outcoupling enhancement factor by PS:PEG films with different weight ratios (total concentration: 60 mg/mL). The values of C_1 extracted from the enhancement factors are also listed.

Table 4.1 also summarizes the values of C_1 (see Eq. (4-5)) calculated from the experimental enhancement factor. These values are much smaller than the calculated ideal value of 0.359 which indicates only partial extraction of the trapped light by the PS:PEG film. The increase of C_1 from a device with undoped PS to a device with a 9:1 PS:PEG film is due to the change of the interface geometry and the increased density of scattering centers within the film. The decrease of C_1 when the PEG concentration is further increased is attributed to the reduced light extraction caused by the smaller curvature of the larger PEG-coated micropores on the surface(Fig. 4-3).

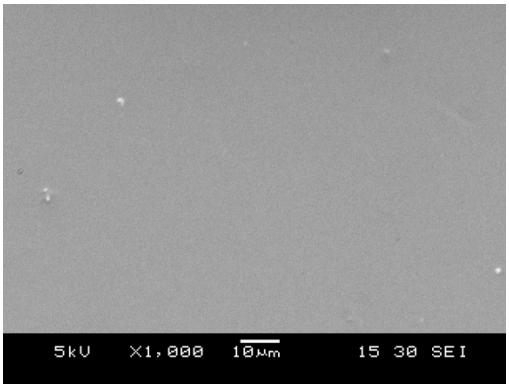

Undoped PS 60 mg/mL

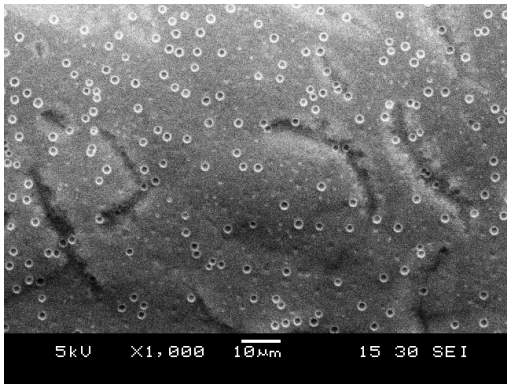

PS:PEG 19:1 ratio 57:3 mg/mL

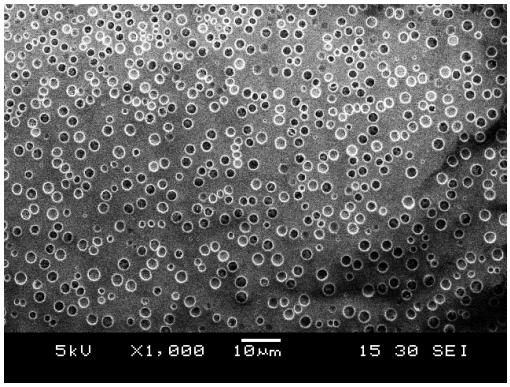

PS:PEG 9:1 ratio 54:6 mg/mL

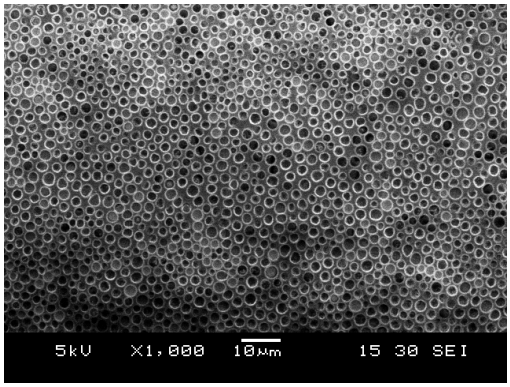

PS:PEG 4:1 ratio 48:12 mg/mL

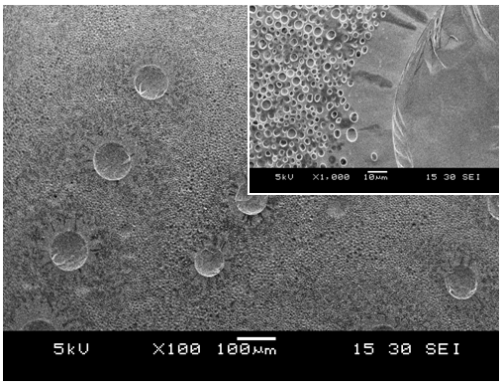

PS:PEG 2:1 ratio 40:20 mg/mL

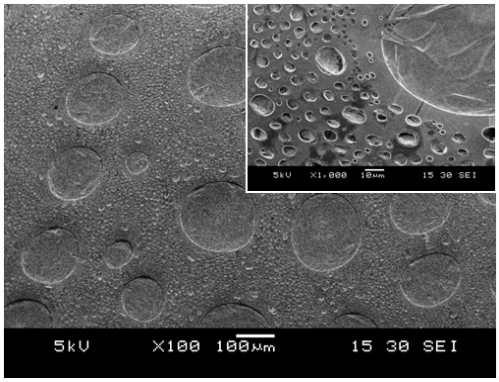

PS:PEG 1:1 ratio 30:30 mg/mL

Figure 4-3. The surface SEM images of the PS:PEG films with different weight ratios, but constant total concentration of 60 mg/mL. The scale bar in the insets is 10 μm.

To demonstrate the potential generality of this method, 48:12 mg/mL of PS: poly(vinyl pyrrolidone) (PVP) in chloroform were also applied on the backside of the substrate of an OLED, as a similar microporous structure was demonstrated earlier for this blend [30]. Such structures also resulted in η_{out} enhancement, but only by ~32%.

Finally, we note that we recently showed that if the conventional ITO anode is

replaced by several layers of high conductivity poly(3,4-ethylenedioxythiophene) poly(styrenesulfonate) (PEDOT:PSS), the OLED power efficiency can increase by up to 80% [32]. This modification of the anode can be combined with the technique shown in this paper to generate an even higher device efficiency.

4.4 Conclusions

We successfully fabricated controlled microporous structures by dropcasting toluene solutions of various PS:PEG ratios on the blank glass side opposite to the glass/ITO OLED structures. The microstructures of these films enhance the forward light extraction by scattering the light that is otherwise trapped in the OLED's glass substrate. An enhancement of ~60% was achieved by optimizing the size and filling factor of the micropores formed in the PS:PEG film; the optimal PS:PEG weight ratio was found to be 9:1 – 4:1. The agreement between a theoretical analysis of the non-Lambertian angular intensity profile and the experiments is excellent, clearly showing that this enhancement originates from scattering by both surface and bulk micropores. Additionally, the non-Lambertian distribution provides increased emission intensity at larger angles. Hence, this approach provides an extremely simple and economical means for outcoupling enhancement in OLEDs and potential applications in OLED-based luminaires.

Acknowledgements

This work was supported by the US Department of Energy, Basic Energy Sciences, Materials Sciences and Engineering Division, under Contract No. DE-AC

02-07CH11358.

References

1. S.R. Forrest, Nature **428**, 911 (2004).
2. *Organic Electronics: Materials, Processing, Devices and Applications*(Ed: F. So, CRC, 2010)
3. *Organic Electronics in Sensors and Biotechnology* (Eds: R. Shinar and J. Shinar, McGraw-Hill, 2009)
4. J. Shinar, and R. Shinar, J. Phys. D: Appl. Phys. **41**, 133001 (2008).
5. Y. Sun, and S. R. Forrest, Nature Photonics **2**, 483 (2008).
6. J. Frischeisen, D. Yokoyama, A. Endo, C. Adachi, and W. Brütting, Organic Electronics **12**, 809 (2011).
7. M. Slootsky, and S. R. Forrest, Optics Letter **35**, 1052 (2010).
8. W. H. Koo, S. M. Jeong, F. Araoka, K. Ishikawa, S. Nishimura, T. Toyooka, and H. Takezoe, Nature Photonics **4**, 222 (2010).
9. A. O. Altun, S. Jeon, J. Shim, J.-H. Jeong, D.-G. Choi, K.-D. Kim, J.-H. Choi, S.-W. Lee, E.-S. Lee, H.-D. Park, J. R. Youn, J.-J. Kim, Y.-H. Lee, and J.-W. Kang, Organic Electronics **11**, 711 (2010).
10. H. J. Peng, Y. L. Ho, X. J. Yu, and H. S. Kwok, J. Appl. Phys. **96**, 1649 (2004).
11. S. Mladenovski, K. Neyts, D. Pavicic, A. Werner, and C. Rothe, Optics Express **17**, 7562 (2009).
12. B. W. D'Andrade, and J. J. Brown, Appl. Phys. Lett. **88**, 192908 (2006).

13. L. Lu, F. Zhang, Z. Xu, S. Zhao, Z. Zhuo, D. Song, J. Li, and Y. Wang, Physica B **405**, 3728 (2010).

14. S. Reineke, F. Lindner, G. Schwartz, N. Seidler, K. Walzer, B. Lüssem, and K. Leo, Nature **459**, 234 (2009).

15. J.-M. Park, Z. Gan, W.Y. Leung, R. Liu, Y. Zhou, K. Constant, J. Shinar, R. Shinar, and K.-M. Ho, Optics Express **19**, A786 (2011).

16. Y. Sun, and S. R. Forrest, J. Appl. Phys. **100**, 073106 (2006).

17. J. Lim, S. Oh, D. Kim, S. Cho, I. Kim, S. Han, H. Takezoe, E. Choi, G. Cho, Y. Seo, S. Kang, and B. Park, Opt. Express **14**, 6564 (2006).

18. H. Lin, Y. Ho, J. Lee, K. Chen, J. Fang, S. Hsu, M. Wei, H. Lin, J. Tsai, and T. Wu, Opt. Express **16**, 11044 (2008).

19. S.-H. Eom, E. Wrzesniewski, and J. Xue, Organic Electronics **12**, 472 (2011).

20. W.-K. Huang, W.-S. Wang, H.-C. Kan, and F.-C. Chen, Jpn. J. Appl. Phys. **45**, L1100 (2006).

21. J. A. Zimberlin, P. Wadsworth, and A. J. Crosby, Cell Motil Cytoskeleton. **65**, 762 (2008).

22. P. Ruffieux, T. Scharf, I. Philipoussis, H. Herzig, R. Voelkel, and K. Weible, Opt. Express **16**, 19541 (2008).

23. J. S. Kim, D. S. Kim, J. J. Kang, J. D. Kim, and C. J. Hwang, Polymer Eng. & Sci. **50**, 1696 (2010).

24. S. Walheim, M. Böltau,, J. Mlynek, G. Krausch, and U. Steiner, Macromolecules **30**, 4995 (1997).

25. J. E. G. J. Wijnhoven, and W. L. Vos, Science **281**, 802 (1998).

26. M. Ulbricht, Polymer **47**, 2217 (2006).

27. G. K. Stylios, P. V. Giannoudis, and T. Wan, Injury **36**, S6 (2005).

28. J.-K. Kim, K. Taki, and M. Ohshima, Langmuir **23**, 12397 (2007).

29. J.-K. Kim, K. Taki, S. Nagamine, and M. Ohshima, Langmuir **24**, 8898 (2008).

30. K.-H. Wu, S.-Y. Lu, and H.-L. Chen, Langmuir **22**, 8029 (2006).

31. C. F. Madigan, M.-H. Lu, and J. C. Sturm, Appl. Phys. Lett. **76**, 1650 (2000).

32. M. Cai, T. Xiao, R. Liu, Y. Chen, R. Shinar, and J. Shinar, Appl. Phys. Lett. **99**, 153303 (2011).

Chapter 5. Organic Light Emitting Diode Sensing Platform: Challenges and Solutions

Modified from R. Liu, Y. Cai, J.-M. Park, K.-M. Ho, J. Shinar, R. Shinar, Adv. Funct. Mater. **21**, 4744 (2011).

Abstract

The organic light-emitting diode (OLED)-based sensing platform is gaining momentum due to unique attributes of the compact OLEDs that are used as excitation sources. This paper, however, points to issues related to this sensing platform that will affect many (bio)chemical sensing applications, in particular in photoluminescence (PL)-based sensors operated in the advantageous time domain, where pulsed OLEDs are utilized. The issues are related to the post-pulse electroluminescence (EL) profile, i.e., transient EL, which depends on the OLED materials and structure, and to the long-wavelength tail of the typically broad-band EL spectrum. Depending on materials and device structure, the transient EL may exhibit spikes peaking at ~100-200 ns and μs-long tails. As shown, these interfere with the determination of PL decay times (that are related to analyte concentrations) of sensing elements. The results also indicate that the long-wavelength tail of the EL spectrum contributes to the interfering post-pulse μs-long EL tail. Hence, it is shown that the choice of OLED materials, the use of microcavity (μC) OLEDs with tunable, narrower EL bands, and the use of UV OLEDs alleviate these issues, resulting in more reliable data analysis. Furthermore, a 2-D uniform 2 μm-pitch microlens array that was previously used for improving light extraction from the OLEDs (J.-M. Park et al., *Optics Express* **2011**,

19, A786) is used for directional PL scattering toward the photodetector, which leads to a ~2.1-3.8 fold enhancement of the PL signal. This behavior is shown for oxygen sensing, which is the basis for sensing of bioanalytes such as glucose, lactate, ethanol, cholesterol, and uric acid.

5.1 Introduction

5.1.1. Organic electronics in sensing applications

The growing progress in organic electronics, i.e., the field of (opto)electronic devices utilizing conjugated organic active layers, has led to emerging R&D in various organic electronics-based (bio)chemical sensing and biotechnology applications [1]. As examples, luminescent conjugated polymers have been used to gain insight into biology and pathology of protein aggregation diseases [2], and for designing electrochemical switches and ion pumps for cell biology studies [3,4]. Organic thin film transistors (OTFTs) were implemented to develop cost-effective and label-free DNA or protein sensor chips [5], and organic light-emitting diodes (OLEDs) have been evaluated as excitation sources in photoluminescence (PL)-based sensing of analytes, such as oxygen, ethanol, glucose, lactate, and cholesterol [1,6-13]. Other examples of the use of OLEDs (including polymer LEDs (PLEDs)) in sensing applications include an integrated PL-based oxygen and *p*H sensor, utilizing an OLED as the light source and an organic photodetector (PD) [13-16]; two polarizers were used for separating the PL and the OLED's electroluminescence (EL) [13]. OLEDs were used also for fluorescence detection of proteins [17] and PLEDs were used as an

integrated excitation source for microfabricated capillary electrophoresis [18]. The use of PLEDs for monitoring biomolecules labeled with fluorescent dyes by monitoring shifts in the PLED's EL [19] and a surface plasmon resonance sensor utilizing an OLED and a metallic sensing layer were also reported [20]. A nanotextured OLED-based chemical sensor for label-free detection of methanol and ethanol was demonstrated [21]. The detection was based on monitoring analyte-induced changes in the OLED turn-on voltage and EL intensity. In another example, a refractometer with an integrated OLED light source and dual organic PDs were used for sensitive analyte detection by monitoring the change in light flux from the OLED to the PD that resulted from changes in refractive index of the analyte solution relative to a reference solution [16].

Good detection sensitivities are often obtained using OTFT- and OLED-based sensors, and the issue of the long-term stability that affects the organic devices is often less important in their sensing platforms, as the sensing probes are often shorter lived than the OLEDs. Moreover, as the cost of OTFTs and OLEDs is expected to drop, they are promising for use in disposable sensors.

5.1.2. OLED-based PL sensors

The attraction of OLEDs for PL-based and other sensing applications is due to their small size (nm to mm pixels) [1,22], ease of fabrication via thermal evaporation or solution processing on simple substrates such as glass and plastic, and therefore, their compatibility with microfluidic architectures [1,23]. Additionally, they are flexible in size and design, and can be easily structurally integrated with the sensing

probes, and with thin-film PDs to generate very compact, yet reliable monitors.

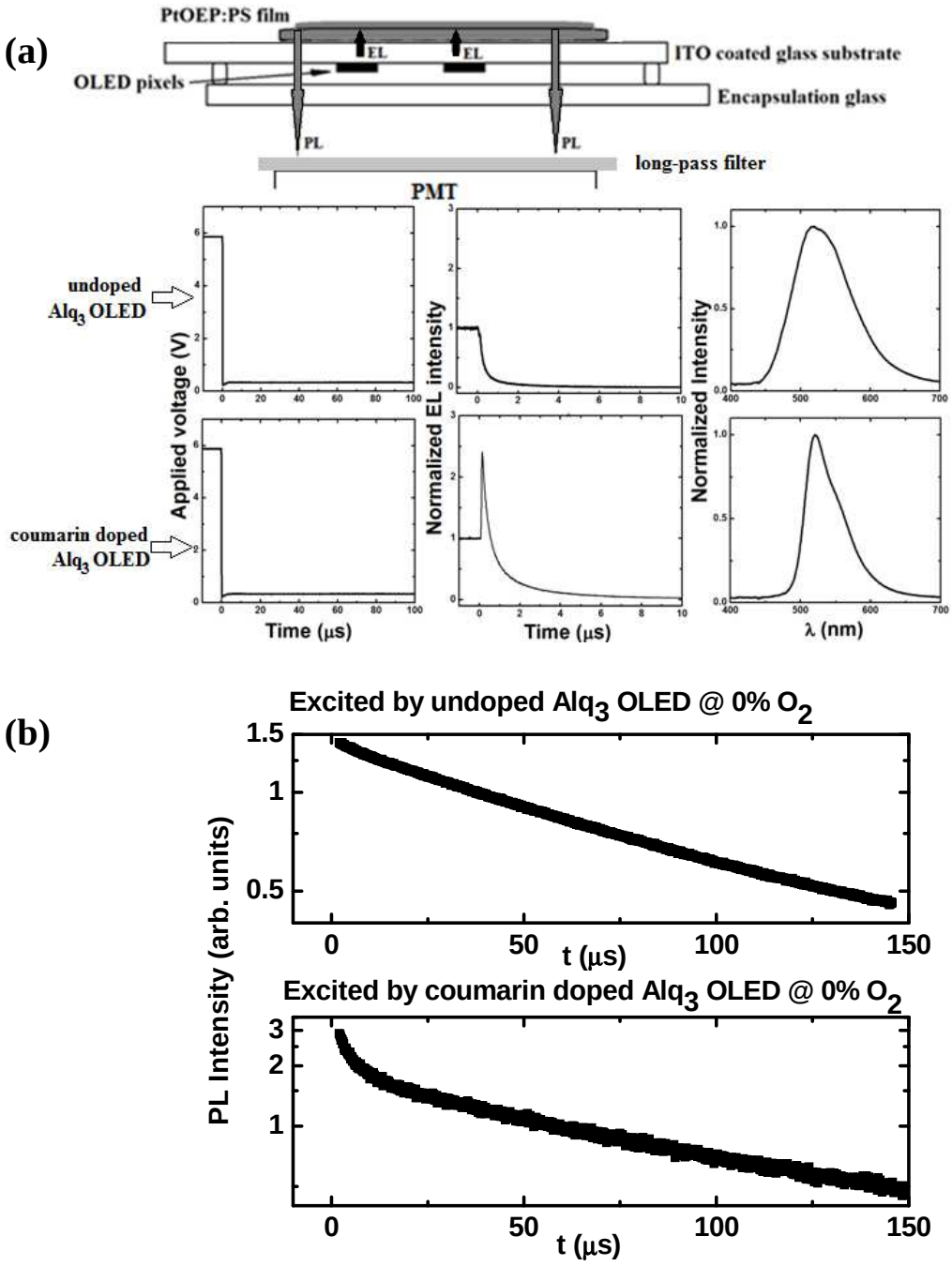

Fig. 5-1 (a) The set-up of the conventional OLED-based oxygen sensor probe: PtOEP:PS film excited by Alq_3-based OLEDs and the transient bias pulse, excitation EL and the on-pulse spectra of the undoped and coumarin-doped Alq_3 OLEDs while operation, where the undoped OLED structure is ITO/5 nm CuPc/50 nm NPB/40 nm Alq_3/1 nm LiF/~120 nm Al; in the doped device coumarin was doped into the first 2 nm of the Alq_3 layer. (b) The PL decay signal of a PtOEP:PS film excited by undoped and coumarin-doped OLEDs at 0% O_2

The schematic configuration of Fig. 5-1(a) shows an integration of the sensing

film and the excitation OLED using the back-detection geometry which largely prevents the distortion of the signal from the excitation source. As such, the potential of OLEDs to be used in badge-size and miniaturized sensor arrays surpasses that of many excitation sources. Indeed, compact structures with OLEDs and thin-film Si- or organic-based PDs have been demonstrated, including with operation in the time domain [6-11,23-25].

For sensing applications, OLEDs (that generally comprise of organic layers sandwiched between two electrodes; indium tin oxide, ITO, often serves as the transparent anode) are often fabricated as an array of individually-addressable small-size pixels, and as such are suitable for monitoring multiple analytes. Indeed, initial results showed the OLEDs' potential in a lab on a chip PL-based bioplatform [23], and in compact multianalyte sensors with other designs [9,23,26,27].

Earlier studies have shown that the outcoupling efficiency of conventional OLEDs is limited to ~20% due to waveguiding within the organic layers/ITO and within the glass layers, which is caused by total internal reflection at the ITO/glass and glass/air interfaces, respectively [28]. In some OLED structures the outcoupling efficiency is further reduced by EL quenching by surface plasmon (SP) modes associated with metallic cathodes [29]. Various methods have been used to alleviate this problem. Better outcoupling efficiency is achieved by utilizing SP-mediated emission [29], low index grids [28], corrugated anode structures [30], and micro- [31] or macro-lenses [32] on the backside of the substrates. Among these approaches, microlens arrays (μLAs) are most promising in combining with the OLED-based biochemical sensing

platform due to their low cost, ease of fabrication, and minimal influence on the device preparation process. In this paper we show that such a μLA can be utilized also to enhance the PL by scattering it toward the PD.

5.1.3. PL-based oxygen sensor

The detection of oxygen in this work is based on monitoring O_2-induced changes in the PL intensity (I) or PL decay time (τ) of the oxygen sensitive dye Pt octaethylporphyrine (PtOEP) embedded in a polystyrene (PS) matrix [1,6-11,23-25, 33,34]. Analysis was based on the well known Stern-Volmer (SV) equation [1,6].

$$I_0/I = \tau_0/\tau = 1 + K_{SV}[O_2] \qquad (5.1).$$

where I_0 and τ_0 are the unquenched values, K_{SV} is the SV constant, and $[O_2]$ is the O_2 level. We have recently shown [10] that in our studies the PL decay time obeys an exponential fit only in the absence of the quencher (i.e., in Ar or N_2 atmospheres). In the presence of O_2, however, in particular as $[O_2]$ increases, the PL decay curve deviates from a simple exponent due to inhomogeneity in the sensing film [35-39].

We typically use the red-emitting PtOEP together with green tris-(8-hydroxyquinoline) Al (Alq_3)-based OLEDs. These OLEDs have been well-studied and they are easy to fabricate and can maintain decent luminescence for months if encapsulated. Monitoring analytes in the time domain is possible if the PL decay time is significantly longer than that of the response time of the measurement system. This approach is advantageous as minor changes in the background light, the sensing probe, or the excitation source do not affect sensor performance. As proved in earlier studies and in later content of this paper the PL decay time is an intrinsic

quantity, independent of the light intensity [1,6-13,23-25,33,34]. Hence, frequent calibration and a reference sensor are avoided and more compact devices, devoid of optical filters, can be fabricated.

As studies of OLED-based (bio)chemical sensing expand several issues emerge. In this paper we present such issues and approaches to alleviate them. These issues are related to the OLED materials and configuration, the width of the OLED's EL band, and the OLED's post-pulse (transient) EL profile. This situation is of importance for most OLED-based (bio)chemical sensors with time-resolved analysis. In the later content, we will show approaches to alleviate these issues, including the use of microcavity (μC) and UV OLEDs. Furthermore, by utilizing μLAs fabricated by the soft lithography method described earlier [31], we are able to improve the OLED-based oxygen sensing platform, as the PL signal is more than doubled in the back-detection geometry. This approach further prevents the distortion due to the background EL from affecting the detected PL signal, as demonstrated for the oxygen sensor operated in the time domain. The enhanced PL also allows the use of the OLEDs at a lower voltage, which enhances their operational lifetime.

5.2 Results and discussion

5.2.1. Enhanced OLED-based sensing utilizing CBP- and μC Alq_3-based devices

To improve the performance of the OLED-based biochemical sensors, efforts focused first on improving OLED structures and materials. To that end, the Alq_3-based OLEDs were replaced by more efficient and stable guest-host OLEDs such as coumarin-doped Alq_3 OLEDs. However, studies of such guest-host OLEDs

revealed EL spikes following a bias pulse, peaking at ~100 ns, which are associated with charge trapping on the guest molecules, and tails extending to the μs range [40,41]. Fig. 5-1(a) also elaborates this phenomenon by comparing the falling edge of the applied bias and transient EL overall intensity of the undoped and coumarin-doped Alq_3-based OLEDs. As clearly observed, with the same electrical bias pulse, the coumarin-doped OLEDs exhibit strong EL spikes and tails after the biases are turned off. This may largely relates to the charge trapping character of the coumarin dye [40,41], as manifested by the coumarin-responsible EL spectrum with only 1nm doped layer. Although the spikes appeared at a relatively short time, the transient EL tails caused by recombination of initially unpaired charges detrapped from shallow traps in the host [40,41], and by other mechanisms, such as triplet-triplet annihilation (TTA) [42], affect the PL oxygen-sensing signals [43].

Fig. 5-1(b) shows the PL decay curves of a PtOEP:PS film at 0% O_2 (Ar atmosphere) excited by an undoped and coumarin-doped pulsed Alq_3-based OLEDs. As clearly seen, the decay curve excited by the doped OLED, unlike that obtained when using the pulsed undoped device, shows two distinct regions. This latter behavior is due to the mixing of the long PL decay (~100 μs at 0% O_2) [6,44] with the short transient EL spike and tail that extends to several μs. Although at low [O_2] the signal distortion can be easily remedied by using a long pass filter or analyzing the decay curve at a longer time range (e.g., from ~2-20 μs), at high [O_2] it is hard to extract the pure sensor PL because the PtOEP decay times (a few μs) are comparable to the EL delay. In particular, the EL-related signal distortion increases at high [O_2]

where the PL intensity is low.

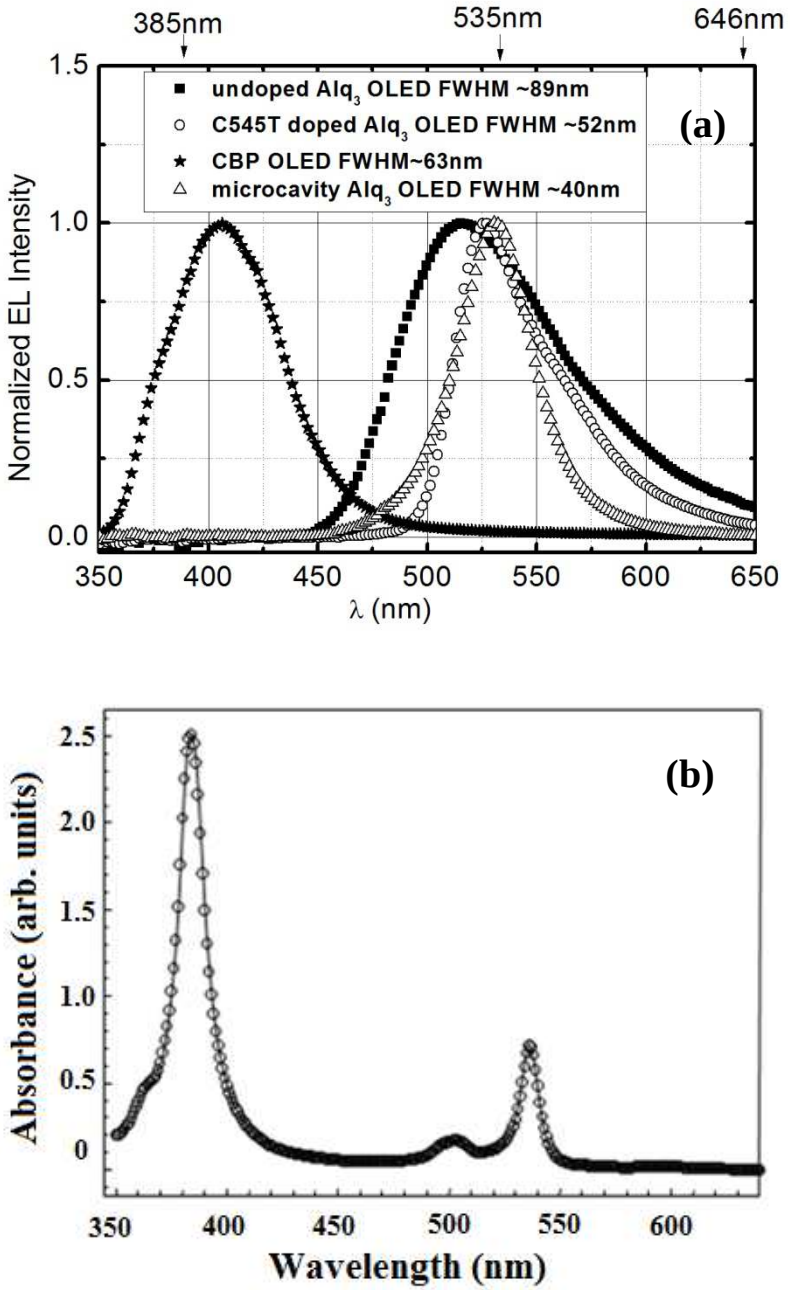

Fig. 5-2 (a) The emission spectra of various OLEDs. Undoped Alq_3 device: ITO/5 nm MoO_3/50 nm α-NPB/50 nm Alq_3/1nm LiF/~100 nm Al (squares); C545T-doped Alq_3 device: ITO/5 nm MoO_3/50 nm NPB/20 nm C545T:Alq_3/30 nm Alq_3/1nm LiF/~100 nm Al (circles); CBP device: ITO/10 nm MoO_3/40 nm CBP/35 nm BPhen/3 nm Alq_3/1nm LiF/~100 nm Al (stars); Microcavity Alq_3 device: 25 nm Ag/5 nm MoO_3/49 nm NPB/56 nm Alq_3/1 nm LiF/~100 nm Al (triangles); (b) The absorbance of PtOEP:PS films.

By blocking the excitation EL from reaching the PD, the 600 nm long-pass filter alleviates signal distortion. However, due to the broadband emission profile of these

undoped and coumarin-doped Alq_3 devices it does not eliminate it completely (Fig. 5-2(a)). Not only is the low-energy end of the EL spectrum comparable to or stronger than the PL and hence contributes to the signals (resulting in EL and PL mixing), but, additionally, part of the broadband emission is also "wasted" due to the relatively narrow PtOEP:PS absorption bands at ~385 nm and ~535 nm (Fig. 5-2(b)). As in compact designs optical filters should be ultimately excluded, alternative OLED excitation sources are required for increasing the absorption of the sensing films and reducing EL contribution to the measured signals. Moreover, by increasing the absorption at a certain EL, the OLEDs can be operated at lower excitation intensities, which boosts their operational lifetime.

With this motivation, alternative device structures such as CBP near-UV emitting OLEDs and μC Alq_3-based OLEDs were adopted. Fig. 5-2(a) shows the normalized EL spectra of the undoped and C545T-doped Alq_3-based OLEDs, the CBP-based OLED, and the μC Alq_3-based OLED. As clearly seen, the FWHM of the EL band decreases from ~89 nm to ~52 nm to ~40 nm from the undoped to the C545T-doped to the μC Alq_3 OLEDs. The peak emission of the undoped CBP OLEDs (structure: ITO / 10nm MoO_3 / 40nm CBP / 35nm BPhen / 3nm Alq_3 / 1nm LiF / ~100 nm Al) is at ~405 nm (Fig. 5-2(a)); this EL band is suitable for the PtOEP's ~385 nm absorption that is ~5 fold stronger than the ~535 nm band (Fig. 5-2(b)). Moreover, no interfering post-pulse spike is observed with this device. Hence, as shown below, in this case of CBP OLEDs the contribution of the transient EL is minimized. This is a result of (i) the stronger absorption that enhances the PL, (ii) the absence of the post-pulse spike

due to the absence of a charge-trapping dopant, (iii) the use of BPhen as a good hole-blocking layer (HBL), and (iv) the use of MoO_3 as the efficient hole injection layer (HIL) [40,41].

A similar advantage is achieved when using a μC Alq_3-based OLED with the structure 25 nm Ag / 5 nm MoO_3 / 49 nm NPB / 56 nm Alq_3 / 1nm LiF / ~100 nm Al. Here the two metal electrodes (with the very thin Ag for semi-transparency) form an optical cavity that narrows the EL band, increasing the normal-direction intensity via constructive interference. MoO_3, compared to the CuPc HIL, provides more efficient hole injection and prevents the charge from piling up at the HIL/hole transporting layer (HTL) interface. A reproducible maximum EL of ~140,000 Cd/m^2 is achieved for this device structure. This is very beneficial for OLED-based sensors, which require relatively high excitation intensities. The narrowing of the EL band leads to more efficient absorption by the sensing films and minimizes its mixing with the PL band (~646 nm [44]).

The CBP- and μC-based OLEDs excitation sources reduce the EL tail that interferes with the sensor's PL, leading to a better signal intensity and the possibility of excluding optical filters. To best demonstrate the improvement of the oxygen sensor by applying these OLEDs, we looked into the high oxygen concentration range, where the PL is the weakest and hence most affected. Fig. 5-3 compares the sensing signals and background in 100% gas-phase O_2 following the OLED pulse. The PL signal was monitored through a 600 nm long pass filter by exciting the PtOEP:PS film with the OLEDs in the back-detection geometry. By using the filter, the decay signal

is due mostly to the PL from the PtOEP:PS films. The background, i.e., the transient EL that passes through the long pass filter, was obtained through the same set-up in the absence of the sensing element.

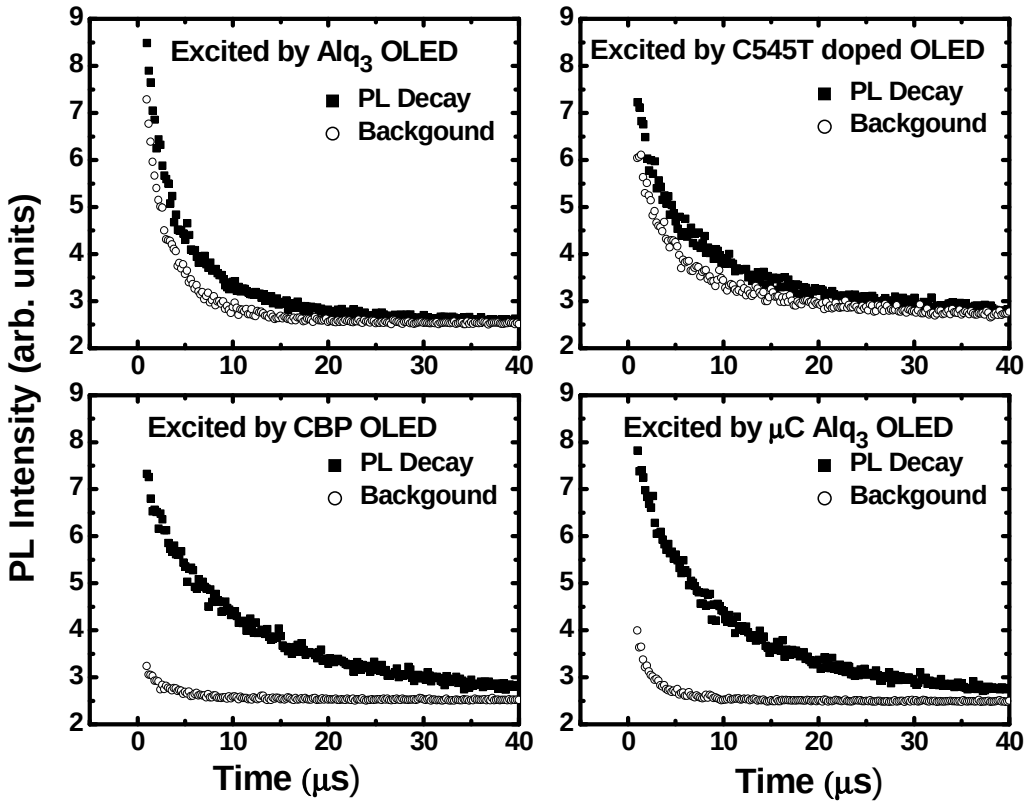

Fig. 5-3 The PL decay curve (solid squares) and background (open circles) in 100% O_2 monitored through a 600 nm long pass filter. The PL decay curve was obtained by exciting the PtOEP:PS film with various OLEDs in the back-detection geometry[6]. The background was obtained with the same setup but without the sensing element. The strongly reduced background with the CBP- and μC Alq_3-based OLEDs is clearly seen.

As clearly seen in Fig.5-3, the EL background in the doped and undoped Alq_3 OLEDs is much stronger than in the CBP- and μC Alq_3-based OLEDs. Hence, the signals obtained with the sensor film, following a bias pulse, are much more reliable with the latter OLEDs, where the contribution of the transient EL is minimized. Table

5.1 summarizes this behavior by evaluating the signals' intensity at 1 μs following the bias pulse applied on the OLED. The Table shows the ratio of the signal (*S*) with the sensor element minus the background (*B*) to *B*, i.e., (*S* – *B*)/*B*. As seen, the ratio ~ 0.2 is low for the often-used doped and undoped Alq_3-based OLED. It increases significantly for the CBP- and μC Alq_3-based OLEDs, to ~1.3 and 1.0, respectively. Thus, the use of the latter provides more reliable analysis when obtaining the PL decay time from decay curves following a pulsed OLED.

Table 5.1: the PL: EL signal ratio for a PtOEP:PS sensor film in 100% gas-phase O_2 at 1 μs following the EL pulse for various OLEDs.

Device	Undoped Alq_3	C545T:Alq_3	CBP	Microcavity Alq_3
(*S*-*B*)/*B* @ 1 μs	0.16	0.20	1.26	0.96

To further demonstrate the improved performance of the oxygen-based sensors excited by CBP- and μC Alq_3-based OLEDs, the normalized decay signals obtained with and without the 600 nm long pass filter for 100% Ar, Air, and 100% O_2 are shown on a semi-log scale in Fig. 5.4. Due to the decay of the OLED EL, the initial parts of the signals are excluded for reliable analysis. A linear behavior in the semi-log plot obviously demonstrates a simple single-exponential decay time in which case the contribution of the transient EL to the measured signal is minimal. The signals from all the devices with the 600 nm long-pass filter fit a single-exponential decay at zero oxygen concentration (Fig. 5.4 (a)). The EL:PL mixing at low oxygen levels is small due to the long PL decay time (~100 μs in 100% Ar [1,6,44]; see Table II & III) and the minimal contribution of the EL tail that decays in ~3 μs. As the oxygen concentrations increase, the decay curves obtained using undoped and C545T-doped Alq_3 OLEDs deviate from a single exponential while those from CBP

and μC Alq_3 OLEDs remain nearly exponential across the whole O_2 range (with single exponential regression coefficients R^2 = 0.997,0.998, and 0.989 for 100% Ar, Air, and 100% O_2 respectively).

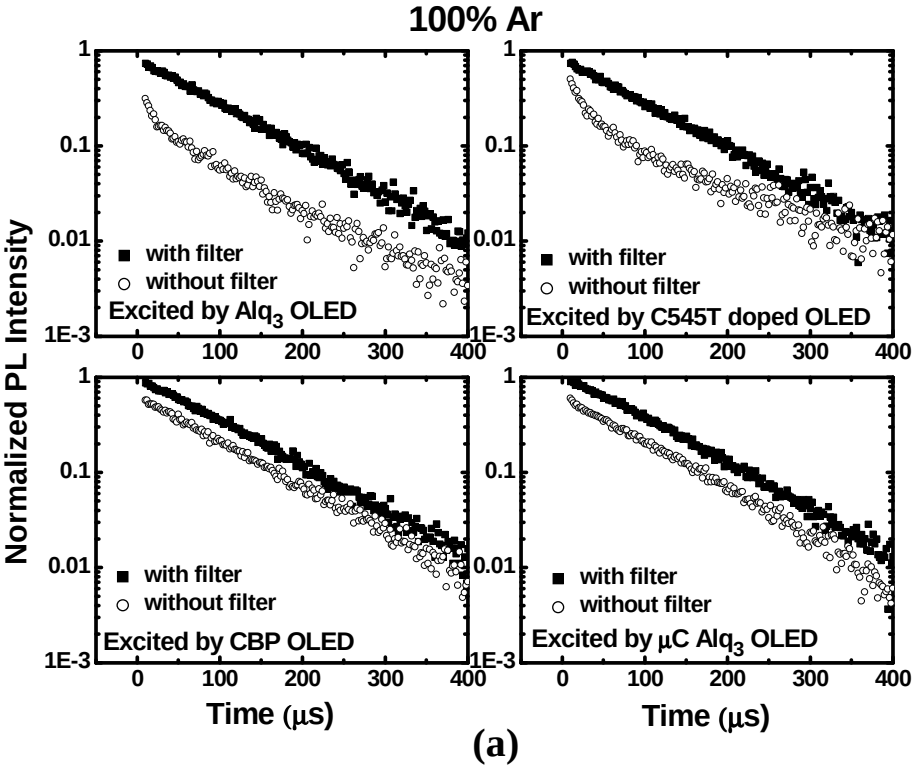

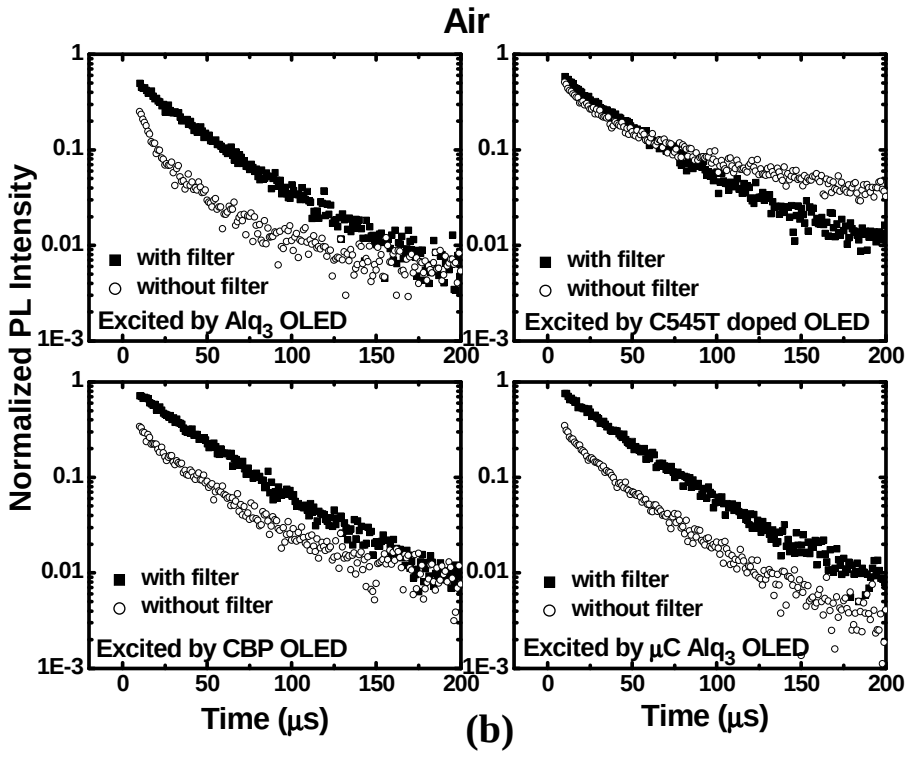

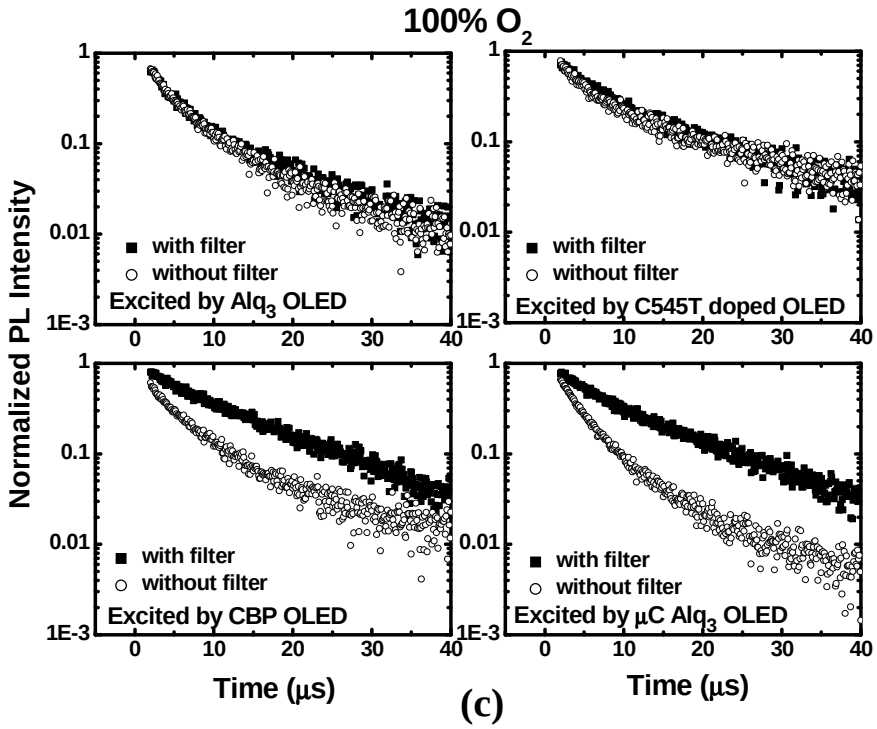

Fig. 5-4 The normalized PL decay curves of the PtOEP:PS films excited by various OLEDs in (a) 100% Ar (b) Air (21% O_2) and (c) 100% O_2 with (solid squares) and without (open circles) the 600 nm long pass filter. Note the semilog scale.

Without the 600 nm long-pass filter, the decay curves are distorted by the transient EL from undoped and C545T-doped Alq_3 OLEDs for all O_2 concentrations. The situation is different for the CBP- and μC Alq_3-based OLEDs, as seen in the bottom panels of Fig. 5-4(a)-(c). In 100% Ar and air, the plots are close to linear even in the absence of the optical filter. This is important because 0%-21% O_2 is the range of interest in most applications, including for dissolved O_2 (DO) and for DO-based sensors for bioanalytes such as glucose, lactate, and alcohol [6-10]. In 100% O_2, the optical filter is needed for reliable analysis, however, the EL contribution (as observed in the absence of the 600 nm filter) is significantly lower than with undoped and C545T-doped Alq_3 OLEDs. Additionally, the decay curves at 100% O_2 excited by the undoped and C545T-doped Alq_3 OLED with and without the filter overlap, proving

that even with the filter the decay curve is mainly that of the incompletely blocked EL tail.

Table 5.2 summarizes the single exponential-fitted decay times for the four OLEDs, with and without the long-pass filter, in different atmospheres. The similar decay times obtained for 0% and 21% O_2 using CBP- and μC Alq_3-based OLEDs prove that they can provide more efficient excitation and less EL contribution to the O_2 sensing signals. We note that the single exponential fit both with and without the optical filter worsens at 100% O_2. This deviation is probably due to the low signal intensity caused by strong O_2 quenching of the phosphorescence and the microheterogeneity of the sensing films, which results in a distribution of O_2/excited PtOEP collision rates. Earlier studies have shown that the stretched exponential fit was more suitable at high oxygen concentrations due to this distribution of collision rates [10]. However, as we focus only on the signal improvement induced by different OLED architectures, this detailed analysis was not applied in this work.

Table 5.2: the single exponential-fitted decay times for the four OLEDs, with and without the 600 nm long-pass filter, in different atmospheres.

With the long-pass filter (μs)			
	100% O_2	Air	100% Ar
Alq_3-based OLED	4.0	26.1	89.0
C545T-doped Alq_3 OLED	6.6	28.5	86.7
CBP-based OLED	8.5	33.7	91.2
μC Alq_3 OLED	8.7	33.1	103.3
Without the long-pass filter (μs)			
Alq_3-based OLED		16.4	60.5
C545T-doped Alq_3 OLED		40.1	46.3
CBP-based OLED		30.8	90.2
μC Alq_3 OLED		30.0	92.6

5.2.2. μLA-induced signal improvement

The preceding section demonstrated methods of fabricating improved OLEDs for reliable (bio)chemical sensing. Next we describe the use of a *μLA*, typically used for enhancing the OLED's EL, for enhancing the PL that reaches the PD.

For a conventional OLED fabricated on ITO-coated glass, only ~20% of the emission generated internally is extracted out of the device in the forward direction [28]. Most of the rest is trapped in the organic/ITO and glass layers due to total internal reflection at the ITO/glass and glass/air interfaces. Many studies have focused on improving the outcoupling of the OLEDs [28-32]. The μLA, which is easy to fabricate and integrate with OLED pixel arrays, can improve the performance of the OLED-based sensing platform without affecting its compactness. Such a μLA is made from materials that have refractive indices similar to that of the glass substrate, minimizing the internal reflection between the glass and the μLA material. In principle, a PS-based sensor film (refractive index ~1.55, similar to that of glass), deposited directly on the back of the OLED's glass substrate, or on a separate glass substrate with perfect contact with the OLED's substrate, should also minimize the internal reflection between the OLEDs and the sensing film. However, some of the sensing film's PL will undergo internal reflection at the glass/air (in the back detection geometry) or the PS/air (in the front detection geometry) [6], reducing the PL that reaches the PD. Note also that in the back-detection geometry the OLED pixels partially block the PL from reaching the PD.

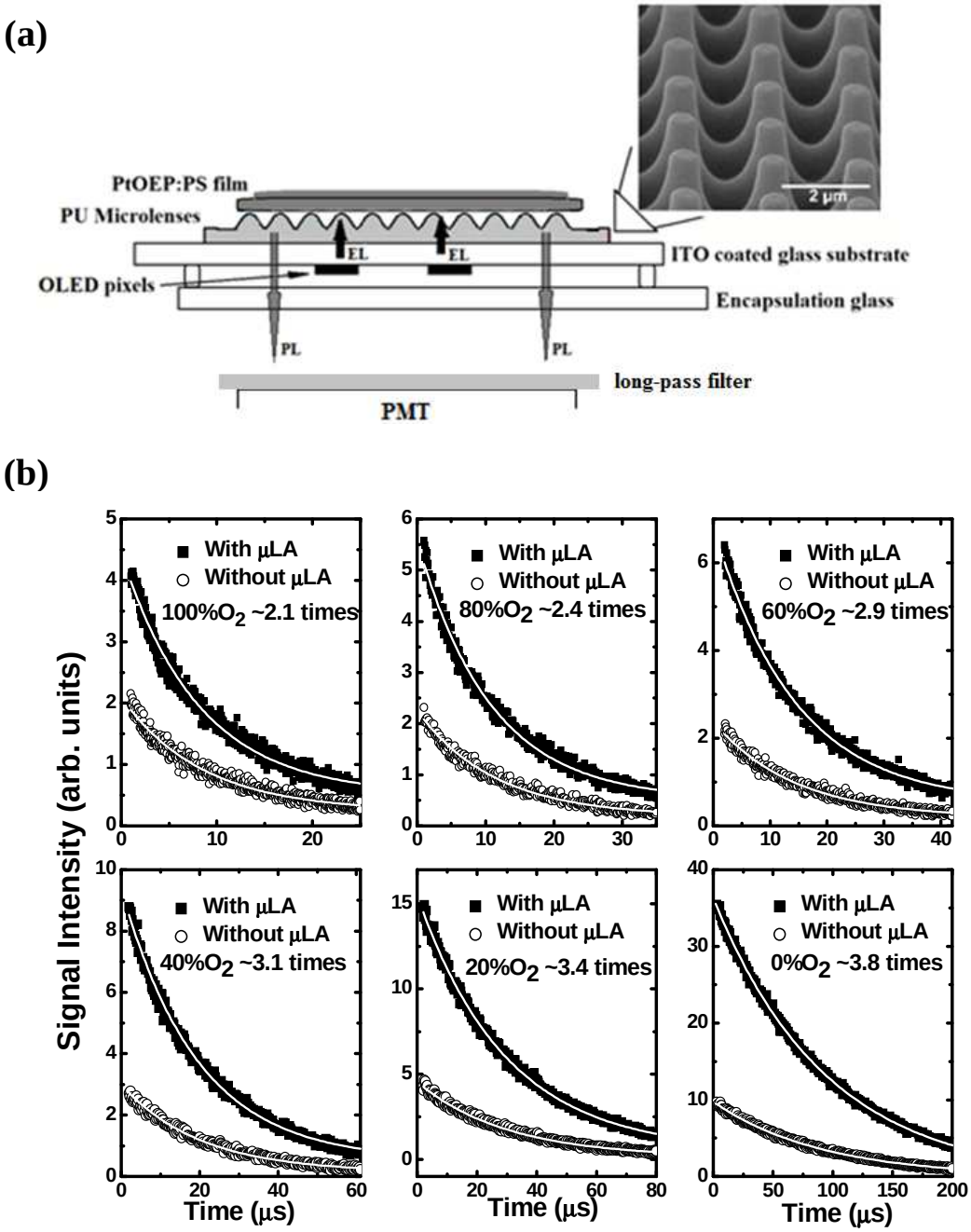

Fig. 5-5 (a) The set-up of the compact oxygen sensor probe: PtOEP:PS film excited by the CBP OLED structurally integrated with the microlens array. Note that the drawing is not to scale. (b) The sensor signal enhancement obtained by using a CBP OLED/microlens array under various O_2 environments (solid squares) and the reference decay curves without the microlenses (open circles); the white lines are the single exponential fitting.

Fig. 5-5(a) shows the compact setup of the OLED-based oxygen sensing probe with a μLA, and a SEM image of that PU 2 μm-pitch μLA. It has been confirmed that

this device design enhances EL outcoupling in the forward direction by ~100% [31]. Fig. 5-5(b) shows the signal improvement of the oxygen sensor excited by a CBP UV OLED equipped with such a μLA. The signal enhancement factor in the back-detection geometry ranges from ~2.1 to ~3.8 across the 0 – 100% oxygen concentration range. We attribute this enhancement to strong scattering/directing of the PL toward the PD by the μLA, possibly also the PL fraction that is otherwise partially blocked by the OLED pixels. The observed dependence of the enhancement factor on [O_2] is currently not clear; it is not associated with the response of the photomultiptier tube (PMT), as it was operated in the linear region. Importantly, as summarized in Table 5.3, while the integrated μLA enhances the detected signal, it has practically no effect on the τ values calculated from the decay curves.

Table 5.3: The single exponential fitted decay times (μs) for the gas-phase oxygen sensor excited by a CBP OLED with and without the μLA in different atmospheres.

	0% O_2	20% O_2	40% O_2	60% O_2	80% O_2	100%O_2
with μLA	94.5	29.6	19.4	14.2	10.7	8.12
without μLA	91.2	30.0	20.1	14.2	11.4	8.50

5.3 Conclusion

In summary, issues related to the pulsed OLED-based luminescent sensing platform and approaches to alleviate them are presented. When monitoring O_2 (and other bioanalytes whose sensing is based on monitoring O_2) in PL-based sensors utilizing undoped and C545T-doped Alq_3-based OLEDs, in particular at high O_2 levels, the decay curves contain contributions from the post-pulse transient EL. The situation improves as [O_2] decreases. However, optical filters are needed, reducing device compactness. The C545T-doped Alq_3 and other similar doped small-molecule OLEDs are especially of concern due to their slow-decaying post-pulse transient EL.

The above-mentioned issues are alleviated when using CBP- or microcavity Alq_3-based OLEDs as the excitation source, where (in addition to the absence of a post-pulse spike) the absorption of the sensing film is significantly more efficient and the interference from the long-wavelength tail of typical EL bands is minimized, respectively. Additionally, uniform 2 μm-pitch μLAs made from polyurethane (PU), attached to the backside of a CBP OLED, significantly enhance the detected signal intensity. This enhancement is due to directing the otherwise isotropic and partially blocked PL toward the PD. Such approaches enable the use of compact OLED-based oxygen and related biosensing probes driven at a relatively low excitation power so that the lifetime of the devices is prolonged. These improved excitation sources will assist in further developing the thin OLED-based sensing platform in conjunction with microfluidic architectures for reliable data analysis.

5.4 Experimental

5.4.1. Materials

OLEDs: ~15 Ω/square ITO-coated glass was obtained from Colorado Concept Coating, LLC., and N,N’-diphenyl-N,N’-bis(1-naphthylphenyl)-1,1’-biphenyl-4,4’ -diamine (α-NPB), coumarin 545T (C545T) and tris(8-hydroxyquinolinato) Al (Alq_3) were obtained from H. W. Sands. 4,7-diphenyl-1,10-phenanthroline (BPhen), copper phthalocyanine (CuPc) and LiF were obtained from Sigma-Aldrich. 4,4'-Bis(carbazol-9-yl)biphenyl (CBP) was obtained from Luminescence Technology. MoO_3 is purchased from Strem Chemicals. Silver dropshots were obtained from Johnson Matthey.

Sensing elements: PtOEP was obtained from H. W. Sands, PS, molecular weight 45,000, from Sigma-Aldrich, and toluene from Fisher Scientific.

5.4.2. Procedures

μLA fabrication [31]: For fabrication of the μLA, a two-beam laser holography was applied to pattern a 2-D interference structure on a photoresist that coated a glass substrate. A first exposure of the photoresist created a 1-D pattern; the desired 2-D pattern was achieved by a second exposure after rotating the sample by 90°. The photoresist was then developed and briefly heated to generate a spherical array structure. Polydimethylsiloxane (PDMS) was poured directly onto the photoresist, cured, and peeled off, thus becoming the inverse-pattern stamp for the μLA. A tiny drop of UV curable PU was applied on the blank side of an ITO-coated glass substrate, which was subsequently used for OLED fabrication, and the PDMS mold, with the inverse μLA pattern, was gently pressed against it. Any excess of PU was easily removed. After the PU was cured in a UV chamber, the PDMS mold was lifted off and the μLA pattern was formed on the PU. OLED pixels, with or without an underlying μLA, were then fabricated on the ITO.

OLED fabrication: OLED pixels were fabricated on the ~150 nm thick ITO layer; the ITO was treated as previously described [45]. It was then etched to generate stripes that served as the anode. Following thermal evaporation of MoO_3 (a hole injection layer), the organic layers and LiF (an electron injection layer) were deposited. Finally, the Al cathode was thermally-evaporated via a mask to generate stripes similar to the ITO ones, but perpendicular to them. The OLED pixels were

defined by the overlapping ITO/Al regions.

Fabrication of μC OLEDs started with deposition of 25 nm Ag on a glass substrate. The MoO_3 and organic layers were then deposited and capped with LiF and Al as the cathode. 2 mm ×2 mm^2 individually addressable OLED pixels were generated with the total thickness of the devices, excluding the substrate and the encapsulating cover glass, less than 0.3 μm. The encapsulating cover glass was glued using Torr Seal epoxy to prevent water and O_2 exposure. We note that OLEDs encapsulated in this simple manner can be used successfully for months when operated in a pulsed mode and monitoring the analytes' effect on the PL decay times, as small changes in the OLED brightness over time do not affect the measured PL decay time.

Sensing elements preparation: The sensing films were prepared by drop casting 50-60 μL of toluene solution, which contained 1 mg/mL PtOEP and ~40 mg/mL PS on cleaned glass slides. The glass slides were cleaned by ultrasonication in acetone for 5 min followed by ultrasonication in isopropanol, blow-drying in N_2, and 5 min UV ozone treatment. The solutions were spread on the slides to generate typically 7-8 μm thick films. The resulting films were allowed to dry in the dark at ambient temperature for at least 24 hours. We note that the detection sensitivity is strongly dependent on the nature of the sensing film; the sensitivity increases when the oxygen permeability increases. The PS sensing films used in this study are moderately permeable to oxygen.

Monitoring the PL decay time: PL decay curves at different levels of gas phase O_2 were obtained by applying 100 μs OLED excitation pulses. To simplify the analysis

τ was extracted from the decay curves using a single exponential fit with background (i.e., offset).

Instrumentation: OLED arrays were fabricated by thermal vacuum evaporation of the organic layers in a chamber (background pressure ~1-2×10^{-6} Torr) installed in an Ar-filled glove box (typical O_2 levels <10 ppm). The OLEDs were driven by an Avtech AV-1011B pulse-generator.

The PL was monitored with a Hamamatsu R6060 PMT, typically in the "back-detection" geometry, collecting the PL passing through the gaps between the OLED pixels that were used for excitation [6-10,24,25]. We note that the back detection geometry results in a more compact setup.

Various levels of gas-phase O_2 were generated by flowing oxygen/argon mixtures. Mixing was achieved by means of mass flow controllers, where the flow rates of the oxygen and argon varied, while maintaining a constant total flow rate, thus generating varying oxygen partial pressures.

Acknowledgements

Research supported by the U.S. Department of Energy, Basic Energy Sciences, Materials Sciences and Engineering Division under Contract No. DE-AC 02-07CH11358.

References

1. *Organic Electronics in Sensors and Biotechnology* (Eds: R. Shinar, J. Shinar, McGraw Hill, NY, 2009).
2. K. P. R. Nilsson, P. Hammarström, F. Ahlgren, A. Herland, E. A. Schnell, M.

Lindgren, G. T. Westermark, O. Inganäs, Chembiochem. **7**, 2096 (2006).

3. L. Robinson, A. Hentzell, N. D. Robinson, J. Isaksson, M. Berggren, Lab on a Chip **6**, 1277 (2006).
4. J. Isaksson, P. Kjäll, D. Nilsson, N. D. Robinson, M. Berggren, A. Richter-Dahlfors, Nat. Mater. **6**, 673 (2007).
5. L. Torsi, A. Dodabalapur, Anal. Chem. **77**, 390A (2005).
6. J. Shinar, R. Shinar, J. Phys. D: Appl. Phys. **41**, 133001 (2008).
7. R. Shinar, Z. Zhou, B. Choudhury, J. Shinar, Anal. Chim. Acta **569**, 190 (2006).
8. Z. Zhou, R. Shinar, A. J. Allison, J. Shinar, Adv. Funct. Mater. **17**, 3530 (2007).
9. Y. Cai, R. Shinar, Z. Zhou, J. Shinar, Sensors and Actuators B: Chem **134**, 727 (2008).
10. Y. Cai, A. Smith, J. Shinar, R. Shinar, Sensors and Actuators B: Chem **146**, 14 (2010).
11. S. Sax, E. Fisslthaler, S. Kappaun, C. Konrad, K. Waich, T. Mayr, C. Slugovc, I. Klimant, E. J. W. List, Adv. Mater. **21**, 3484 (2009).
12. E. Kraker, B. Lamprecht, A. Haase, G. Jakopic, T. Abel, C. Konrad, S. Kostler, M. Tscherner, B. Stadlober, T. Mayr, in Organic Semiconductors in Sensors and Bioelectronics III, (Eds: R. Shinar and I. Kymissis), Proc. SPIE **7779**, 777904 (2010).
13. E. Kraker, A. Haase, B. Lamprecht, G. Jakopic, C. Konrad, S. Köstler, Appl. Phys. Lett. **92**, 033302 (2008).

14. R.B.A. Sharpe, P.A. Rensing, G.T. van Heck, B.A.M. Allard, M.M. Koeste, N.N.M. Meulendijks, P.G.M. Kruijt, M.W.W.J. Tijdink, R.M. de Zwart, S.J.J.F. van Veen, H.F.M. Schoo, in Organic-based Chemical and Biological Sensors, (Eds: R. Shinar and G. Malliaras), Proc. SPIE **6659**, 665908 (2007).
15. M. Koeste, P. Rensing, G. van Heck, R. Sharpe, B. Allard, F. Wieringa, P. Kruijt, N. Meulendijks, H. Jansen, H. Schoo, in Organic Field-Effect Transistors VII and Organic Semiconductors in Sensors and Bioelectronics, (Eds: Z. Bao, I. McCulloch, R. Shinar and G. Malliaras), Proc. SPIE **7054**, 70541I (2008).
16. E. L. Ratcliff, P. A. Veneman, A. Simmonds, B. Zacher, D. Huebner, S. S. Saavedra, N. R. Armstrong, Anal. Chem. **82**, 2734 (2010).
17. B. Yao, G. Luo, L. Wang, Y. Gao, G. Lei, K. Ren, L. Chen, Y. Wang, Y, Hu, Y. Qiu, Lab on a Chip **5**, 1041 (2005).
18. J. B. Edel, N. P. Beard, O. Hofmann, J. C. deMello, D. D. C. Bradley, A. J. deMello, Lab on a Chip **4**,136 (2004).
19. M. Vasilopoulou, D. G. Georgiadou, L. C. Palilis, A. Botsialas, P. S. Petrou, S. E. Kakabakos, P. Argitis, Microelectronic Engineering **86**, 1511 (2009).
20. J. Frischeisen, C. Mayr, N. A. Reinke1, S. Nowy, W. Brütting, Optics Express **16**, 18426 (2008).
21. S. Devabhaktuni, S. Prasad, Journal of Nanoscience and Nanotechnology **9**, 6299 (2009).
22. H. Yamamoto, J. Wilkinson, J.P. Long, K. Bussman, J.A. Christodoulides, Z.H. Kafafi, Nano Lett. **5**, 2485 (2005).

23. S. Vengasandra, Y. Cai, D. Grewell, J. Shinar, R. Shinar, Lab On a Chip **10**, 1051 (2010).

24. R. Shinar, D. Ghosh, B. Choudhury, M. Noack, V.L. Dalal, J. Shinar, J. Non Cryst. Solids **352**, 1995 (2006).

25. K. S. Nalwa, Y. Cai, A. L. Thoeming, J. Shinar, R. Shinar, S. Chaudhary, Adv. Mater. **22**, 4157 (2010).

26. E. J. Cho, Z. Tao, E. C. Tehan, F. V. Bright, Anal. Chem. **74**, 6177 (2002).

27. H. Frebel, G.-C. Chemnitius, K. Cammann, R. Kakerow, M. Rospert, W. Mokwa, Sensors and Actuators B: Chem. **43**, 87 (1997).

28. Y. Sun, S. R. Forrest, Nature Photonics **2**, 483 (2008).

29. P. A. Hobson, S. Wedge, J. A. E. Wasey, I. Sage, W. L. Barnes, Adv. Mater. **14**, 1393 (2002).

30. W. H. Koo, S. M. Jeong, F. Araoka, K. Ishikawa, S. Nishimura, T. Toyooka, H. Takezoe, Nature Photonics **4**, 222 (2010).

31. J.-M Park, Z. Gan, W.Y. Leung, R. Liu, Y. Zhou, K. Constant, J. Shinar, R. Shinar, K.-M. Ho, Optics Express **19**, A786 (2011).

32. S. Reineke, F. Lindner, G. Schwartz, N. Seidler, K. Walzer, B. Lüssem, K. Leo, Nature **459**, 234 (2009).

33. I. Bergman, Nature **218**, 396 (1968).

34. O.S. Wolfbeis, Anal. Chem. **80**, 4269 (2008).

35. W. Xu, R.C. McDonough, B. Langsdorf, J.N. Demas, B.A. DeGraff, Anal. Chem. **66**, 4133 (1994).

36. J.N. Demas, B.A. DeGraff, W. Xu, Anal. Chem. **67**, 1377 (1995).

37. S. Draxler, M.E. Lippitsch, I. Klimant, H. Kraus, O.S. Wolfbeis, J. Phys. Chem. **99**, 3162 (1995).

38. S. Draxler and M.E. Lippitsch, Anal. Chem. **68**, 753 (1996).

39. Y. Tang, E.C. Tehan, Z. Tao, and F.V. Bright, Anal. Chem. **75**, 2407 (2003).

40. Z. Gan, R. Liu, R. Shinar, J. Shinar, Appl. Phys. Lett. **97**, 113301 (2010).

41. R. Liu, Z. Gan, R. Shinar, J. Shinar, Phys. Rev. B **83**, 245302 (2011).

42. Z. D. Popovic, H. Aziz, J. Appl. Phys. **98**, 013510 (2005).

43. R. Liu, Z. Gan, Y. Cai, A. Smith, J. Shinar, R. Shinar, in Organic Semiconductors in Sensors and Bioelectronics II, (Eds: R. Shinar and G. Malliaras), Proc. SPIE **7418**, 74180D (2009).

44. Y. Amao, Microchim. Acta **143**, 1 (2003).

45. V. Savvate'ev, Z. Chen-Esterlit, J. W. Aylott, B. Choudhury, C.-H. Kim, L. Zou, J. H. Friedl, R. Shinar, J. Shinar, R. Kopelman, Appl. Phys. Lett. **81**, 4652 (2002).

Chapter 6. Multiple Approaches for Enhancing All-Organic Electronics PL Sensors: Simultaneous Oxygen and pH Monitoring

Modified from a paper submitted to Advanced Functional Materials

Rui Liu, Teng Xiao, Weipan Cui, Joseph Shinar, Ruth Shinar

Abstract

Key issues in using organic light emitting diodes (OLEDs) as excitation sources in structurally integrated photoluminescence (PL)-based sensors are the low forward light outcoupling as well as the OLEDs' broad electroluminescence (EL) bands and long tails. The outcoupling issue limits the detection sensitivity and the EL characteristics interfere with the analyte-sensitive PL, leading to a background signal that reduces the detection sensitivity and dynamic range. In particular, these issues interfere with designing compact sensors, potentially miniaturizable, that are devoid of optical filters and couplers. We address these shortcomings by introducing easy-to-employ multiple approaches for outcoupling improvement, PL signal enhancement and background EL reduction leading to novel, compact all-organic device architectures demonstrated for simultaneous monitoring of oxygen and pH. The sensor comprises simply-fabricated, directionally-emitting multicolor microcavity OLED excitation and an organic photodetector (OPD) with a more selective spectral response. Additionally, the detection sensitivity and PL intensity for oxygen are enhanced by using polystyrene (PS): polyethylene glycol (PEG) blends as the sensing film matrix. The microporous structure of these blended films, with PEG decorating PS pores, serves a dual purpose. It results in light scattering that reduces

the waveguided EL in the substrate and it increases the PL directed toward the OPD. The multiple functional structures with the multicolor microcavity OLED pixels/microporous scattering films/OPDs enable generation of enhanced individually addressable sensor arrays, devoid of interfering issues, for O_2 and pH as well as for other analytes.

6.1 Introduction

The fast-growing development of organic electronic materials and devices has enhanced their application in flat-panel displays, solid-state lighting, solar cells and photodetectors, as well as (bio)chemical and medical sensing [1-5]. Among these applications, organic-based luminescent sensors have demonstrated high detection sensitivities with advantages such as potential low cost and ease of fabrication and integration with sensing films, thin-film photodetectors (PDs), and microfluidic structures [3-12]. Recent progress in developing highly-efficient organic light-emitting diodes (OLEDs) [13-15] and organic photovoltaic (OPV) devices [16-18] further advance all-organic electronics photoluminescence (PL)-based sensors [8,11,12].

The all-organic PL-based sensing platform comprises OLED pixels, organic photodetectors (OPDs) and thin sensing elements, all fabricated on simple substrates such as glass or plastic. In integrated structures, the OLEDs and sensing films were often fabricated on two back-to-back attached glass slides [4,11,19]. Several recent studies evaluated the properties of OLED-based sensors and demonstrated their feasibility for monitoring (bio)chemical analytes such as oxygen, carbon dioxide,

glucose, lactate, pH, and algal [5-12].

The electroluminescence (EL) spectra of OLEDs are typically broad with long tails, and may therefore partially overlap the analyte-sensitive PL of the sensing elements. Hence, separation of the excitation EL and PL signals is required, while maintaining sufficient signal intensities for sensitive detection and broad dynamic range. To address this issue optical filters or polarizers are often used [6,9,11,12]. In other reports, the OPDs were spatially separated from the excitation light and substrate waveguided PL was detected by using additional coupling structures, such as gratings and scattering films [7,10]. However, to realize compact, eventually miniaturized, and cost-effective sensors, enhancing the signal to noise ratio with simpler integrated structures, materials and approaches resulting in sensors devoid of optical filters, fibers, mirrors and other couplers is needed.

Aiming for such compact and simple architecture, we earlier reported on oxygen sensors, where the OLED and the PD (photomultiplier tube or Si photodiode) were positioned in a back-detection geometry, where the PD is behind the OLED pixel array, collecting the PL between the OLED pixels. This design enables easier access of the sensing element to the analyte. Also, using this approach the distortion of the signals due to the interfering electroluminescence (EL) background is reduced, with the excitation EL directed opposite to the detected PL [4,11,19].

As is well known, the detection of O_2 using optical sensors is based on monitoring O_2-induced changes in the PL intensity (I) or decay time (τ) of an oxygen sensitive dye, such as Pt octaethylporphyrine (PtOEP), embedded in a polymeric matrix, such

as polystyrene (PS). Analysis is based on the Stern-Volmer (SV) equation [3,4,20].

$$I_0/I = \tau_0/\tau = 1 + K_{SV}[O_2] \qquad (6.1)$$

where I_0 and τ_0 are the unquenched values, K_{SV} is the SV constant, and $[O_2]$ is the O_2 level.

In this work multi-functional films and structures were developed. The O_2 sensing films were cast directly on the back of the OLED substrates. The sensing films were prepared from blends of high molecular weight (M_w) PS and low M_w polyethylene glycol (PEG). The resulting microporous films improved both the oxygen permeability and signal intensity with no dye leaching. Moreover, these index-matching films in direct contact with the OLED substrate enabled partially overcoming the forward EL outcoupling issues in OLEDs caused by total internal reflection at the glass/air interface [21]. Additionally, the micropores that were formed in the blended PS:PEG films, with PEG decorating voids in the PS, scatter the PL, enhancing the fraction that reaches the PD. As the excitation light is also scattered by the PS:PEG microstructure, an OPD with a more specific spectral response to the longer-wavelength PL was fabricated.

To further improve the sensor performance by reducing the background light, narrower-band microcavity (μC) OLEDs, with emission concentrated mostly in the normal direction, were used. A simple method to fabricate multicolor μC OLEDs was recently developed [22]. In this method, a thin layer of MoO_3 was utilized as both the hole injection layer and the optical spacer. Varying the thickness of this layer in a combinatorial deposition approach led to multicolor OLED pixels on a compact area.

Hence, this approach enables construction of compact multiple-sensor arrays with different excitation wavelength suitable for different fluorophores.

The pH detection is based on the change in the fluorescence of the pH-sensitive dye fluorescein. Fluorescein and many of its derivatives exhibit multiple pH-dependent ionic equilibria. Acidification of the fluorescein dianion protonates first the phenol to yield the fluorescein monoanion; this is followed by the formation of carboxylic acid to produce the neutral species. Further acidification generates a fluorescein cation. As only the monoanion and dianion are fluorescent with different quantum yields, the PL of such materials varies with the solution pH [23].

A dual sensing platform demonstrating the utility of the multicolor microcavity OLED array in an all-organic structure with multi-function films was designed for monitoring O_2 and pH by evaluating changes in both the PL intensity and decay time. These analytes are key in, e.g., agricultural, environmental and biological processes monitoring [24-26], and therefore a practical and compact device is very desirable.

6.2 Results and Discussion

6.2.1. Toward all-organic O_2 sensor

The back-detection geometry reduces the distortion of the PL intensity signal stemming from the interfering EL background by directing the excitation light forward, opposite to the photodetector (PD) that is positioned behind the OLED pixels [4,11]. Fig. 6-1(a) shows the original design. As seen, the disadvantage in this design is that the PL is partially blocked by the nontransparent OLED cathode. Scattering structures such as microlens arrays, fabricated by soft lithography, were previously

used to enhance the detected PL intensity by scattering/directing the signal toward the PD, away from the blocking OLED pixel [19]. However, such a method involves a complex process, including UV curing, which makes it difficult to integrate the sensing elements with the scattering structure. Sensing films on separate substrates reduce the compactness of the devices and weaken the advantage of the back-detection design by leading to multiple reflections at the substrate surfaces, which increases the background light reaching the PD.

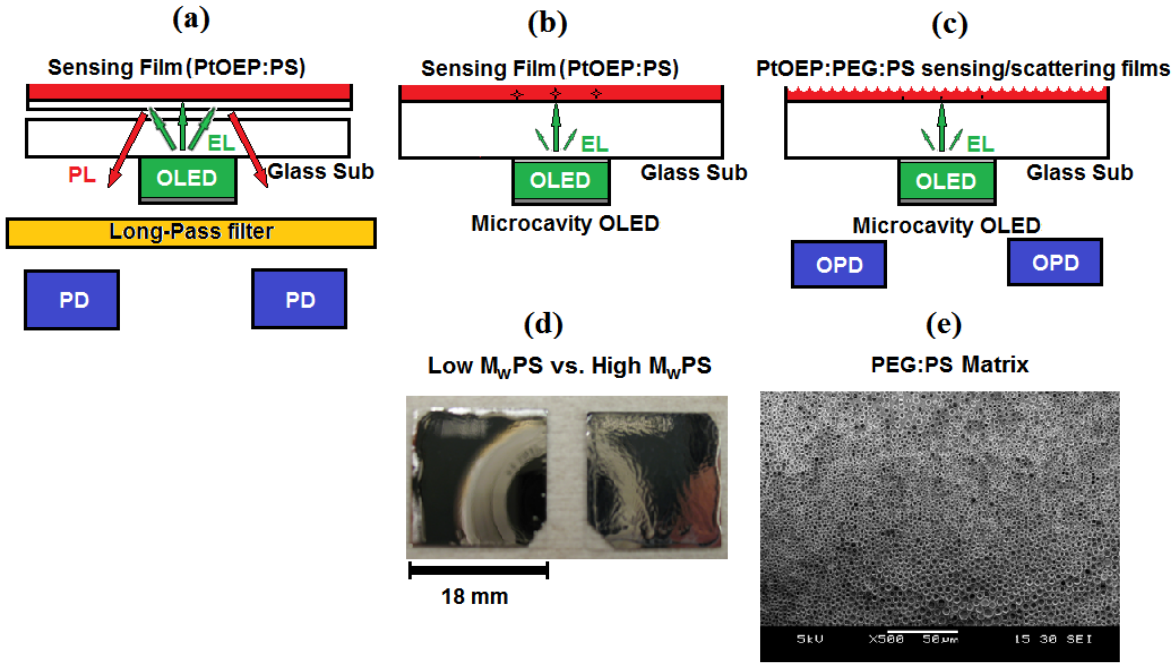

Fig. 6-1 Evolution of the back-detection organic-based O_2 sensor: (a) Original set-up. (b) Sensing film with more permeable high M_w PS matrix directly dropcast on the back of the OLED substrate excited by a μC OLED with a significantly narrower emission band at the absorption band of PtOEP. (c) Modified scattering matrix of blended PS:PEG. (d) Image comparing the macroscopic morphology of the smoother low M_w PS (M_w ~ 45,000) film and the rougher high M_w PS (M_w ~ 280,000) film dropcast on 18×18 mm^2 glass substrates. A 100 nm Al layer was deposited on the dried films. (e) SEM image of the high M_w PS:PEG film with a 4:1 weight ratio.

Figs. 6-1(a)-(c) demonstrate the evolution of the OLED-based O_2 sensor from the original set-up shown in (a), where two glass slides were attached back-to-back and a long-pass filter was placed in front of the PD. Due to light absorption by the Al

electrode and waveguided modes within the ITO+organic layers and within the glass substrate, only ~20% of the light generated within the OLED is forward outcoupled and hence usable for excitation [27]. In Fig. 6-1(b) the regular OLED is replaced by a μC OLED [22]. The concentrated narrow emission from the μC device (full width at half maximum FWHM ~30 nm) reduces the fraction of scattered background EL and provides more efficient excitation as reported earlier [19]. The figure also shows the more compact design where the sensing element is fabricated by dropcasting toluene solution containing 1:40 mg/mL PtOEP:PS directly on the back of the OLED's substrate. The index matching of the PS film ($n \approx 1.6$) disrupts the total internal reflection at the glass/air interface, which enhances the intensity of the excitation light that reaches the PtOEP dye. Furthermore, different from earlier reported work, higher M_w PS is used as the matrix material. It was observed that the high M_w PS improves the sensor's performance. The longer polymer chains apparently form films that are more permeable to O_2 and hence improve the detection sensitivity. Fig. 6-1(d) shows photographs of PS film/glass, with different M_w PS, coated with Al to illustrate the surface roughness. As seen, the blurred reflection from the Al/high M_w PS (M_w ~ 280,000) film indicates a rougher structure than that of the Al/low M_w PS (M_w ~ 45,000) film.

In order to prevent blocking of the PtOEP PL by the opaque cathode of the OLED, in Fig. 6-1(c) we modified the sensing film by mixing the PS with PEG to form scattering microstructures. During the room-temperature solvent (toluene) evaporation of the mixed solution, PS and PEG phase separate, forming initially PEG-rich droplets.

Upon continued evaporation, the PEG droplets shrink to form PEG-coated micropores ranging in size from ~1.5 μm to ~5 μm in diameter, as shown in the SEM image of Fig.6-1(e) [21].

For comparison, three different sensor films were tested utilizing the combined above-mentioned modifications. We first compared films with 1 mg/mL PtOEP embedded in 40 mg/mL low M_w PS (M_w ~ 45,000) or in 40 mg/mL high M_w PS (M_w ~ 280,000); these films were labeled L40 and H40, respectively. As the high M_w PS films showed improved oxygen permeability, we blended it at a 40:10 mg/mL high M_w PS:PEG (M_w ~ 1,000) ratio. The latter film was marked H40G10. The sensors were operated in the time domain using a green μC OLED (40 nm Ag/7 nm MoO_3/49 nm N,N'-diphenyl-N,N'-bis(1-naphthylphenyl)-1,1'-biphenyl-4,4'-diamine (α-NPB)/61 nm tris(8-hydroxyquinolinato) Al (Alq_3)/1nm LiF/100 nm Al) with a 100 μs excitation pulse. The PL decay curve was then analyzed; comparable single exponential PL decay times (τ) of ~93-97 μs were obtained for the sensing films in absence of O_2. However, at all other O_2 concentrations the PL decay times of the films with high M_w PS were repeatedly shorter than those with low M_w PS, as shown in Table I and seen in Fig. 6-2(a) for 100% O_2. The shorter decay times observed for the high M_w PS films are evidently due to the improved O_2 permeability.

Comparison of H40 and H40G10 (Fig. 6-2(a) and Table 6.1) indicates that the latter film results in longer τ (by ~18% to ~26% in the presence of oxygen). This behavior is reproducible, but currently not clear. Earlier studies have shown consistently longer τ values when scattering titania particles were introduced into PS

sensing films [28]. Increased τ_0 with increased concentration of ZnO particles in PDMS was also reported. In that case PtOEP aggregated on the silica particles [29]. These scattering centers, however, are of a different nature. A potential scenario explaining the longer τ may be the somewhat reduced permeability of oxygen due to the presence of the PEG and possibly trapping/rattling of the oxygen molecules within the voids of the blended PS:PEG film before encountering the PtOEP dye.

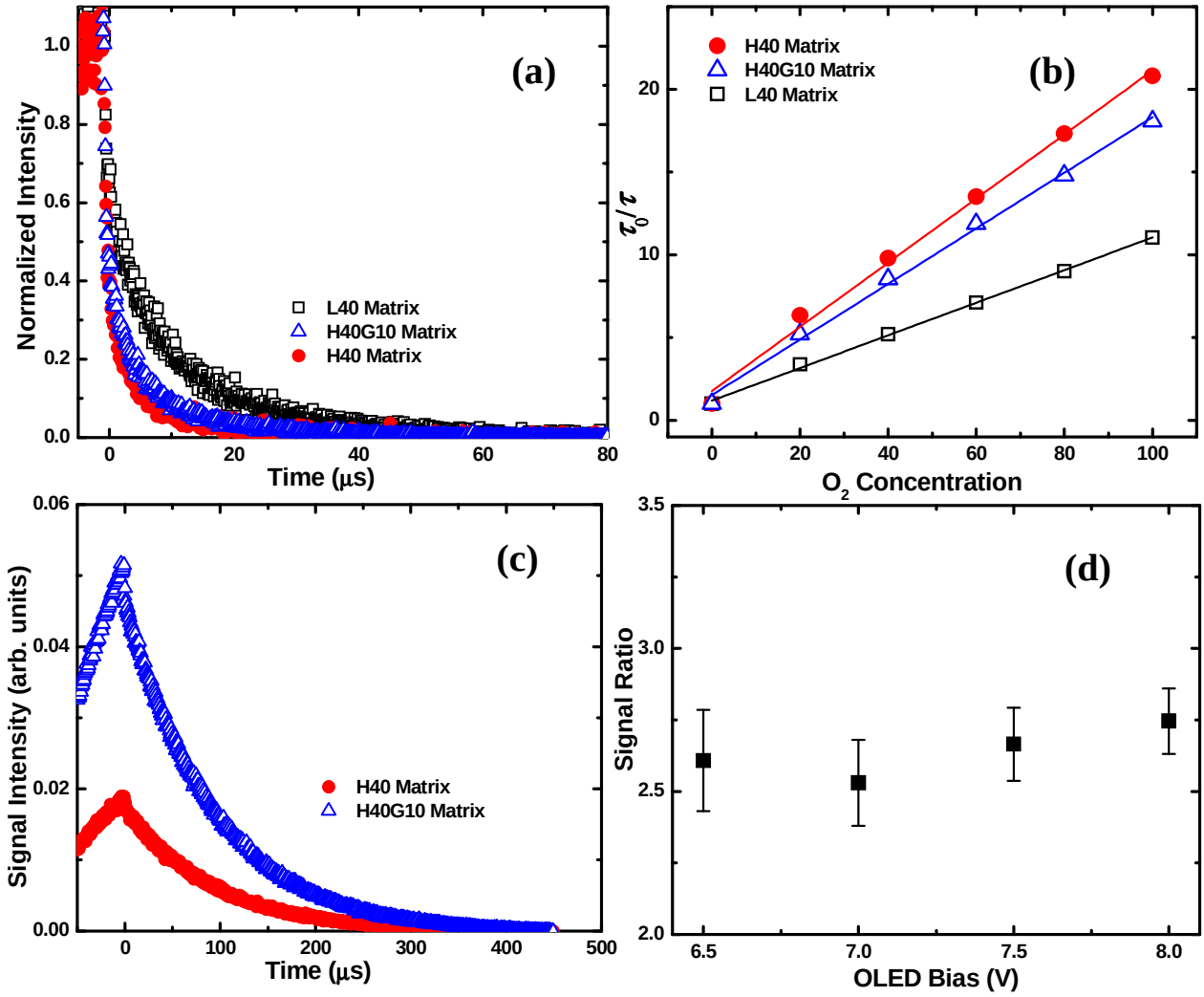

Fig. 6-2 (a) Normalized PL signals of PtOEP in different matrices at 100% O_2 excited by a green μC OLED with a 100 μs pulse width and 8 V amplitude. (b) The SV plots for PtOEP in the different matrices. (c) Comparison of the actual PL signals at 0% O_2 of PtOEP in the H40 and H40G10 matrices both excited by a green μC OLED with 100 μs pulse width and 8 V amplitude; (d) The ratio of the PL signal of H40G10 to that of H40 at different OLED bias voltages.

Table 6.1: The single exponential fitted τ(μs) for the gas-phase O_2 sensor with PtOEP embedded in different matrices excited by a μC green OLED.

	0% O_2	20% O_2	40% O_2	60% O_2	80% O_2	100%O_2	Sensitivity*
L40	96.9	28.7	18.7	13.6	10.8	8.8	11.0
H40	93.0	14.7	9.5	6.9	5.4	4.5	20.7
H40G10	96.4	18.5	11.3	8.1	6.5	5.3	18.2

***** The sensitivity is defined as $S \equiv \tau_0/\tau(100\%\ O_2)$.

As seen in Table 6.1 and Fig. 6-2(b) that shows the SV lines, the sensitivity was highest for the H40 sensing film. It increased from ~11 with the previously used L40 film to ~21 and ~18 for H40 and H40G10, respectively. Although the H40G10 matrix generated a somewhat lower sensitivity compared to H40, the PL signal intensity of the H40G10 film was much larger (~×2.7) as seen in Fig. 6-2(c). This behavior is due to the scattering by the micropores induced by the PEG.

The dependence of this enhancement on the OLED's excitation bias is plotted in Fig 6-2(d). It clearly shows that the embedded scattering microstructures increase the PL signal intensity ~2.7 fold, independent of the on-pulse EL amplitude.

The PL signals of the preceding sections were obtained with a photomultiplier tube (PMT) and a 600 nm long-pass filter to block the EL. Following the successful demonstration of the improvement by using the PtOEP:PS:PEG sensing elements, the optical filter was removed and a small-molecule CuPc/C_{70} (CuPc is the copper phthalocyanine donor and C_{70} is the fullerene acceptor)-based OPD with the structure ITO/1 nm air-plasma-treated LiF/15 nm CuPc/30 nm C_{70}/3.5 nm 4,7-diphenyl-1,10-phenanthroline (BPhen)/120 nm Al [30] was used to achieve a compact all organic-based O_2 sensor.

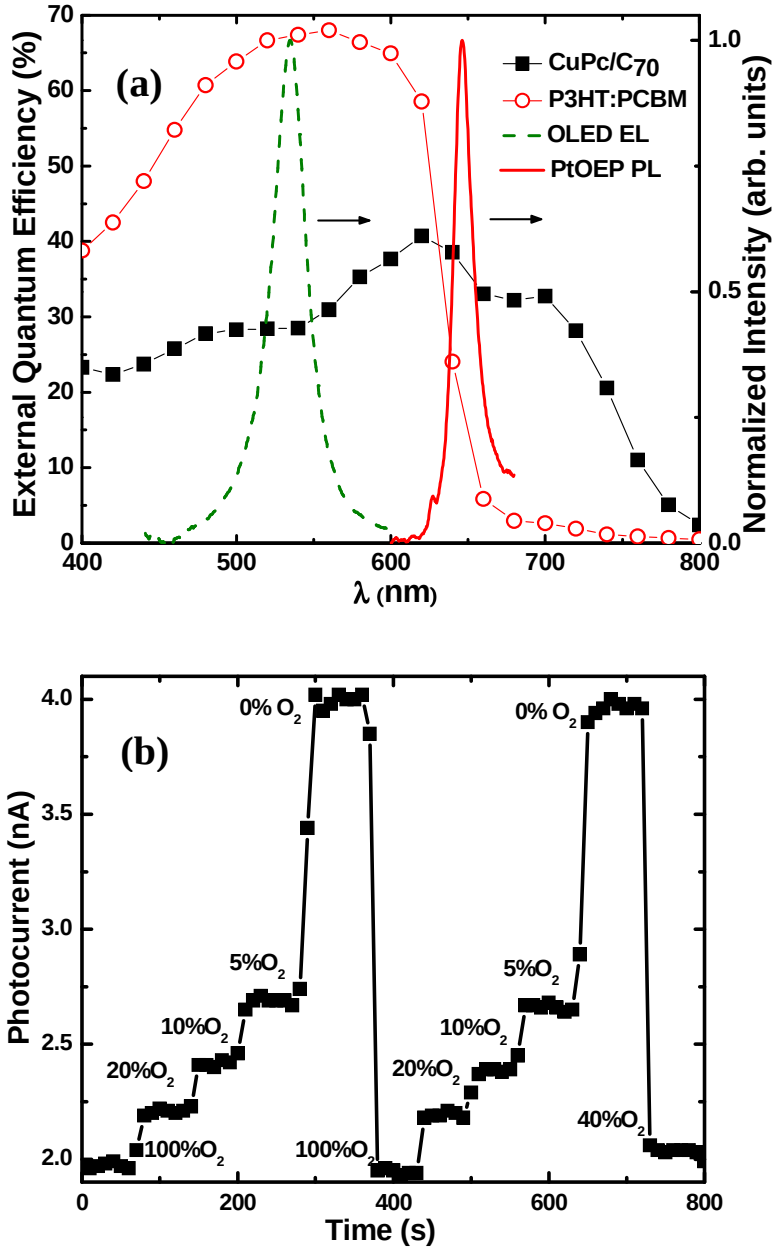

Fig. 6-3 (a) External quantum efficiencies of CuPc/C_{70} (black squares) and P3HT:PCBM (red circles)-based OPDs. The device structures are ITO/1 nm air-plasma-treated LiF/15 nm CuPc/30 nm C_{70} /3.5 nm BPhen /120 nm Al and ITO/poly(3,4-ethylenedioxythiophene): poly(styrenesulfonate) (PEDOT:PSS)/ P3HT:PCBM/Ca/Al. The EL of the μC OLED (dashed green line) and PL of the PtOEP: H40G10 sensing film (solid red line). (b) The sensing signal excited by the μC OLED detected by CuPc/C_{70} OPD at various O_2 concentrations.

Although polymer photovoltaic devices are usually more efficient than the small-molecular ones, the choice of the OPD relies on more than just device efficiency. Fig. 6-3(a) compares the optimized external quantum efficiency (EQE) of two conventional OPDs, i.e., those based on P3HT:PCBM (i.e.,

poly(3-hexylthiophene):[6,6]-phenyl-C_{60}-butyric acid methyl ester) [16,31] or CuPc/C_{70}. The former has a higher power conversion efficiency (PCE) and was used in sensing applications previously [11]. However, in order to further enhance the signal to noise ratio, it is preferable to use an OPD that collects more photons at the longer PL wavelength and is much less responsive to the green region of the EL.

The EQE spectra of the OPDs, the μC green EL, and the PtOEP PL bands are shown in Fig. 6-3(a). As seen, the CuPc/C_{70} OPDs are better suited for PtOEP-based O_2 sensing. The optimized device with a thin air-plasma-treated LiF layer for better hole extraction exhibits a PCE of ~2%, as reported earlier [30]. The photocurrents measured with this OPD for changing [O_2] are shown in Fig. 6-3(b). As clearly seen, the organic-based O_2 sensor successfully performs with a fast response of a few seconds.

6.2.2. Dual sensing platform for dissolved O_2 and pH

In an earlier study we demonstrated multicolor sky-blue to red μC OLED arrays fabricated in a simple method [22]. We applied a similar method to the dual sensing platform for dissolved O_2 (DO) and pH monitoring. This compact dual platform is promising since these two parameters are of great importance in cultivation and bioprocess monitoring [24,25]. Fig. 6-4(a) is the schematic of the set-up. The PtOEP:H40G10 film was directly dropcast on the back of the OLED substrate and the fluorescein was dissolved initially in a pH 10 buffer solution. By adding diluted hydrochloric acid (HCl) and controlling the O_2/Ar gas mixture that flows into the solution, it was possible to control the DO and pH levels. Pixels of 3×3 mm^2 blue and

green μC OLEDs (device structure: 40 nm Ag/3 nm MoO_3/42 nm NPB/56 nm Alq_3/1 nm LiF/100 nm Al for the blue μC OLED and 40 nm Ag/7 nm MoO_3/49 nm NPB/61 nm Alq_3/1 nm LiF/100 nm Al for the green μC OLED) with normal direction peak emissions at ~490 nm (FWHM = 23 nm) and ~540 nm (FWHM = 27 nm), respectively, as shown in Fig.6-4(b), were fabricated on a common substrate. Those emissions bands are suitable for fluorescein absorption, and as mentioned earlier, for PtOEP absorption, respectively. The separation between the pixels was 3 mm; the PD was positioned between the two pixels. Thus, when the blue OLED is turned on, the PD detects mostly the fluorescence from the pH-sensitive fluorescein. Indeed, as shown in Fig. 6-4(c), when the blue μC OLED was turned on the PL signal intensity was almost constant for 0%, 20% and 100% O_2 for a given pH. The intensity dropped sharply for pH values < 7, as expected due to the non-fluorescing cation present in the acidic solution. As seen in Fig. 6-4(d), when the green μC OLED was turned on the signal intensity at all pH values followed largely the same changing trends that depended on the varying [O_2]. Ideally, these PL signals should not change with changing pH when the green μC OLED is on. However, they still exhibited relatively small variations as the pH changed. This was attributed to the fact that the emission spectrum of the green μC OLED shifts to shorter wavelengths at larger angles, which may then also excite the fluorescein. Nonetheless, with such a dual sensing platform one can always acquire a 2-D data table for the PL signal intensities excited by the blue and green OLEDs to obtain both the DO and pH values of a testing solution.

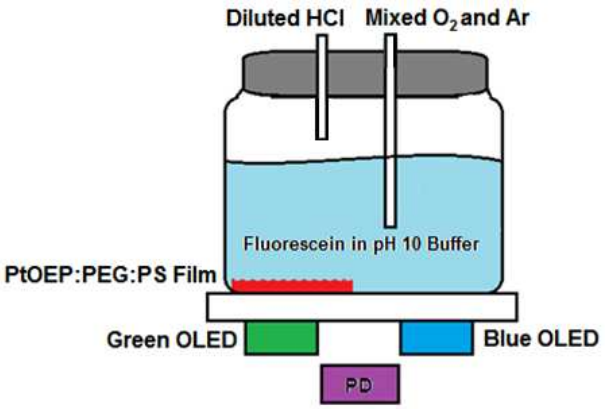
Diluted HCl
Mixed O_2 and Ar
Fluorescein in pH 10 Buffer
PtOEP:PEG:PS Film
Green OLED
Blue OLED
PD

(a)

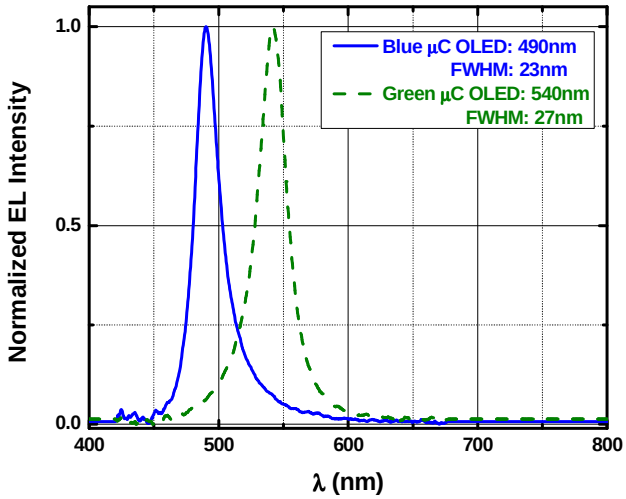
Blue μC OLED: 490nm
FWHM: 23nm
Green μC OLED: 540nm
FWHM: 27nm
Normalized EL Intensity
λ (nm)

(b)

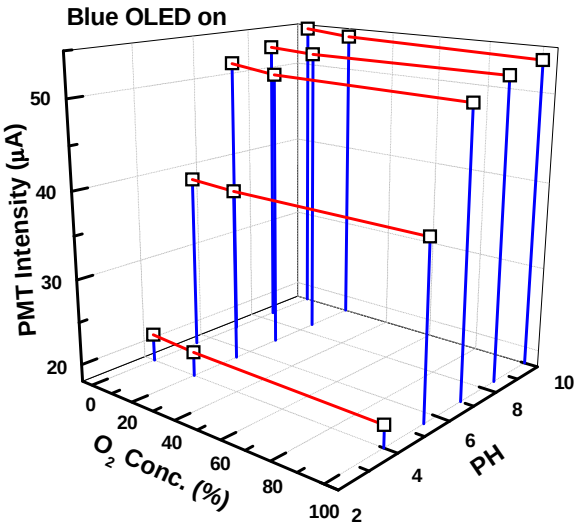
Blue OLED on
PMT Intensity (μA)
O_2 Conc. (%)
PH

(c)

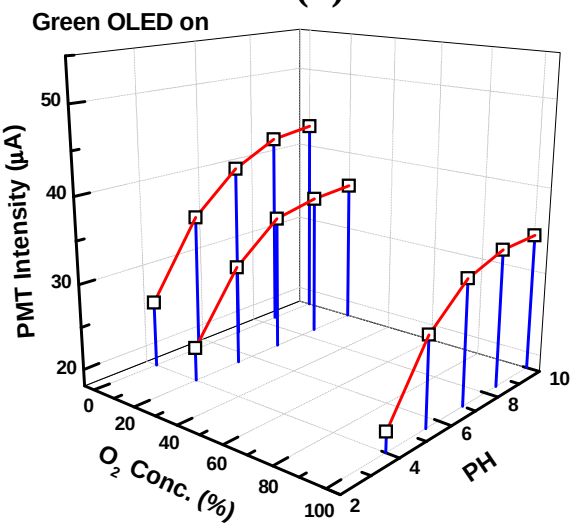
Green OLED on
PMT Intensity (μA)
O_2 Conc. (%)
PH

(d)

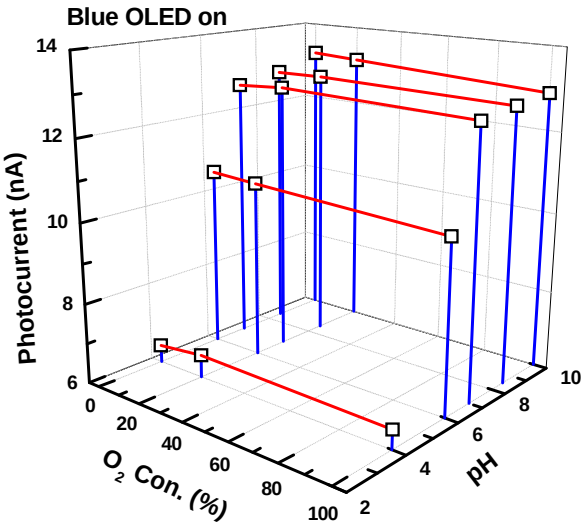
Blue OLED on
Photocurrent (nA)
O_2 Con. (%)
pH

(e)

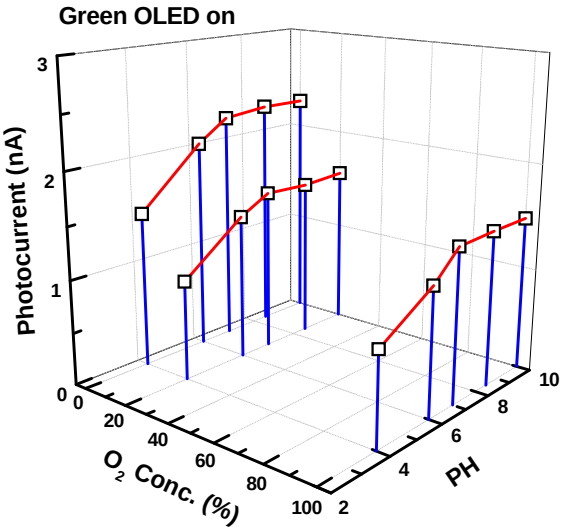
Green OLED on
Photocurrent (nA)
O_2 Conc. (%)
PH

(f)

Fig. 6-4 (a) Schematics of the dual sensing platform for O_2 and pH. The OLED pixels are 3×3 mm^2 and the gap between them is 3 mm. (b) The normal direction EL spectra of the blue and green μC OLEDs. (c) and (d) The signal intensity detected by a PMT at different O_2 and pH levels with the blue and green μC OLEDs. (e) The signal intensity detected by the P3HT:PCBM OPD at different O_2 and pH levels with the blue μC OLED. (f) The signal intensity detected by the CuPc/C_{70} OPD at different O_2 and pH levels with the green μC OLED.

Figs. 6-4(e) and (f) show the all-organic (OLED/PtOEP:PEG:PS/OPD) O_2 + pH sensor. Measurements similar to those shown in Figs. 6-4(c) and (d) were conducted with the P3HT:PCBM OPD for the pH monitoring and with the CuPc/C_{60} OPD for the O_2 sensing. Similar trends were successfully observed, which demonstrates the feasibility of this all-organic dual sensing platform.

As mentioned, the PL signals obtained with the green OLED (meant to excite only the O_2-sensitive PtOEP) varied with pH as well. One way to overcome this issue and actually realize simultaneous monitoring of the DO and pH is to analyze the time-resolved PL + background signals. As demonstrated in Fig. 6-5(a), at the turn-off edge of the green μC OLED bias pulse, the luminescent decay signal is comprised of three parts: the decaying OLED excitation background, the fluorescence decay of fluorescein and the phosphorescence decay of PtOEP, which is much slower than the first two. Hence, a typical decay signal first exhibits a sharp decrease caused by the drop of the OLED EL and the fluorescein's luminescence. The following long decay results from PtOEP's response to different [O_2]. The amplitude difference between the on-pulse signal intensity and the start of the PtOEP phosphorescent decay relates to the pH value + a constant OLED background. Hence, the change in this difference is indicative of the pH. That is, the DO and pH can be simultaneously analyzed with the τ and I modes, respectively.

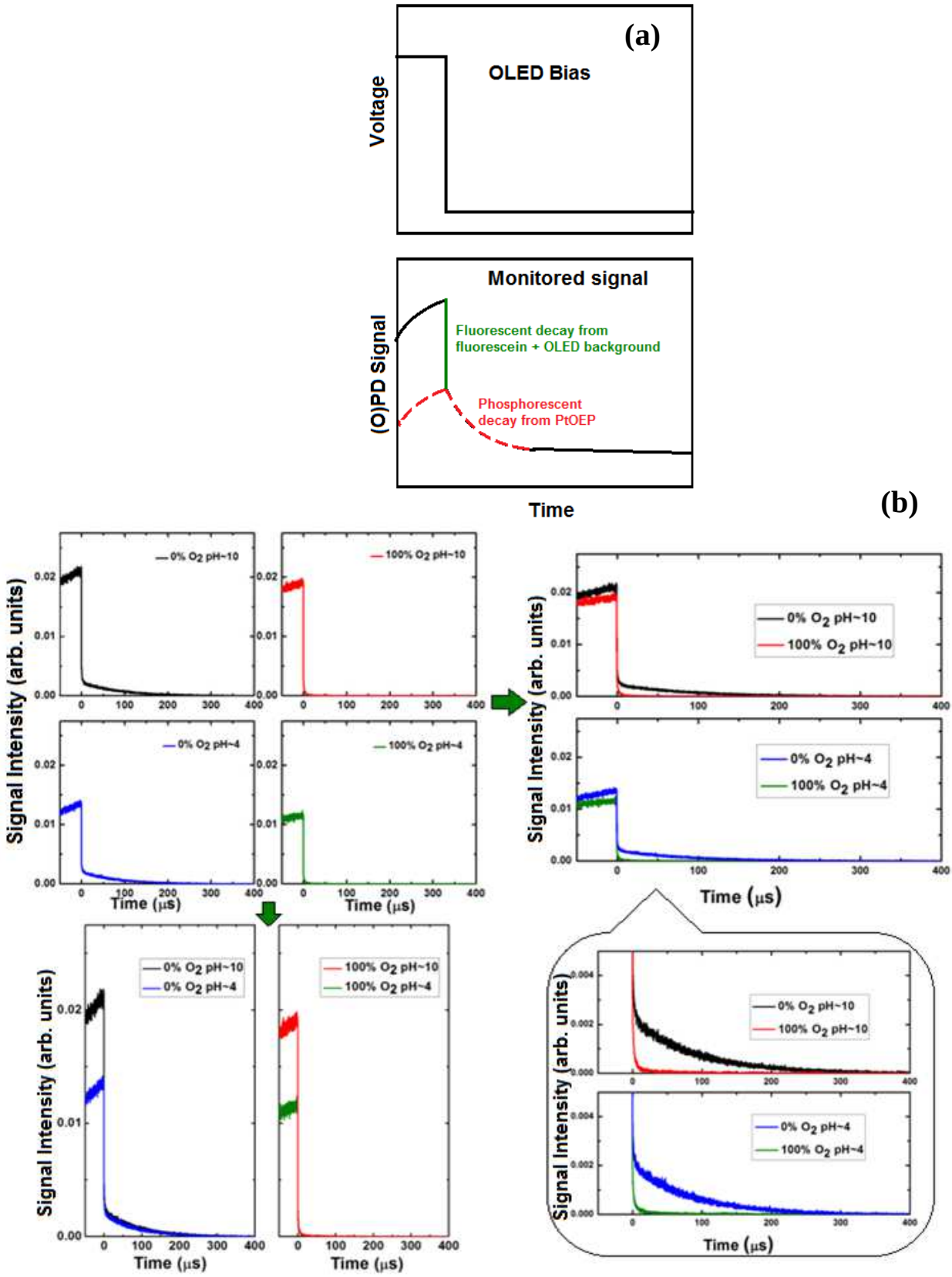

Fig. 6-5 (a) The components of the monitored signal following the OLED pulse: the phosphorescence decay of PtOEP, the fluorescence decay of fluorescein and the OLED background. (b) Luminescent signals obtained by using the green μC OLED at (i) 0% O_2, pH ~ 10, (ii) 100% O_2, pH ~ 10, (iii) 0% O_2, pH ~ 4, (iv) 100% O_2, pH ~ 4.

In order to prove the validity of such an analysis, we compared the time-resolved

decay signals at four extreme conditions: (*i*) 0% O_2, pH~10, (*ii*) 100% O_2, pH~10, (*iii*) 0% O_2, pH~4 and (*iv*) 100% O_2, pH~4. The transient signals of these four conditions are shown at the top left part of Fig. 6-5(b). By following the downward arrow to compare signals with the same [O_2], it is found that for exposure to both 0% and 100% gas-phase O_2, the on-pulse amplitudes are higher for pH ~ 10 and lower for pH ~ 4 with the same PL decay times at the μs range. By following the arrow to the right to compare signals at the same pH, as seen, the difference of the transient decays between 0% and 100% O_2 are obvious. With the contributions of the PtOEP PL subtracted, the fast-decaying amplitudes are unchanged at a constant pH.

6.3 Conclusions

In summary, we have successfully constructed an all-organic electronic-based novel sensing platform architecture for simultaneously monitoring O_2 and pH. This was achieved by applying various methods to improve the sensor performance and analyze the obtained data. For oxygen detection, PtOEP embedded in high M_w PS:PEG matrix was directly cast on the back of the OLED substrate for higher O_2 permeability and stronger OLED EL. The detection sensitivity consequently improved from ~11 to ~21. PEG was blended with PS to form scattering microstructures that enhance the detectable signal intensity ~2.7 fold. For better signal to noise ratio, green μC OLEDs, with spectrally narrowed and concentrated EL, together with a CuPc/C_{70}-based OPD, whose spectral response is better suited to the PtOEP PL, were utilized. For the dual sensing of DO and pH, two μC OLED excitation sources were fabricated combinatorially with the normal direction peak emission wavelengths

designed for the O_2-sensitive PtOEP and the pH-sensitive fluorescein. In this way, one could extract a 2-D data table for monitoring these two important analytes. Furthermore, from the transient decay signals following the OLED pulses, one could resolve the signals related to DO and pH by employing both the τ and I detection modes. Hence, the two analytes could be monitored simultaneously. The combination of the PtOEP:PS:PEG sensing film coupled with the multicolor microcavity OLEDs and the appropriate OPD and the possibility to combine time- and intensity-domain analyses pave the way for realizing a more simple and cost-effective all organic electronic O_2 and pH sensors, which can be expanded to detect other (bio)chemical analytes.

6.4 Experimental Section

Sensing elements preparation: PtOEP was obtained from H. W. Sands, and PS, with M_w ~45,000 and ~280,000, from Sigma-Aldrich. The O_2 sensing films were prepared by dropcasting 200 μL of toluene solution on the back of the 1×1 $inch^2$ OLED substrates with 1mg/mL PtOEP embedded in three different matrices: 40 mg/mL low M_w PS (M_w ~ 45,000), 40 mg/mL high M_w PS (M_w ~ 280,000) and 40:10 mg/mL high M_w PS (M_w ~ 280,000): PEG (M_w ~ 1,000), denoted as samples L40, H40, and H40G10, respectively. The resulting films on the encapsulated OLED devices were allowed to dry in the dark at ambient temperature for at least 12 hours. The concentration of the fluorescein was 6 μM in pH 10 buffer.

OLED and OPD fabrication: μC OLEDs were thermally evaporated on the glass substrates in a vacuum chamber (background pressure ~ 10^{-6} Torr) located in an

Ar-filled glovebox with structures as 40 nm Ag/3 nm MoO_3/42 nm NPB/56 nm Alq_3/1 nm LiF/100 nm Al for the blue μC OLED and 40 nm Ag/7 nm MoO_3/49 nm NPB/61 nm Alq3/1 nm LiF/100 nm Al for the green μC OLED. The evaporation rate of organic layers was ~ 1Å/s. 3×3 mm^2 individually addressable OLED pixels were fabricated with 3 mm gap between them. The encapsulating cover glasses were glued using Torr Seal epoxy to prevent water and O_2 exposure of the pixels. The P3HT:PCBM and CuPc/C_{70} OPDs were fabricated as described by Xiao et al [30, 31].

Instrumentation: For the time-resolved signal analysis, the OLEDs were driven with a 100 μs electrical pulse generated by an Avtech AV-1011B pulse-generator. The PL was monitored with either a Hamamatsu R6060 PMT or OPDs. Various levels of O_2 were generated by flowing O_2/Ar mixtures controlled by Tylan FC-280 mass flow controllers while maintaining a constant total flow rate. The pH was controlled by stepwise adding 30 μL of diluted HCl (Fisher Scientific) into a 2 mL testing reservoir.

Acknowledgements

Ames Laboratory is operated by Iowa State University for the US Department of Energy (USDOE) under Contract No. DE-AC 02-07CH11358. This research was supported by Basic Energy Sciences, Materials Sciences and Engineering Division, USDOE.

References

1. S. R. Forrest, Nature **428**, 911 (2004).
2. A. J. Heeger, Chem. Soc. Rev. **39**, 2354 (2010).
3. Organic Electronics in Sensors and Biotechnology (Eds: R. Shinar, J. Shinar,

McGraw Hill, NY, 2009).

4. J. Shinar, R. Shinar, J. Phys. D: Appl. Phys. **41**, 133001 (2008).
5. M. Koeste, P. Rensing, G. van Heck, R. Sharpe, B. Allard, F. Wieringa, P. Kruijt, N. Meulendijks, H. Jansen, H. Schoo, in Organic Field-Effect Transistors VII and Organic Semiconductors in Sensors and Bioelectronics, (Eds: Z. Bao, I. McCulloch, R. Shinar and G. Malliaras), Proc. SPIE **7054**, 70541I, (2008).
6. A. Pais, A. Banerjee, D. Klotzkin, I. Papautsky, Lab Chip **8**, 794 (2008).
7. M. Ramuz, D. Leuenberger, R. Pfeiffer, L. Bürgi, C. Winnewisser, Eur. Phys. J. Appl. Phys. **46**, 12510 (2009).
8. E. L. Ratcliff, P. A. Veneman, A. Simmonds, B. Zacher, D. Huebner, S. S. Saavedra, N. R. Armstrong, Anal. Chem. **82**, 2734 (2010).
9. E. Kraker, A. Haase, B. Lamprecht, G. Jakopic, C. Konrad, S. Köstler, Appl. Phys. Lett. **92**, 033302 (2008).
10. T. Mayr, T. Abel, B. Enko, S. Borisov, C. Konrad, S. Köstler, B. Lamprecht, S. Sax, E. J. W. List, Ingo Klimant, Analyst **134**, 1544 (2009).
11. K. S. Nalwa, Y. Cai, A. L. Thoeming, J. Shinar, R. Shinar, S. Chaudhary, Adv. Mater. **22**, 4157 (2010).
12. F. Lefèvre, A. Chalifour, L. Yu, V. Chodavarapu, P. Juneau, R. Izquierdo, Lab Chip **12**, 787 (2012).
13. Z. B. Wang, M. G. Helander, J. Qiu, D. P. Puzzo, M. T. Greiner, Z. M. Hudson, S. Wang, Z. W. Liu, Z. H. Lu, Nature Photonics **5**, 753 (2011).
14. L. Xiao, Z. Chen, B. Qu, J. Luo, S. Kong, Q. Gong, J. Kido, Adv. Mat. **23**, 926

(2011).

15. M. Furno, R. Meerheim, S. Hofmann, B. Lüssem, Karl Leo, Phys. Rev. B **85**, 115205 (2012).
16. C. J. Brabec, S. Gowrisanker, J. J. M. Halls, D. Laird, S. Jia, S. P. Williams, Adv. Mat. **22**, 3839 (2010).
17. L. Dou, J. You, J. Yang, C.-C. Chen, Y. He, S. Murase, T. Moriarty, K. Emery, G. Li, Y. Yang, Nature Photonics **6**, 180 (2012).
18. Y. Sun, G. C. Welch, W. L. Leong, C. J. Takacs, G. C. Bazan, A. J. Heeger, Nature Materials **11**, 44(2012).
19. R. Liu, Y. Cai, J.-M. Park, K.-M. Ho, J. Shinar, R. Shinar, Adv. Funct. Mater. **21**, 4744 (2011).
20. Y. Amao, Microchim. Acta **143**, 1 (2003).
21. R. Liu, Z. Ye, J.-M. Park, M. Cai, Y. Chen, K.-M. Ho, R. Shinar, J. Shinar, Optics Express **19**, A1272 (2011).
22. R. Liu, C. Xu, R. Biswas, J. Shinar, R. Shinar, Appl. Phys. Lett. **99**, 093305 (2011).
23. A. Cook, A. Le, J. Phys. Chem. Lab **10**, 44 (2006).
24. Y. Kostov, P. Harms, L. Randers-Eichhorn, G. Rao, Biotechnology and Bioengineering **72**, 346 (2001).
25. S. Arain, G. T. John, C. Krause, J. Gerlach, O. S. Wolfbeis, I. Klimant, Sensors and Actuators B **113**, 639 (2006).
26. S. Schreml, R. J. Meier, O. S. Wolfbeis, M. Landthaler, R.-M. Szeimies, P. Babilas,

PNAS **108**, 2432 (2011).

27. Y. Sun, S. R. Forrest, Nature Photonics **2**, 483 (2008).

28. Z. Zhou, R. Shinar, A. J. Allison, J.Shinar, Adv. Funct. Mater. **17**, 3530 (2007).

29. X. Lu, I. Manners, M. A.Winnik, Macromolecules **34**, 1917 (2001).

30. T. Xiao, W. Cui, M. Cai, R. Liu, J. W. Anderegg, J. Shinar, R. Shinar, Journal of Photonics for Energy **2**, 021006 (2012).

31. T. Xiao, W. Cui, J. Anderegg, J. Shinar, R. Shinar, Organic Electronics **12**, 257 (2011).

Chapter 7. Summary

As mentioned in the Introduction, guest-host OLEDs are largely applied for higher efficiency and brightness as they alleviate the concentration quenching issue. Such OLEDs are good candidates for OLED-based (bio)chemical sensing platforms. However, in Chapter 2, we showed that ITO/CuPc/NPB/C6-doped Alq_3/Alq_3/LiF/Al devices and other charge trapping guest-host SMOLEDs exhibit EL spikes at 70 – 300 ns and μs long EL tails following a bias pulse. The spikes are not affected by early-stage device degradation, but are strongly influenced by temperature, pulse amplitude, duration, the distance of the doped layer from the HTL and the reverse bias applied after the pulse. They are also significantly weaker in devices where charge transport is largely enhanced. Such EL spikes and tails raise an issue for OLED-based sensing as they may distort the PL sensing signals.

Good agreement is found between the experimental data and a model based on recombination of CCPs and charges that are initially unpaired. The generation of spikes exceeding the on-pulse EL level is attributed to the combination of CCP formation and reduced electric field-induced SE dissociation after the pulse. The comparison of the transient EL behavior of various SMOLEDs suggests that the EL spikes are an additional reliable tool to identify the main emitting mechanism in guest-host OLEDs.

In Chapter 3, we have demonstrated a simple monolithic fabrication method for achieving multicolor μC OLEDs by tuning the thickness of the HIL/spacer MoO_x. The peak emission wavelength was tunable from 493 to 639 nm with the electrical

characteristics of the OLEDs unchanged. Such a method was applied to fabricate the OLED light source for dual sensing in Chapter 6. The higher $L_{\perp max}$ obtained with the MoO_x-based μC OLEDs provides further evidence that the breakdown of the conventional CuPc-based OLEDs likely occurs due to Joule heating produced by the accumulated charges at the unfavorable HIL/HTL interface.

We also successfully fabricated controlled microporous structures to enhance the forward light extraction of OLED by up to ~60% by dropcasting toluene solutions of various PS:PEG ratios on the back side of the substrate. As shown in Chapter 4, this enhancement originates from scattering by both surface and bulk micropores of the film and provides an extremely simple and economical means for outcoupling enhancement in OLEDs and potential applications in OLED-based luminaires and sensors.

In Chapter 5 and 6, we utilized the findings and development described in Chapter 2-4 to improve the OLED-based PL sensor performance. We found that at high O_2 levels, the decay curves contain contributions from the post-pulse transient EL due to the EL spikes and tails generated in guest-host OLEDs mentioned in Chapter 2. This issue is alleviated when using CBP- or μC Alq_3-based OLEDs as the excitation source, where (in addition to the absence of a post-pulse spike) the absorption of the sensing film is significantly more efficient and the interference from the long-wavelength tail of typical EL bands is minimized, respectively. Additionally, uniform 2 μm-pitch μLAs made from polyurethane, attached to the backside of a CBP OLED, significantly enhance the detected signal intensity by directing the otherwise isotropic

and partially blocked PL toward the PD.

A similar approach is applied in Chapter 6, where PtOEP embedded in high M_w PS:PEG matrix was directly cast on the back of the OLED substrate for higher O_2 permeability and stronger OLED EL. The detection sensitivity consequently improved from ~11 to ~21. PEG was blended with PS to form scattering microstructures that enhance the detectable signal intensity ~2.7 fold. A green μC OLED together with a CuPc/C_{70}-based OPD, whose spectral response is better suited to the PtOEP PL, were utilized to achieve an all-organic based O_2 sensor.

With the method demonstrated in Chapter 3, two μC OLED excitation sources were fabricated combinatorially with the normal direction peak emission wavelengths designed for the O_2-sensitive PtOEP and the pH-sensitive fluorescein. In this way, one could extract a 2-D data table for monitoring these two important analytes. Furthermore, from the transient decay signals following the OLED pulses, one could resolve the signals related to DO and pH by employing both the τ and I detection modes. Hence, the two analytes could be monitored simultaneously.

The combination of the PtOEP:PS:PEG sensing film coupled with the multicolor microcavity OLEDs and the appropriate OPD, and the possibility to combine time- and intensity-domain analyses have shed light on the opportunities to realize simple, compact, potentially disposable sensors for the detection of O_2, pH and other (bio)chemical analytes.

Acknowledgements

I would like to take this opportunity to express my deepest appreciation to my advisors Dr. Joseph Shinar and Dr. Ruth Shinar for their guidance, help and encouragement through my graduate research and studies. I feel very fortunate to choose them as my advisors.

I would also like to thank my parents and my wife, Xiao Lin for their selfless support. Without their understanding, none of the work could be done easily. The care and love that they showed was always the relief and motivation for me when I met difficulties.

It has been a precious 5-year period working in the group. I would like to convey my thanks to my colleagues Yun Tian, Zhengqing Gan, Yuankun Cai, Emily Hellerich, Ying Chen, Min Cai, Teng Xiao, Weipan Cui, Eeshita Manna, Fadzai Fungura, and Joong-Mok Park for the in-depth discussions and collaborations. Special thanks to Dr. Rana Biswas for his extensive simulation work and research advice.

Many thanks to the funding agencies, including the US Department of Energy and the NSF for supporting the research work of this dissertation. I would also like to thank Larry, Lori, and Gloria for their excellent administrative work.